

This Memoirs is annually issued. Selected original works of the members of the Faculty of Engineering are compiled herein. Abstracts of paper presented elsewhere during the current year are also compiled in the latter part of the volume.

All communications with respect to Memoirs should be addressed to:

Dean of the Graduate School of Engineering
Osaka City University
3-3-138, Sugimoto, Sumiyoshi-ku
Osaka 558-8585, Japan

Editors

Makoto HOSODA

Ayumu SUGITA

Daisuke MIYAZAKI

Hiroshi KAWAKAMI

Hisao TSUNOKAKE

Taro TACHIBANA

Tetsuro TANIGUCHI

MEMOIRS OF THE FACULTY OF ENGINEERING
OSAKA CITY UNIVERSITY

VOL. 53

DECEMBER 2012

CONTENTS

Regular Articles 1

Urban Engineering

Architecture and Building Engineering

Ultimate Seismic Resistance Capacity for Long Span Lattice Structures under Vertical Ground Motions

Yoshiya TANIGUCHI 1

Civil Engineering

Citizen Awareness of Community Buses from the Public Support Perspective

Yusuke KURASHIMA and Takashi UCHIDA 15

Applied Chemistry and Bioengineering

Applied Chemistry

Liquid / Liquid Near Interface Analysis by Micro-XRF Using Needle-Type Collimators

Yoshihiko NISHIDA and Kouichi TSUJI 27

Abstracts of Papers Published in Other Journals 31

Mechanical and Physical Engineering

Mechanical Engineering 33

Intelligent Materials Engineering 42

Applied Mathematics 50

| | |
|--|----|
| <i>Physical Electronics and Informatics</i> | |
| <i>Electrical Engineering</i> | 51 |
| <i>Applied Physics</i> | 53 |
| <i>Information and Communication Engineering</i> | 64 |
| | |
| <i>Applied Chemistry and Bioengineering</i> | |
| <i>Applied Chemistry</i> | 65 |
| <i>Bioengineering</i> | 74 |
| | |
| <i>Urban Engineering</i> | |
| <i>Architecture and Building Engineering</i> | 79 |
| <i>Civil Engineering</i> | 81 |
| <i>Environmental Urban Engineering</i> | 94 |

MEMOIRS
OF THE
FACULTY OF ENGINEERING
OSAKA CITY UNIVERSITY

VOL. 53

DECEMBER 2012

PUBLISHED BY THE
GRADUATE SCHOOL OF ENGINEERING
OSAKA CITY UNIVERSITY

Ultimate Seismic Resistance Capacity for Long Span Lattice Structures under Vertical Ground Motions

Yoshiya TANIGUCHI*

(Received October 5, 2012)

Synopsis

Seismic resistance capacities of frame structures have been discussed with equilibrium of energies among many researchers. The early one is the limit design presented by Housner [Ref.1], that is, frame structures should possess the plastic deformation ability equivalent to an earthquake input energy given by a velocity response spectrum. The earthquake input energy consists of some amount dissipated through the damping and the remainder stored in the structure. The remainder consists of the kinetic energy, the elastic strain energy and plastic energy. The plastic energy might be a portion of the earthquake input energy. On such studies of response estimation by the energy equilibrium, the potential energy has been generally abandoned, since the effect of self weight or fixed loads on the potential energy is negligible while ordinary buildings usually sway in the horizontal direction. However, it could be said that the effect of gravity has to be considered for long span structures since the mass might be concerned with the vertical response. Then in this paper, as for ultimate seismic resistance capacity of long span structures, an estimation method considering the potential energy is discussed as for plane lattice beams and double-layer cylindrical lattice roofs. The method presented can be done with the information of static nonlinear behavior, natural periods and velocity response spectrum of seismic motions, that is, any complicated nonlinear time-history analysis is not required. The value estimated can be modified with the properties of strain energy absorption and the safety static factor.

KEYWORDS: Ultimate seismic resistance capacity, Limit state load, Limit state deformation, Static absorbed energy, Static safety factor, Seismic motion

1. Introduction

Long span and spatial structures have been utilized as a roof structure of buildings including large space. They are often used as a place of refuge or stronghold of rescue in a disaster area. Then it is important for government or caretaker to grasp ultimate seismic resistance capacity of such buildings without regard to new or existing buildings in advance. They might wish to know concretely the seismic motion level at which structures reach a limit state if it would be subjected to over design loads. The information would be just an ultimate seismic resistance capacity of structures.

The estimation methods of seismic response have been studied with equilibrium of energies instead of a time history analysis by many researchers. Among them, the limit design presented by Housner [Ref.1] is found as an early one. The method was to design the structure so that it could plastically absorb energy equal to the earthquake input energy estimated by a velocity response spectrum. Kato and Akiyama [Ref.2] defined the energy absorption due to plastic deformations as energy contributed to structural damages. They carried out numerical studies with a 5 mass model for many cases, to confirm validity of the limit design. As for the estimation method with such energy index with respect to spatial structures, Tada et al. [Ref.3] introduced gravity energy, defined by the product of the self weight and vertical displacements, into the input energy as a collapse index for double-layer grids. It was shown that the double-layer grid began to collapse when the earthquake energy input to the grid exceeded a certain amount. Qiao et al. [Ref.4] investigated the dynamic collapse behavior of a single layer shallow lattice dome to make clear the relationships between the maximum absorbed energies and the vibration modes, and pointed out that the maximum absorbed energies would change corresponding to vibration modes. As a further study of estimation method for dynamic collapse level of seismic motions, Taniguchi [Ref.5] treated plane lattice arches and double layer cylindrical lattice roofs and defined a limit state load and a limit state deformation representing an ultimate state, given by the information of static nonlinear behavior under vertically loading. An estimation method of ultimate seismic resistance capacity was presented with the static absorbed energy until an initial yield state and ultimate state, which is a kind of an extrapolation method. The method

*Professor, Dept. of Urban Engineering, Osaka City University

includes a modification to improve the accuracy, considering the properties of elastic and plastic strain energies of structures during a pushover analysis until an ultimate state. However, the method has a retrogression equation which includes an unknown quantity. Then in this paper, the effect of static safety factors is investigated to make clear the meanings of the unknown quantity in the modification equation, for lattice beams of two types, plane lattice arches and double-layer cylindrical roofs described in Ref.5, to establish a consistent estimation method of the ultimate seismic resistance capacity.

2. Numerical model

Numerical models are shown in figures 1 and 2. They are supported at the side ends, by roller and pin-supports. The models consist of two member types; all members are the same section property denoted as small letter a and the 3 center top chord members are larger than the others, denoted as small letter b. All nodes are assumed to be rigid jointed since the joints may have sufficient strength and stiffness. The static safety factor ν , that represents the ratio of initial yield load against the dead load including the self-weight, is treated as a numerical parameter $\nu = 2, 3, 4$. The section properties of models are shown in Table 1.

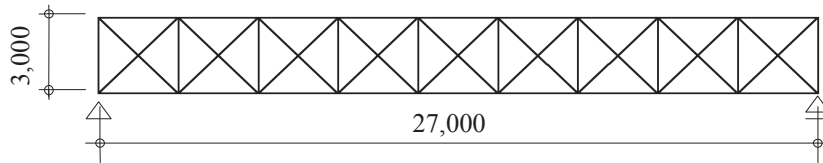


Fig.1 Plane lattice beam of X type (X)

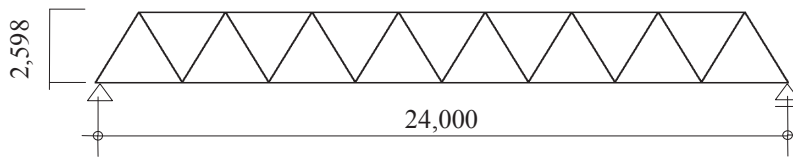


Fig.2 Plane lattice beam of Warren type (W)

Table 1 Section properties of models

| Model | Safety factor ν | Dead load | Section size $\phi \times t$ (mm) | Section area A (cm ²) | Moment inertia I (cm ⁴) |
|--|------------------------|---------------|--------------------------------------|--|--|
| | | P_{DL} (kN) | | | |
| Xa | 2 | 155.22 | 89.1 × 4.5 | 11.96 | 107 |
| | 3 | 103.48 | | | |
| | 4 | 77.61 | | | |
| Xb | 2 | 155.17 | 89.1 × 4.5 | 11.96 | 107 |
| | 3 | 103.45 | 114.3 × 4.5 | 15.52 | 234 |
| | 4 | 77.59 | | | |
| Wa | 2 | 135.91 | 89.1 × 4.5 | 11.96 | 107 |
| | 3 | 90.61 | | | |
| | 4 | 67.95 | | | |
| Wb | 2 | 135.38 | 89.1 × 4.5 | 11.96 | 107 |
| | 3 | 90.25 | 114.3 × 4.5 | 15.52 | 234 |
| | 4 | 67.69 | | | |
| Young's modulus E (N/mm ²) | | | | 205,000 | |
| Yield stress σ_y (N/mm ²) | | | | 300 | |

3. Static elasto-plastic behavior

Push-over analyses were carried out to grasp the nonlinear behavior of models, under vertical distributed loads which was nodal loads corresponding to the covered area. In the static analysis the energy equilibrium is expressed as Equation (1).

$$E^e - E^G = E^F \quad (1)$$

, where E^e is the strain energy, E^G is the potential energy performed by the product of the self-weight and vertical displacements. E^F is the energy done by the external loads. E^e consists of elastic strain energy ${}_sW_e$ and the dissipation energy ${}_sW_p$ done by plastic deformations. Each energy is expressed as an equivalent velocity as follows:

$${}_sV^e = \sqrt{2E^e/M}, \quad {}_sV^G = \sqrt{2E^G/M}, \quad {}_sV^F = \sqrt{2E^F/M} \quad (2)$$

, where M is the total mass of each model. The former subscript s denotes the static analysis. In this paper, ${}_sV^F$ is defined as static absorbed energy and the maximum value of ${}_sV^F$ is considered as the maximum energy input to the structure. The equivalent velocity of strain energy E^e at the maximum ${}_sV^F$ is denoted as ${}_sV_f$. Further the equivalent velocities of strain energy at the elastic limit load P_{LE} and the limit state load P_{GY} are denoted as ${}_sV_{LE}$ and ${}_sV_{GY}$ respectively. The limit state load, as shown in Figure 3, is the load bearing capacity at an ultimate state after peak. The limit state deformation corresponding to the limit state load P_{GY} is represented by the limit state deformation factor α and the elastic limit deformation δ_{LE} . It should be noted that P_{LE} may be defined as another phenomenon, i.e. elastic buckling.

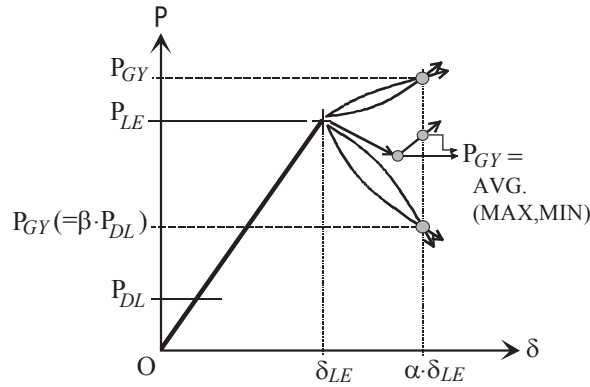


Fig.3 Limit state load and limit state deformation

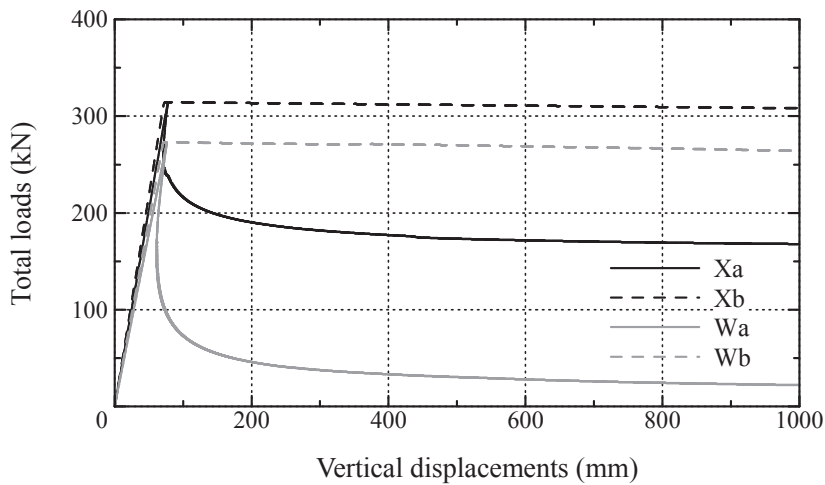


Fig.4 Load-deformation curves of models

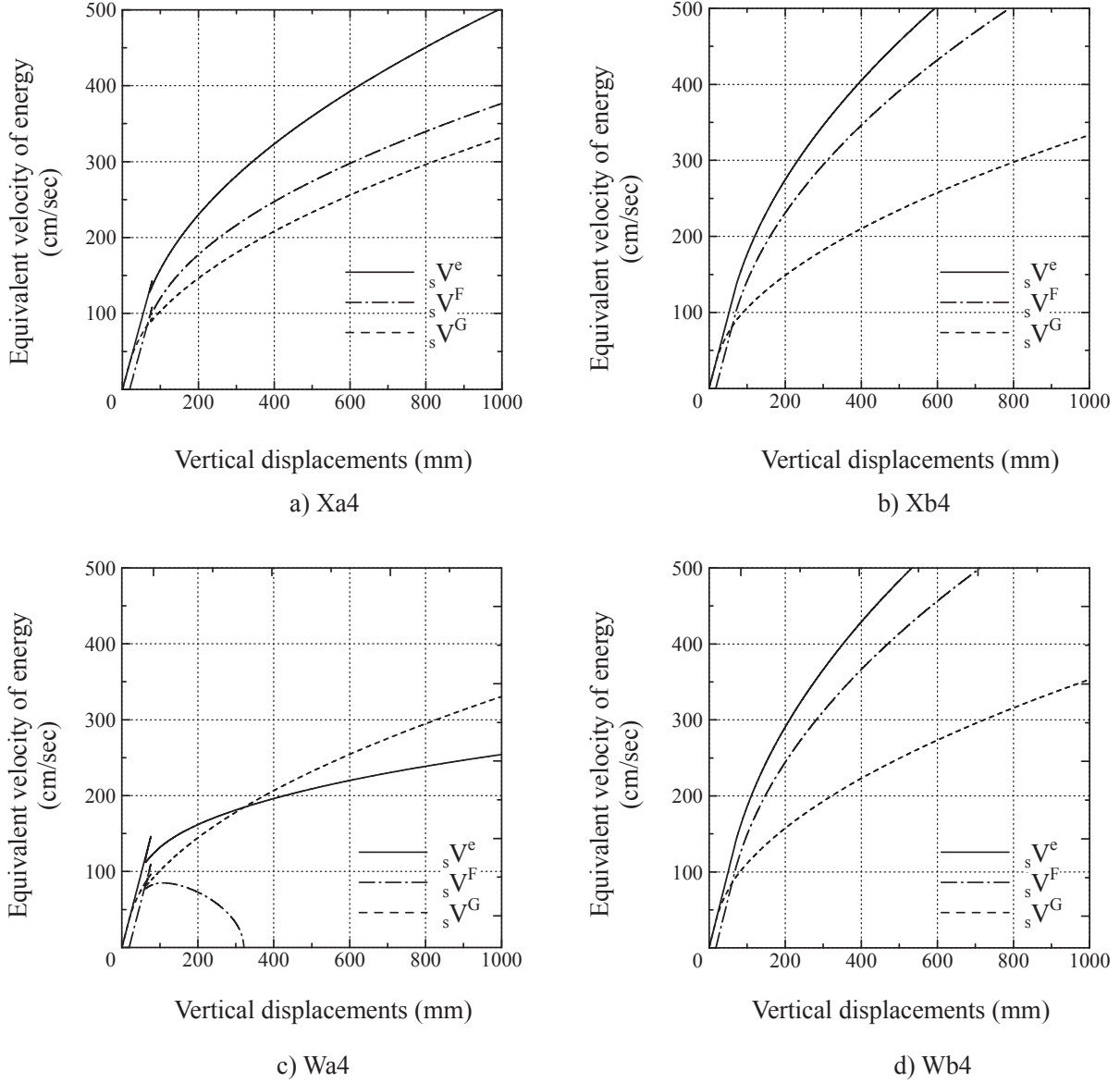


Fig.5 Equivalent velocities of energy and center vertical deformations

The load-deformation curves of plane lattice beams are shown in Figure 4. The horizontal axis represents the vertical displacements of center bottom node. The results of Xb and Wb do not show any reduction since they are yielded in tensile axial loads. The results of Xa and Wa show some reduction because of compressive member failure. Xa model shows relatively gentle reduction than Wa since it has both tensile and compressive member failures. The relationships between three energy and vertical deformations of each model are shown in Figure 5. The model Wa4 shows the peak of ${}_sV^F$ and the other models do not show any peak in the present work.

The equivalent velocities of strain energy are listed in Table 2. The values ${}_sV_f$ of Xa, Xb and Wb are given by the condition of tensile strain 3%, being assumed as the condition of tensile member failure. The values ${}_sV_{GY}$ are estimated at the two factors $\alpha=3$ & 6. The values ${}_sW_e/{}_sW_p$ represent the ratio of the elastic strain energy ${}_sW_e$ and the plastic strain energy ${}_sW_p$ at ${}_sV_{GY}$.

4. Natural vibration property

The results of free vibration analyses are shown in Table 3. The top 3 of effective mass ratio are shown in each table. The natural periods are almost equal to each other since the stiffness of models are almost equal as shown in Figure 4.

Table 2 Equivalent velocities of strain energy and ${}_sW_e/{}_sW_p$

| Model | Safety factor ν | ${}_sV_{LE}$ (cm/sec) | ${}_sV_F$ (cm/sec) | ${}_sV_{GY}$ (cm/sec) | | ${}_sW_e/{}_sW_p$ | |
|-------|------------------------|--------------------------|-----------------------|-----------------------|--------------|-------------------|--------------|
| | | | | $\alpha=3.0$ | $\alpha=6.0$ | $\alpha=3.0$ | $\alpha=6.0$ |
| Xa | 2 | 99.15 | 236.98 | 174.27 | 244.24 | 0.21 | 0.15 |
| | 3 | 121.43 | 290.25 | 213.44 | 299.14 | | |
| | 4 | 140.26 | 335.21 | 246.51 | 345.52 | | |
| Xb | 2 | 95.99 | 291.38 | 201.89 | 297.00 | 0.30 | 0.12 |
| | 3 | 117.37 | 356.72 | 247.06 | 363.33 | | |
| | 4 | 135.46 | 411.81 | 285.05 | 419.34 | | |
| Wa | 2 | 103.30 | 103.30 | 118.69 | 143.94 | 0.06 | 0.04 |
| | 3 | 126.41 | 126.41 | 145.33 | 176.23 | | |
| | 4 | 146.04 | 146.04 | 167.79 | 203.49 | | |
| Wb | 2 | 100.01 | 310.82 | 212.54 | 312.88 | 0.29 | 0.12 |
| | 3 | 122.27 | 380.71 | 260.12 | 382.95 | | |
| | 4 | 141.10 | 439.55 | 300.28 | 442.03 | | |

Table 3 Natural vibration property

a) Xa

| Mode No | Natural period(sec) | | | Effective mass ratio (%) | | Order | |
|------------|---------------------|---------|---------|--------------------------|-------------|-------|---|
| | $\nu=2$ | $\nu=3$ | $\nu=4$ | X direction | Z direction | X | Z |
| 1 | 0.367 | 0.300 | 0.260 | 6.06 | 77.74 | | 1 |
| 2 | 0.133 | 0.108 | 0.094 | 71.82 | 2.10 | 1 | |
| 3 | 0.095 | 0.077 | 0.067 | 12.68 | 0.04 | 2 | |
| 4 | 0.054 | 0.044 | 0.038 | 0.03 | 4.46 | | 3 |
| 5 | 0.045 | 0.037 | 0.032 | 7.47 | 7.75 | 3 | 2 |

b) Xb

| Mode No | Natural period(sec) | | | Effective mass ratio (%) | | Order | |
|------------|---------------------|---------|---------|--------------------------|-------------|-------|---|
| | $\nu=2$ | $\nu=3$ | $\nu=4$ | X direction | Z direction | X | Z |
| 1 | 0.356 | 0.290 | 0.252 | 6.86 | 77.42 | 3 | 1 |
| 2 | 0.131 | 0.107 | 0.092 | 70.50 | 2.70 | 1 | |
| 3 | 0.093 | 0.076 | 0.066 | 14.09 | 0.13 | 2 | |
| 4 | 0.054 | 0.044 | 0.038 | 0.11 | 3.97 | | 3 |
| 5 | 0.044 | 0.036 | 0.031 | 6.63 | 7.98 | | 2 |

c) Wa

| Mode No | Natural period(sec) | | | Effective mass ratio (%) | | Order | |
|------------|---------------------|---------|---------|--------------------------|-------------|-------|---|
| | $\nu=2$ | $\nu=3$ | $\nu=4$ | X direction | Z direction | X | Z |
| 1 | 0.361 | 0.295 | 0.256 | 4.55 | 88.91 | | 1 |
| 2 | 0.128 | 0.104 | 0.090 | 72.98 | 1.60 | 1 | |
| 3 | 0.100 | 0.082 | 0.071 | 15.59 | 0.27 | 2 | |
| 4 | 0.057 | 0.047 | 0.041 | 0.41 | 5.73 | | 2 |
| 5 | 0.045 | 0.036 | 0.032 | 5.05 | 2.13 | 3 | 3 |

d) Wb

| Mode No | Natural period(sec) | | | Effective mass ratio (%) | | Order | |
|------------|---------------------|---------|---------|--------------------------|-------------|-------|---|
| | $\nu=2$ | $\nu=3$ | $\nu=4$ | X direction | Z direction | X | Z |
| 1 | 0.350 | 0.286 | 0.248 | 5.29 | 88.68 | 3 | 1 |
| 2 | 0.126 | 0.103 | 0.089 | 71.34 | 2.13 | 1 | 3 |
| 3 | 0.099 | 0.081 | 0.070 | 17.76 | 0.48 | 2 | |
| 4 | 0.057 | 0.047 | 0.040 | 0.21 | 5.24 | | 2 |

5. Time history response against seismic motions

The dynamic elasto-plastic behaviors are estimated by the geometrical and material nonlinear analysis [Ref.5, 6]. The input seismic waves are artificial waves; BCJ (The Building Center of Japan) level 2 and the two sin waves of the 1st natural periods and the 110% of 1st ones. They are denoted as BCJ-L2, SIN and SIN10 respectively. The acceleration data from 0 to 60 second of BCJ-L2 are adopted. The velocity response spectrum at 2% damping ratio is shown in Figure 6. The sinusoidal waves are 20 seconds including the period of 4 seconds amplification. The sinusoidal wave SIN10 is adopted to study the effect of lengthening natural periods by structural plasticization. Consequently, the effect was not confirmed in the present work.

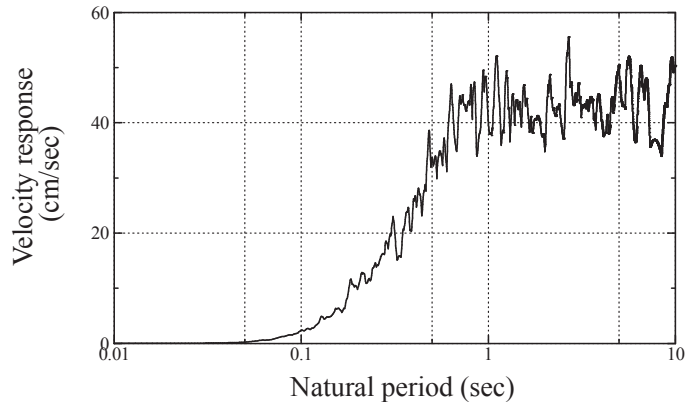


Fig.6 Velocity response spectrum of BCJ-L2

The relationships between maximum input accelerations and maximum vertical displacements are shown in Figure 7. The tensile yield model b shows larger values than the compressive yield model a. The compressive yield models, especially models Wa show dynamic collapse phenomenon representing a sudden increase of displacements.

The relationships of the strain energy and potential energy are shown in Figure 8. In the figure the curves given by the static pushover analyses are also drawn as gray color lines. The black triangle marks represents the initial yield point in the static analyses. The curves by time history analyses almost coincide with the static curves until reaching the initial yield point. After the initial yield, the time history responses are above the static results as for model Xa & Wa showing compressive failure. The two results are not so different for Xb & Wb showing tensile failure.

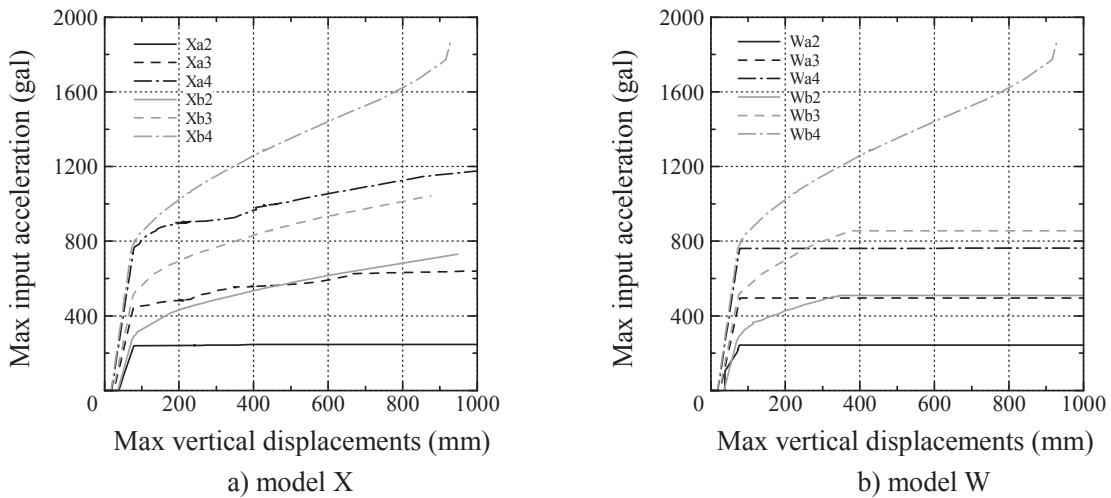


Fig.7 Maximum input acceleration and maximum vertical displacement (BCJ-L2)

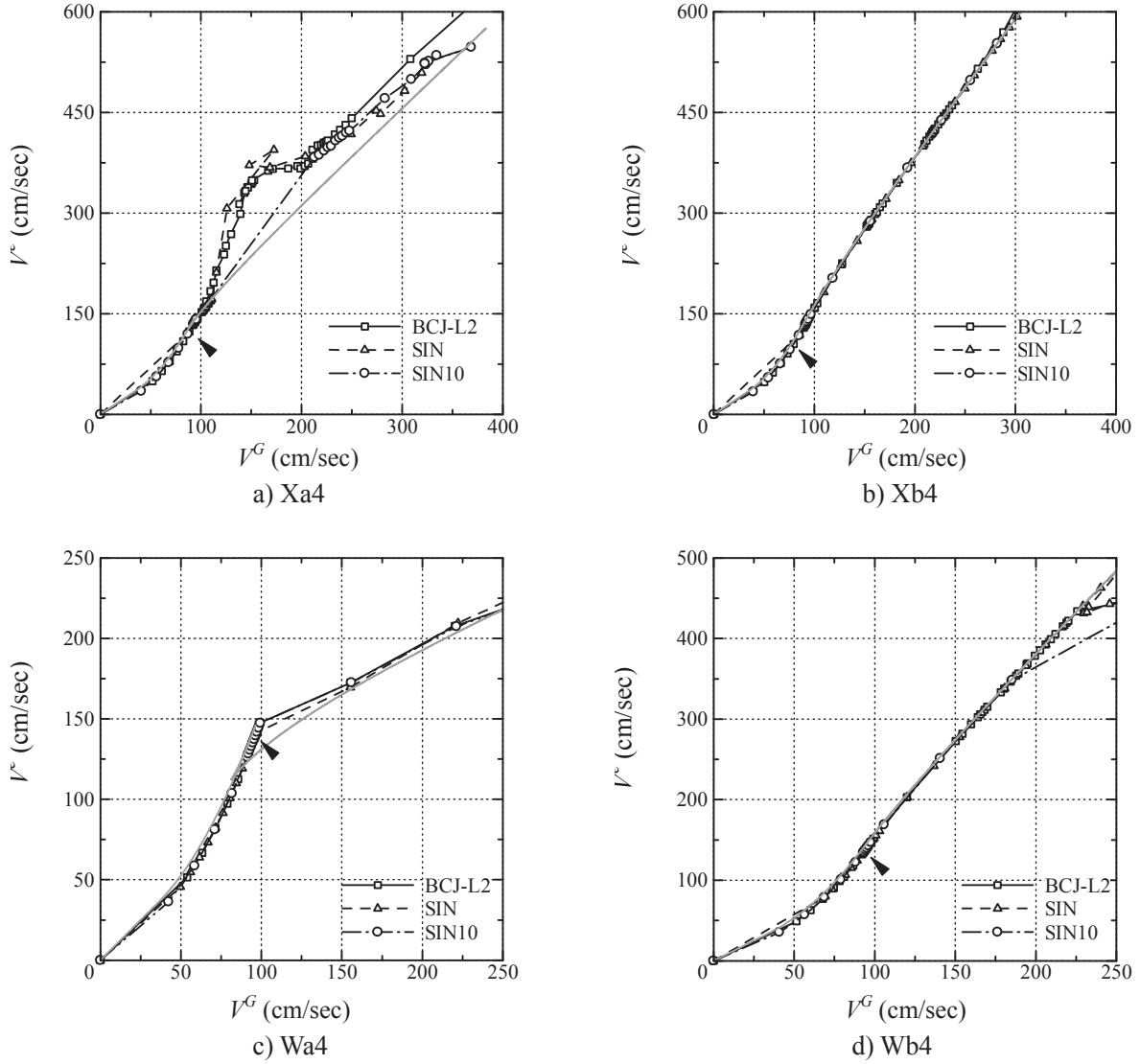


Fig.8 Relationships between V^e and V^G

6. Effect of static safety factors on ultimate seismic resistance capacity

The ratio V_{GY}/V_{LE} given by the time history analyses are compared with the ratio ${}_sV_{GY}/{}_sV_{LE}$ given by the static analyses, as shown in Figure 9. The relationships of both ratios might be on the diagonal line $y=x$, if the dynamic effect would be negligible. However the model Xa shows the rise from the diagonal line $y=x$ and some dynamic effect is confirmed. The rise amount and the ratio ${}_sW_e/{}_sW_p$ are listed in Table 4. Although the model Xa2 and Wa show clearly dynamic collapse, the limit state deformation determined by the factor α was adopted in order to compare with each other. The rise amount b becomes larger as the safety factor ν is larger, for compressive yield model Xa & Wa. It may be due to the reason that the hysteresis dissipation energy becomes larger as the dead load is smaller. The rise amount b is small as for tensile yield model Xb & Wb, regardless of any seismic wave and safety factor ν .

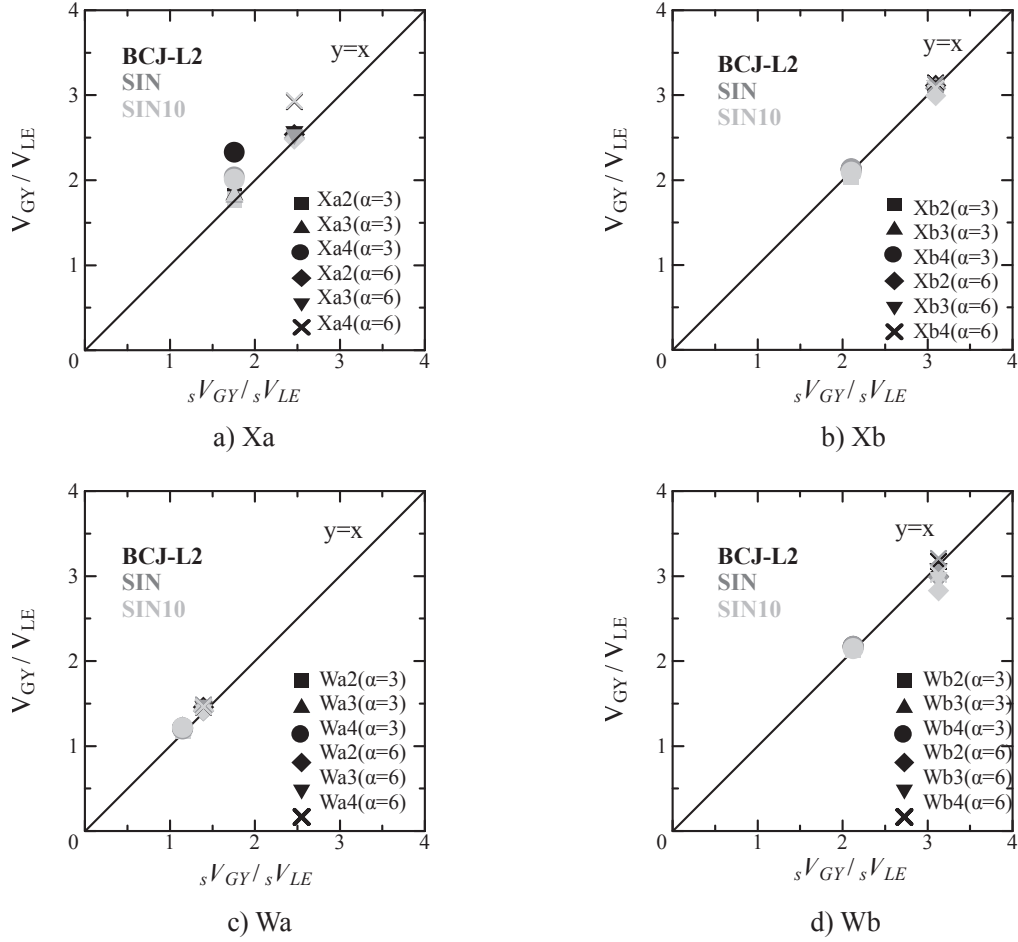


Fig.9 Relationship between sV_{GY}/sV_{LE} & V_{GY}/V_{LE}

Table 4 Rise amount b and sW_e/sW_p

| Model | Safety factor v | $\alpha=3.0$ | | | | $\alpha=6.0$ | | | |
|-------|----------------------|--------------------------|-------|-------|-------------|--------------------------|-------|-------|-------------|
| | | Rise amount b from $y=x$ | | | sW_e/sW_p | Rise amount b from $y=x$ | | | sW_e/sW_p |
| | | BCJ-L2 | SIN | SIN10 | | BCJ-L2 | SIN | SIN10 | |
| Xa | 2 | 0.05 | 0.02 | 0.01 | 0.21 | 0.08 | 0.03 | 0.02 | 0.15 |
| | 3 | 0.07 | 0.04 | 0.06 | 0.21 | 0.11 | 0.07 | 0.06 | 0.15 |
| | 4 | 0.57 | 0.28 | 0.25 | 0.21 | 0.46 | 0.41 | 0.47 | 0.15 |
| Xb | 2 | 0.01 | -0.02 | -0.07 | 0.30 | 0.02 | -0.01 | -0.10 | 0.12 |
| | 3 | 0.00 | -0.01 | -0.03 | 0.30 | 0.02 | 0.00 | -0.03 | 0.12 |
| | 4 | 0.02 | 0.03 | -0.01 | 0.30 | 0.05 | 0.03 | -0.01 | 0.12 |
| Wa | 2 | 0.05 | 0.02 | 0.02 | 0.06 | 0.06 | 0.02 | 0.03 | 0.04 |
| | 3 | 0.07 | 0.08 | 0.03 | 0.06 | 0.07 | 0.09 | 0.04 | 0.04 |
| | 4 | 0.06 | 0.05 | 0.07 | 0.06 | 0.07 | 0.09 | 0.07 | 0.04 |
| Wb | 2 | 0.05 | 0.04 | 0.01 | 0.29 | -0.13 | -0.14 | -0.30 | 0.12 |
| | 3 | 0.04 | 0.04 | 0.06 | 0.29 | -0.04 | -0.05 | -0.14 | 0.12 |
| | 4 | 0.04 | 0.05 | 0.02 | 0.29 | 0.05 | 0.08 | -0.11 | 0.12 |

The differences between the strain energy at dynamic behavior and static behavior are shown in Figure 10, to study the relationships of the rise amount b and components of strain energy. The data treated is at the limit state deformations. In the vertical axis, Δ represents the difference between the dynamic results and static ones. In the figures, the interrelation is confirmed for total strain energy ratio $\Delta E^e/sE^e$ (Fig.10a) and plastic energy ratio $\Delta W_{p/s}W_p$ (Fig.10c) and any interrelation is not confirmed for elastic strain energy ratio $\Delta W_{e/s}W_e$ (Fig.10b), against rise amount b . Since some interrelation is confirmed between $\Delta E^e/sE^e$ and $\Delta W_{p/s}W_p$ (Fig.10d), the increase of strain energy at dynamic behavior is due to the dissipation energy by plastic deformations.

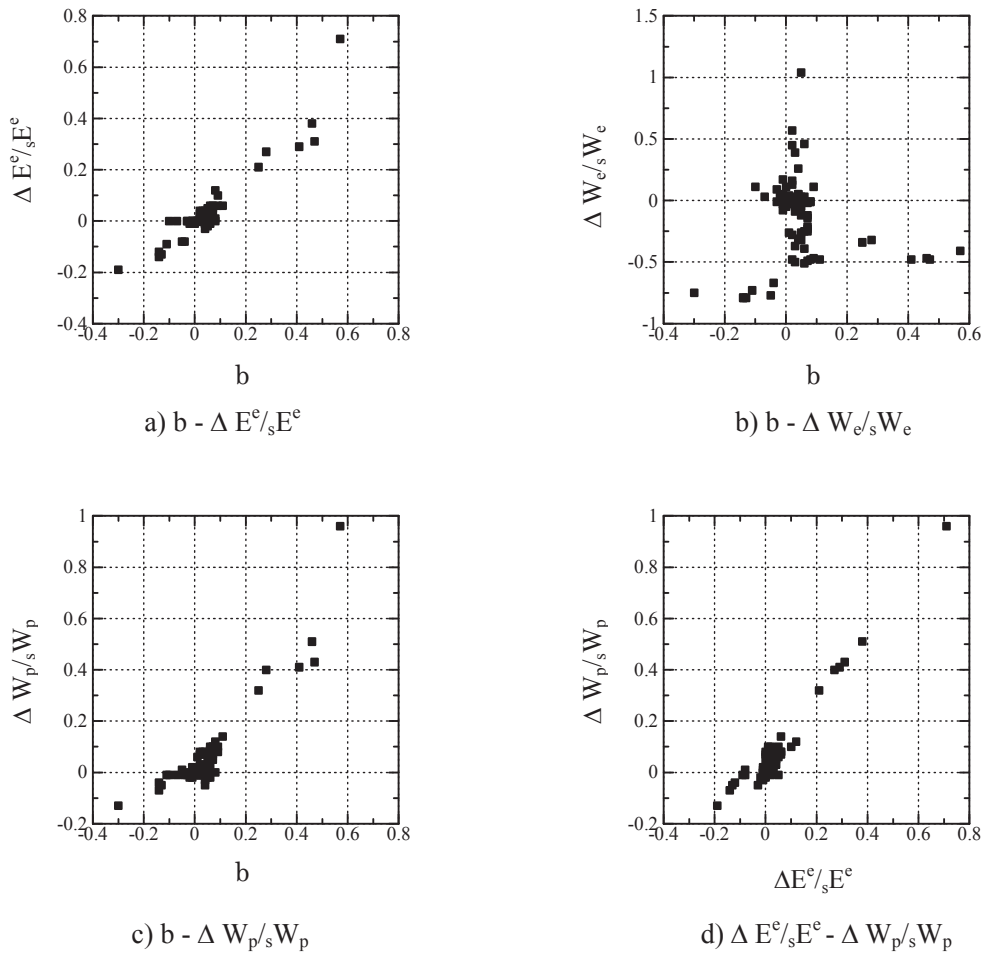


Fig.10 Rise amount b and $\Delta E^e/sE^e$, $\Delta W_{e/s}W_e$, $\Delta W_{p/s}W_p$

Then the relationships between $\Delta W_{p/s}W_p$ and the rise amount b are illustrated for each model and safety factor, as shown in Figure 11.

In Figure 11, the tensile yield models Xb and Wb are distributed in the small range of two axes. However, the compressive yield models Xa and Wa are widely distributed in the positive range of horizontal axis. The fact may be due to the plastic dissipation energy by yield hinges in compressive members. As the safety factors being larger, they are distributed in the right and upper range of the figures. It should be noted that any interrelation was not confirmed between the dissipation energy of damping and rise amount b .

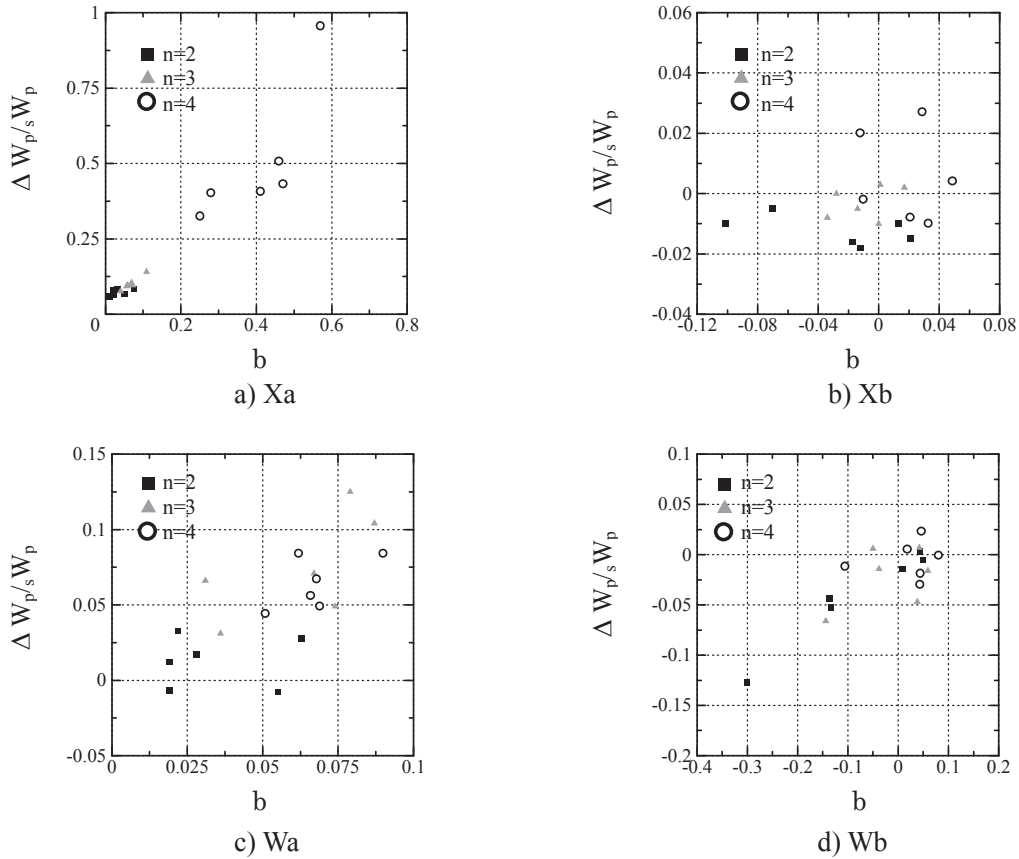


Fig.11 Rise amount b - $\Delta W_{p/s}/W_p$

7. Estimation method of ultimate seismic capacity

The previous results of Ref.5 are combined with the present work to investigate the effect of safety factor ν on the rise amount b . The previous results are listed in Table 5 for lattice arch and double layer cylindrical lattice roof as shown in Figure 12. The letter P denotes both pin supports and PR denotes pin supports and roller supports. The number 1 represents all member sections being equal and number 2 represents members consisting of several section properties. The same relationships are confirmed between the rise amount b and member yield type. As for model PR2, although the static result shows tensile yield, the dynamic behavior includes compressive member yield to increase the rise amount b than model PR1.

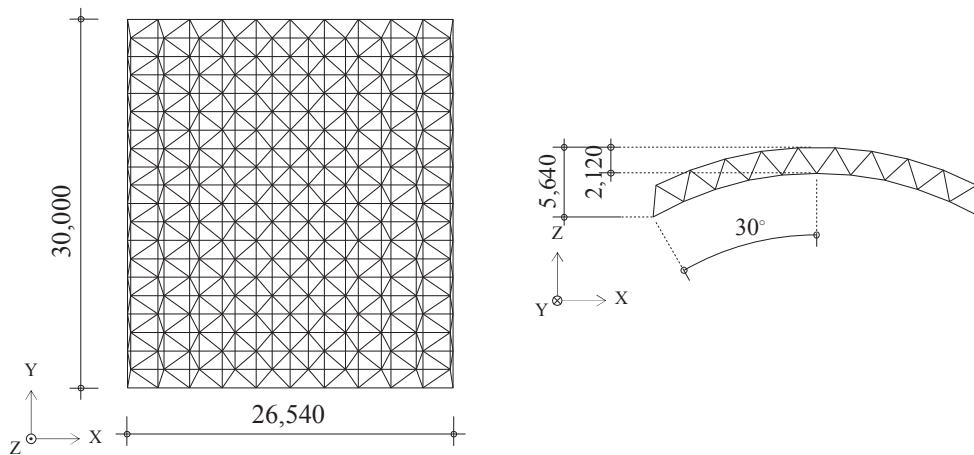


Fig.12 Double-layer cylindrical lattice roof of Ref.5

Table 5 Previous results of lattice arch and double layer cylindrical lattice roof [Ref.5]

| Model | | Safety factor ν | $\frac{sV_{GY}}{sV_{LE}}$ | V_{GY}/V_{LE} | | | Rise amount b from $y=x$ | | | $\frac{sW_e}{sW_p}$ | α |
|---------------------------|------|---------------------|---------------------------|-----------------|------|-------|--------------------------|------|------|---------------------|----------|
| | | | | BCJ-L2 | KOBE | TAFT | BCJ-L2 | KOBE | TAFT | | |
| Plane lattice arch | P1 | 9.68 | 1.74 | 1.82 | 1.89 | — | 0.08 | 0.15 | — | 0.01 | 3.0 |
| | | | 1.99 | 2.80 | 2.64 | — | 0.80 | 0.65 | — | 0.01 | 6.0 |
| | P2 | 10.51 | 1.29 | 1.48 | 1.55 | — | 0.19 | 0.27 | — | 0.07 | 3.0 |
| | | | 1.58 | 2.01 | 1.78 | — | 0.44 | 0.21 | — | 0.02 | 6.0 |
| | PR1 | 5.17 | 1.28 | 1.33 | 1.47 | — | 0.06 | 0.19 | — | 0.03 | 3.0 |
| | | | 1.58 | 1.61 | 1.73 | — | 0.04 | 0.15 | — | 0.01 | 6.0 |
| PR2 | 3.56 | 2.08 | 2.07 | 2.71 | — | -0.01 | 0.63 | — | 0.29 | 3.0 | |
| | | 3.05 | 2.93 | 3.85 | — | -0.12 | 0.81 | — | 0.14 | 6.0 | |
| Double-layer lattice roof | SSR1 | 6.34 | 1.51 | 2.61 | 2.46 | 2.49 | 1.10 | 0.95 | 0.98 | 0.13 | 3.0 |
| | | | 1.97 | 3.08 | 2.65 | 3.36 | 1.11 | 0.68 | 1.39 | 0.05 | 6.0 |
| | SSR2 | 6.99 | 1.42 | 2.65 | 2.21 | 2.11 | 1.23 | 0.79 | 0.70 | 0.10 | 3.0 |
| | | | 1.82 | 2.65 | 2.42 | 2.29 | 0.83 | 0.60 | 0.47 | 0.04 | 6.0 |

The total results of compressive yield models are plotted in Figure 13, according to Eqn. 3 [Ref.5]. The horizontal axis represents the rise amount b that means the increase ratio of dynamic results against static results. The vertical axis represents the strain absorption property of structures at a limit state deformation.

$$\alpha \cdot \frac{sW_e}{sW_p} = k \cdot b \quad (3)$$

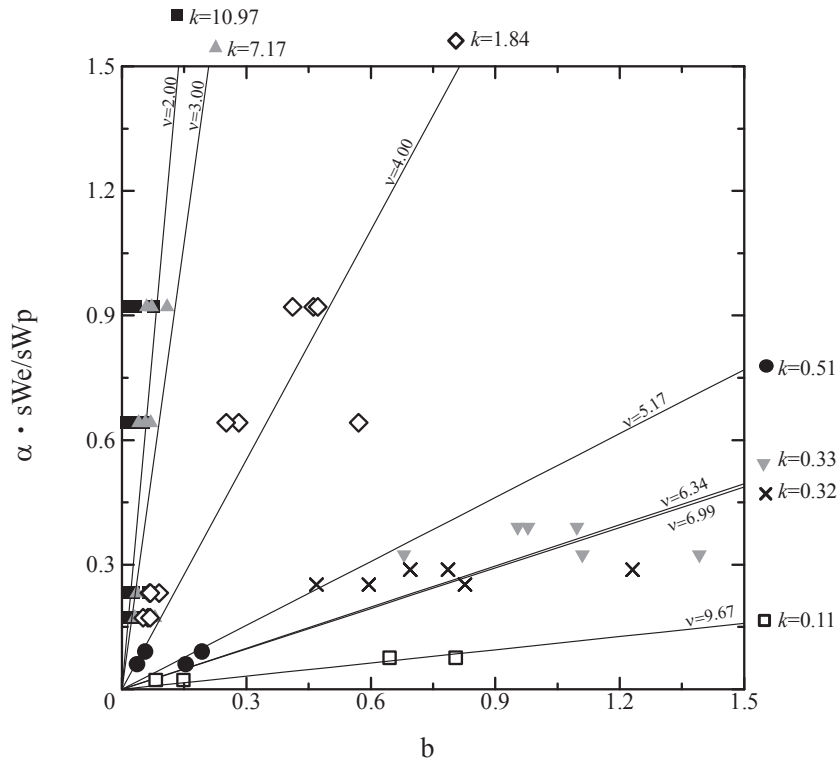


Fig.13 Relationships between rise amount b and $\alpha \cdot sW_e/sW_p$

In Figure 13, the data of Figure 9 and Tables 4 & 5 is plotted, and the safety factor ν and the slope k in Eqn.3 are shown. As larger the safety factor ν is, the slope k becomes smaller. It shows that the large safety factors enlarge the rise amounts, because more dissipation energy by cyclic deformations is occurred until a limit state, consequently the rise amount b becomes large.

In order to study the value of slope k , the relationships of slope k and safety factor ν is drawn in Figure 14. The slope k can be estimated with the safety factor since the correlation coefficient is large.

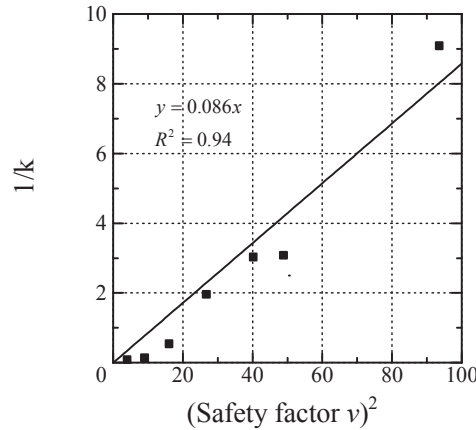


Fig.14 Relationships between safety factor ν and $1/k$

Consequently the ultimate seismic capacity can be accurately estimated with the information of ${}_sW_e/{}_sW_p$ given by a static pushover analysis and the limit state deformation factor α decided by a designer. The value estimated is finally modified by the static safety factor ν .

The flow chart of the estimation method presented is shown as follows and Figure 15.

Step I: The static elasto-plastic behavior is estimated under the vertical loads corresponding to the distribution of mass, until the static absorbed energy of Eqn.2 shows maximum value or the limit state deformation are reached. The elastic component of strain energy ${}_sW_e$ and the plastic dissipation energy ${}_sW_p$ are calculated at the limit state.

Step II: The seismic motion level at which structures become in initial yield can be estimated with the equivalent velocity ${}_sV_{LE}$ and the velocity response spectrum of seismic waves. The equivalent velocity ${}_sV_{LE}$ is determined at initial yield by the pushover analysis. If the natural mode of the largest effective mass ratio would be adopted, the value estimated might be in the safety region [Ref.5].

Step III: The seismic motion level at which structures reach the limit state deformation can be estimated with the value ${}_sV_{GY}/{}_sV_{LE}$. The seismic motion level obtained at the step II may be multiplied by this value to obtain the seismic motion level corresponding to the limit state deformation. If the value ${}_sV_f$ is adopted instead of ${}_sV_{GY}$, the seismic motion level of dynamic collapse could be obtained.

Step IV: The value obtained at the IIIrd step could be modified by the rise amount b that could be given by Equation 3 and Figure 13. The modification with the rise amount b is not necessary on the case that structures would reach a limit state deformation by tensile member yield.

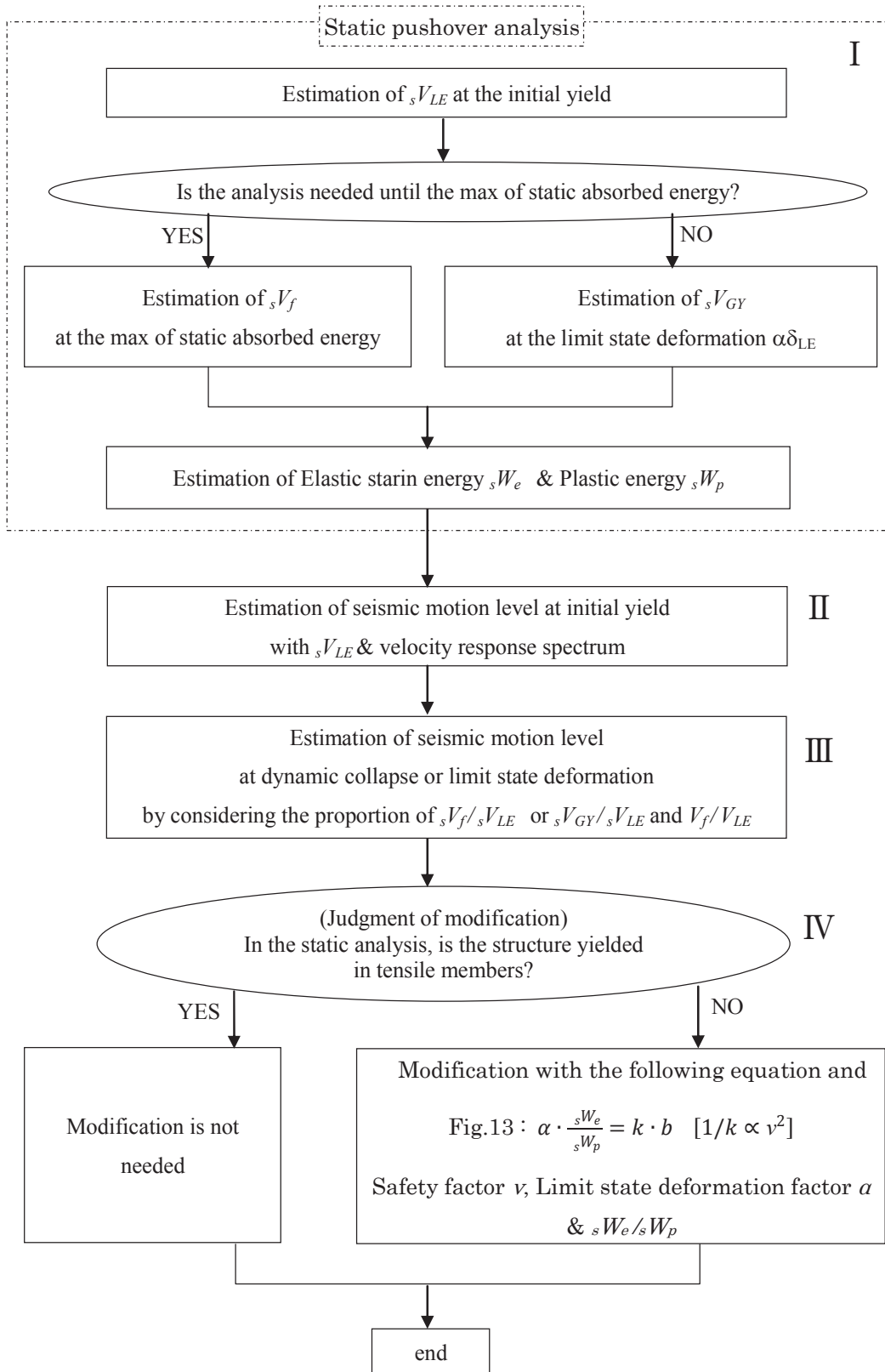


Fig.15 Flow chart of estimation method for ultimate seismic capacity

8. Conclusions

The main conclusions in the present work are listed as follows:

- (1) The equivalent velocities V_f , V_{GY} of strain energy at which structures reach dynamic collapse or a limit state deformation could be accurately estimated with the static safety factor ν being the ratio of initial yield load against dead load.
- (2) The increase of V_f , V_{GY} , at the case that structures are subjected to the seismic motion level corresponding to dynamic collapse or a limit state deformation, is due to the plastic dissipation energy. The effect is small at the conditions that the static safety factor ν is small or structures are in tensile yield.
- (3) The ultimate seismic capacity can be estimated by Figure 15 without any time history analysis.

Acknowledgments

The author gives special thanks to Ms. Risa FUKUSHIMA and Ms. Yuki KADOTSUKA for their numerical works. This work is partially supported by Project Research 2010 of Graduate School of Engineering, Osaka City University and JSPS KAKENHI Grant Number 24656325, Grants-in-Aid for Exploratory Research, Japan.

References

- [1] George W. Housner, Limit Design of Structures to Resist Earthquakes, Proceedings of the World Conference on Earthquake Engineering, Berkley, California, pp.5-1 – 5-13, 1956.
- [2] Ben Kato and Hiroshi Akiyama, Energy Input and Damages in Structures subjected to Sever Earthquakes, Transactions of Architectural Institute of Japan, No.235, pp.9-18, 1975.
- [3] Tada, M., Hayashi, M. and Yoneyama, T., An Improvement of Seismic Capacity of Double-Layer Space Trusses using Force Limiting Devices, Spatial Structures: Heritage, Present and Future, Proc. of the IASS International Symposium, Vol.2, Italy, pp.1085-1092, 1995.
- [4] Qiao, F., Hagiwara, N. and Matsui, T., On the Relation between Absorbed Energy and Dynamic Collapse of a Single-Layer Shallow Latticed Domes, Journal of Structural and Construction Engineering (Transactions of AIJ), No.531, pp.117-124, 2000.
- [5] Yoshiya Taniguchi, Seismic Motion Level of Dynamic Collapse or Limit State Deformation for Lattice Arch and Cylindrical Roof, Abstract Book and CD-ROM of Structural Engineers World Congress, Como, Italy, 2011, p.176.
- [6] SPACE, <http://wwwra.meijo-u.ac.jp/labs/ra007/space/index.htm>, (Prof. Masaru Murata, Meijo University, Japan).

CITIZEN AWARENESS OF COMMUNITY BUSES FROM THE PUBLIC SUPPORT PERSPECTIVE

Yusuke KURASHIMA* and Takashi UCHIDA**

(Received September 30, 2012)

Synopsis

A large amount of public support is devoted to public transport every year. It is a highly public business related to contributions of residents' funding. It is therefore important to acquire an understanding of the business by grasping and using resident awareness.

This study was conducted to ascertain resident awareness for use as basic information. Multivariate analyses of public-transport-related questionnaire responses of Izumi, Osaka residents clarified actual conditions of resident awareness related to public support.

KEYWORDS: Public support, Citizen awareness, Transport policy, Questionnaire, Multivariate analysis

1. Research Background and Objectives

(1) Background

Community buses often operate to eliminate blank areas and compensate routes that are withdrawn because they are unprofitable. Community buses are necessary in a region from the viewpoint of an increase in people whose transportation is constrained by the aging society, and to secure transportation in regions where maintenance is an extremely important issue.

In addition, profitability is difficult to achieve solely by fare income. In many areas, it is maintained through substantial public support. Even through diversification of transfers and destinations, large increases in users can no longer be expected. Maintaining public support is extremely important. Considering public support circumstances such as these necessitates that we ascertain the structure of the problem in terms of attitudes and perceptions of the region for the community bus as resident awareness.

Because public transportation maintenance using a large amount of public support includes benefits and shortcomings, it is important for many actors involved in community buses such as the government, bus companies, and residents to have awareness with respect to public support and maintenance. To take advantage of that awareness, it is necessary for the public to suggest appropriate measures and declare their intentions for it.

When characterizing residents, it is important to grasp the awareness of groups that do not present their intentions positively. In general, the purpose of grasping resident attitudes is to ascertain perceptions and attitudes

* Student, Doctor Course of Department of Civil Engineering

** Professor, Department of Civil Engineering

related to certain issues: so-called public awareness and involvement. Regarding public involvement assessment, techniques can be organized as presented in Table 1. Questionnaires are useful with cases for a wide range of areas, and they are useful to collect basic information with little bias.

Table 1 Assessing public involvement

| Level | Technique |
|-----------------------------------|---|
| 1) Information gathering | <ul style="list-style-type: none"> • Questionnaire survey • Hearing survey • Resource acquisition |
| 2) Public information | <ul style="list-style-type: none"> • Radio, TV, Newspaper, Public information magazine, Web • Distribution of documents, Pamphlets • Exhibition • Seminar, briefing session |
| 3) Conference | <ul style="list-style-type: none"> • Public hearing • Workshop • Open house • Opinions offered by FAX, postcard, email |
| 4) Involvement in decision-making | <ul style="list-style-type: none"> • Brainstorming, KJ method • Simulation game • Social experiment |

For ascertaining resident awareness in the field of public transport, questionnaires are often used to treat as valid only those responses with declarations of intention that signify agreement or objections. So-called non-declarations of intention responses which show no intentions such as blank responses or *do not know* responses are not analyzed. For assessing resident awareness, examining appropriate methods to handle non-declaration of intention responses is also important.

(2) Objectives of Research

This study was conducted to assess the actual conditions of intentions related to the public support of residents who is demand services. We analyzed the results of the resident questionnaire about public transport (community bus etc.) for the resident of Izumi city in Osaka that consisting of questionnaire items about service and public support on public transport. We grasped as resident awareness for suggestion of an appropriate measure and declaration of intention for it.

2. Research Approach

Figure 1 portrays an overview of the research. The resident questionnaire related to public transport of Izumi city consists of two groups that are available and future use, service and public support of community bus. For analyses, we conducted a cluster analysis and principal component analysis respect of service and public support of community bus intended for the group of declaration of intention (samples that consists of responses such as agree or object).

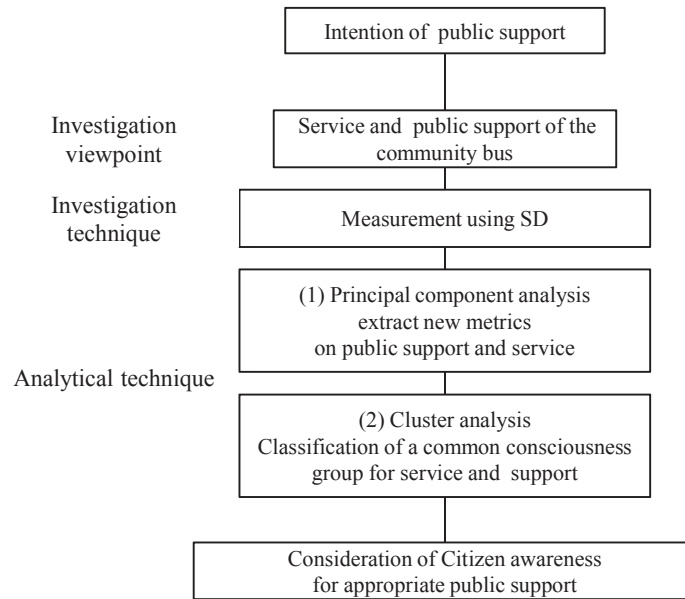


Figure 1 Summary of the study.

3. Outline of the survey

(1) Configuration of the Questionnaire

We produced questionnaires of two types (North and Central edition; South edition) and distributed them to households that subscribe to the town council of the city. For this study, we used a version of the North and Central edition, as summarized in August 2012.

As shown in Table 2, we provided information about the community bus and asked 18 questionnaire items about community bus status, such as the use of taxes to support them, and elicited six responses as follows: strongly object (-2), object (-1), neither (0), agree (1), strongly agree (+2), and *do not know* (DK).

Table 2 Information given in the questionnaire introduction

| | Information |
|---|--|
| 1 | Actual circumstances of the service and the use of the community buses |
| 2 | Actual circumstances of income and expenditure and public support |
| 3 | Importance of maintaining community buses and stringency of the income and expenditure circumstances |
| 4 | Importance of ascertaining resident awareness for examining ways of managing future community buses |
| 5 | Benefits and shortcomings related to public support |

Table 3 Questionnaire items related to service and public support of community buses

| Questionnaire Items | |
|---------------------|---|
| 1 | Routes and deficits should be reduced. |
| 2 | For securing transportation, the current deficit can't be helped. |
| 3 | Even if deficits increase, in addition to the four current routes, community buses should run in other districts. |
| 4 | Community buses should be abolished because they impose a tax burden. |
| 5 | Number of services and deficits should be reduced. |
| 6 | Fares should be cut to increase users. |
| 7 | Not interested in using community buses as a resident. |
| 8 | The number of services should be increased even if deficits increase. |
| 9 | For securing transportation, even if deficits increase, it can't be helped. |
| 10 | Fares should be raised to reduce deficits. |
| 11 | Numbers of services and users should be increased. |
| 12 | More public information and advertising should be done to increase users. |
| 13 | Present fares are too low. |
| 14 | Because they are inconvenient, I do not use buses. |
| 15 | I use buses to the greatest extent possible and want to cooperate to decrease deficits. |
| 16 | I think that the frequency of my own use will increase if the number of services increases. |
| 17 | For cancellation of areas not served by public transport, modes aside from community buses should be considered. |
| 18 | I am proud that Izumi-shi has community buses. |

(2) Survey results

Table 5 presents an overview of the survey results. Distribution of the North and Central edition was done to 45,000 households, from which responses were obtained from 39.2% (17,310 households), which is equivalent to approximately 94% of the total number of collection, including the South edition. It is equivalent to about 25% of all city households including those which are not town council members.

Table 4 Overview of the survey (North and Central edition)

| | |
|--|-------------------------------|
| Period for distribution | November 2010 – January 2011 |
| Period for collection | December 2010 – February 2011 |
| Number of the distribution (A) *Number of households with a member of the town council. | 44,124 |
| Number collected (B) | 17,310 |
| Recovery (B/A) | 39.2% |

(3) Simple tabulation based on responses about the state of community buses

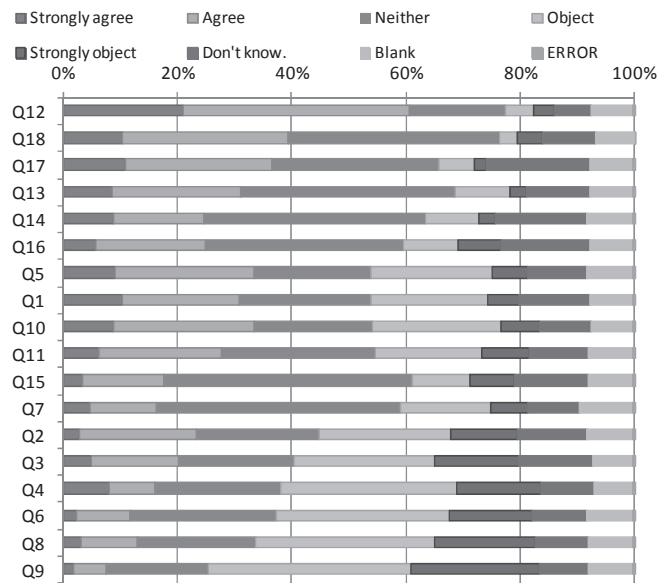


Figure 2 Composition ratios of the responses.

Figure 2 presents results of a simple tabulation of responses. We interpret the trend of the relation between question and benefits and shortcomings, and organized them as shown in Table 5. For all questions, blank and *do not know* responses constituted about 20% of responses. Moreover, in some cases, neither was greater than 40%. Some of these responses are inferred as indicating a so-called "silent majority".

Table 5 Relations of questionnaire items and the benefits and shortcomings

| Intention | Statements |
|--------------------|---|
| Agree | <ul style="list-style-type: none"> • More public information and advertising should be done to increase users (Q12) • I am proud that Izumi-shi has community buses (Q18) • For cancellation of areas not served by public transport, modes aside from community buses should be considered (Q17) • Present fares are too low (Q13) |
| Disagree | <ul style="list-style-type: none"> • For securing transportation, even if deficits increase, it can't be helped (Q9) • The number of services should be increased even if deficits increase (Q8) • Fares should be cut to increase users (Q6) • Community buses should be abolished because they impose a tax burden (Q4) • Even if deficits increase, in addition to the four current routes, community buses should run in other districts (Q3) • For securing transportation, the current deficit can't be helped (Q2) |
| Difficult to judge | <ul style="list-style-type: none"> • Routes and deficits should be reduced (Q1) • Fares should be raised to reduce deficits (Q10) • Numbers of services and users should be increased (Q11) |
| No majority | <ul style="list-style-type: none"> • I am proud that Izumi-shi has community buses (Q18) • Because they are inconvenient, I do not use buses (Q14) • I think that the frequency of my own use will increase if the number of service increases (Q16) • I use buses to the greatest extent possible and want to cooperate to decrease deficits (Q15) • Not interested in using community buses as a resident (Q7) |

4. Actual conditions of the public support intention

(1) Principal component analysis based on responses related to community buses

To extract new metrics on public support and service, we conducted a principal component analysis (PCA) for the group of questionnaire items related to public support and services. In performing the analysis, by setting two cases (Table 6) for how to handle responses with no-declared intentions that are neither, *do not know*, or blank, and make a comparison of results, we also discussed effects of handling results.

Table 6 Cases used for principal component analysis

| Case | Handling of the Non-declaration of intention | Number of samples |
|------|--|-------------------|
| 1 | [Supplement of responses] Substitute zero points for blank responses and <i>do not know</i> , and handle them as null data | 16,888 |
| 2 | [Deletion of responses] Delete samples including blank or <i>do not know</i> responses | 7,644 |

Case 1 uses a pattern that accommodates the non-declaration of intention responses. Therefore, zero is substituted for responses of both blank and *do not know*, and the data are processed. Case 2 shows a pattern for removal of the non-declaration of intention responses. Samples including either or both blank and *do not know* responses were removed from the data used for analyses. Tables 7 and 8 present the respective results.

Regarding a comparison of cases 1 and 2, each principal component score in the first and second principal component shows substantially the same configuration. Furthermore, the third and fourth principal components are similar configurations. From there, in this analysis, we inferred that effects of such handling on results of PCA are slight, even if different methods of handling are used. No difference was found in the interpretation of the principal components, which are presented below.

The first principal component is the "Reduction of public support" as a composite index.

The second principal component is "Lack of interest in buses".

The third principal component is "Support from fare hikes".

The fourth principal component is "Efficiency of business".

Table 7 Results of principal component analysis [Case 1]

| Question | Principal component | | | |
|---|---------------------|--------|--------|--------|
| | first | second | third | fourth |
| 1 Routes and deficits should be reduced. | 0.717 | 0.206 | 0.095 | 0.327 |
| 2 For securing transportation, the current deficit can't be helped. | -0.712 | 0.079 | -0.058 | -0.228 |
| 3 Even if deficits increase, in addition to the four current routes, community buses should run in other districts. | -0.710 | 0.256 | 0.116 | -0.149 |
| 4 Community buses should be abolished because they impose a tax burden. | 0.699 | 0.414 | 0.101 | 0.069 |
| 5 Number of services and deficits should be reduced. | 0.688 | 0.113 | 0.077 | 0.329 |
| 6 Fares should be cut to increase users. | -0.375 | 0.603 | 0.021 | 0.280 |
| 7 Not interested in using community buses as a resident. | 0.416 | 0.474 | 0.171 | -0.018 |
| 8 The number of services should be increased even if deficits increase. | -0.743 | 0.359 | 0.151 | -0.189 |
| 9 For securing transportation, even if deficits increase, it can't be helped. | -0.658 | 0.385 | 0.064 | -0.254 |
| 10 Fares should be raised to reduce deficits. | 0.371 | -0.190 | 0.710 | -0.226 |
| 11 Numbers of services and users should be increased. | -0.690 | 0.229 | 0.317 | 0.047 |
| 12 More public information and advertising should be done to increase users. | -0.510 | -0.235 | 0.263 | 0.347 |
| 13 Present fares are too low. | 0.376 | -0.264 | 0.689 | -0.270 |
| 14 Because they are inconvenient, I do not use buses. | 0.504 | 0.305 | 0.150 | -0.155 |
| 15 I use buses to the greatest extent possible and want to cooperate to decrease deficits. | -0.659 | -0.140 | 0.190 | 0.353 |
| 16 I think that the frequency of my own use will increase if the number of services increases. | -0.702 | 0.016 | 0.286 | 0.289 |
| 17 For cancellation of areas not served by public transport, modes aside from community buses should be considered. | 0.265 | 0.137 | 0.264 | 0.308 |
| 18 I am proud that Izumi-shi has community buses. | -0.679 | -0.308 | 0.072 | 0.212 |
| Eigenvalue | 6.51 | 1.6 | 1.46 | 1.09 |
| Cumulative contribution ratio | 36.18 | 45.08 | 53.2 | 59.27 |

Table 8 Results of principal component analysis [Case 2]

| Question | Principal component | | | |
|---|---------------------|--------|--------|--------|
| | first | second | third | fourth |
| 1 Routes and deficits should be reduced. | 0.744 | 0.216 | -0.003 | 0.318 |
| 2 For securing transportation, the current deficit can't be helped. | -0.738 | 0.022 | -0.054 | -0.249 |
| 3 Even if deficits increase, in addition to the four current routes, community buses should run in other districts. | -0.726 | 0.271 | 0.015 | -0.175 |
| 4 Community buses should be abolished because they impose a tax burden. | 0.751 | 0.361 | -0.054 | 0.068 |
| 5 Number of services and deficits should be reduced. | 0.709 | 0.125 | 0.029 | 0.339 |
| 6 Fares should be cut to increase users. | -0.393 | 0.549 | -0.240 | 0.284 |
| 7 Not interested in using community buses as a resident. | 0.452 | 0.499 | -0.059 | -0.051 |
| 8 The number of services should be increased even if deficits increase. | -0.765 | 0.362 | 0.014 | -0.202 |
| 9 For securing transportation, even if deficits increase, it can't be helped. | -0.687 | 0.331 | -0.047 | -0.261 |
| 10 Fares should be raised to reduce deficits. | 0.388 | 0.089 | 0.755 | -0.137 |
| 11 Numbers of services and users should be increased. | -0.713 | 0.360 | 0.163 | 0.022 |
| 12 More public information and advertising should be done to increase users. | -0.566 | -0.002 | 0.263 | 0.341 |
| 13 Present fares are too low. | 0.403 | 0.047 | 0.742 | -0.218 |
| 14 Because they are inconvenient, I do not use buses. | 0.563 | 0.363 | -0.011 | -0.227 |
| 15 I use buses to the greatest extent possible and want to cooperate to decrease deficits. | -0.693 | -0.058 | 0.223 | 0.387 |
| 16 I think that the frequency of my own use will increase if the number of services increases. | -0.736 | 0.149 | 0.240 | 0.272 |
| 17 For cancellation of areas not served by public transport, modes aside from community buses should be considered. | 0.279 | 0.355 | 0.117 | 0.200 |
| 18 I am proud that Izumi-shi has community buses. | -0.720 | -0.217 | 0.164 | 0.208 |
| Eigenvalue | 7.18 | 1.53 | 1.43 | 1.05 |
| Cumulative contribution ratio | 39.91 | 48.39 | 56.36 | 62.18 |

(2) Cluster analysis based on responses about the state of community buses

Using principal component scores for each case of 3-(1), we performed cluster analysis for classification of collective common sense about the Service and Public Support, in addition to a comparison of each case. Using principal component scores of the principal component for which eigenvalues are equal to or greater than 1.0. Calculations were performed using the ward system. We classified items into five cluster samples. Table 9 shows a representation of color in shades of the component ratio of each response in each classified cluster.

Because high correlation coefficient is seen between the cluster and the cases, it is thought that there is not the big change in a tendency to response to each cluster. However, a difference occurs for the interpretation of the pros and cons because the composition ratio of responses is changes. Furthermore, in the remarkable place, we

can confirm the tendency that composition ratio of responses is biased as 2 or -2 points (Cluster 1 of case 1 and 2). For a case which supplemented responses as in case 1, neither amount is increasing, and the percentage of the cluster of non-declaration of intention becomes very large overall.

Table 9 Composition ratios of respective responses in each classified cluster, in each case

| Case1 | Cluster | | | | | | | | | | | | | | | | | | | | | | | | |
|-------|---------|------|------|------|------|------|------|------|------|------|------|------|------|------|-----|------|------|------|------|------|------|------|------|------|------|
| | 1 | | | | | 2 | | | | | 3 | | | | | 4 | | | | | 5 | | | | |
| Point | 2 | 1 | 0 | -1 | -2 | 2 | 1 | 0 | -1 | -2 | 2 | 1 | 0 | -1 | -2 | 2 | 1 | 0 | -1 | -2 | 2 | 1 | 0 | -1 | -2 |
| 1 | 58.7 | 29.3 | 8.1 | 2.0 | 1.9 | 29.1 | 31.9 | 20.5 | 16.1 | 2.4 | 3.7 | 16.0 | 62.5 | 15.6 | 2.1 | 1.6 | 15.6 | 31.1 | 39.2 | 12.5 | 10.1 | 33.5 | 32.2 | 15.9 | 8.2 |
| 2 | 1.0 | 1.9 | 8.2 | 32.4 | 56.6 | 0.2 | 7.3 | 14.4 | 41.3 | 36.8 | 1.9 | 19.2 | 59.6 | 16.0 | 3.3 | 5.2 | 35.2 | 32.9 | 22.7 | 4.1 | 5.9 | 18.7 | 35.2 | 31.1 | 9.2 |
| 3 | 2.0 | 1.2 | 6.7 | 24.9 | 65.3 | 0.6 | 2.4 | 13.6 | 33.3 | 50.2 | 5.4 | 18.8 | 55.6 | 16.9 | 3.3 | 5.0 | 18.2 | 37.2 | 31.6 | 8.0 | 11.1 | 16.6 | 30.8 | 32.2 | 9.3 |
| 4 | 57.9 | 24.5 | 12.0 | 3.7 | 1.9 | 15.3 | 12.1 | 28.6 | 29.0 | 15.1 | 4.0 | 7.1 | 56.3 | 26.6 | 5.9 | 0.7 | 2.8 | 19.8 | 45.9 | 30.7 | 3.2 | 9.4 | 29.8 | 32.6 | 25.0 |
| 5 | 49.4 | 31.3 | 11.8 | 3.5 | 4.1 | 29.8 | 37.8 | 16.6 | 13.1 | 2.8 | 2.7 | 18.2 | 58.1 | 18.1 | 2.9 | 1.7 | 21.0 | 26.0 | 38.2 | 13.0 | 7.4 | 39.5 | 27.0 | 15.0 | 11.1 |
| 6 | 3.1 | 2.5 | 20.8 | 25.0 | 48.7 | 0.5 | 2.0 | 17.2 | 37.4 | 42.9 | 2.1 | 11.9 | 62.3 | 20.4 | 3.2 | 0.3 | 3.1 | 27.7 | 51.6 | 17.3 | 10.9 | 26.5 | 39.8 | 18.7 | 4.1 |
| 7 | 34.1 | 24.9 | 30.6 | 4.4 | 6.1 | 4.4 | 9.7 | 54.8 | 21.8 | 9.4 | 3.3 | 13.2 | 74.7 | 7.7 | 1.0 | 0.7 | 5.9 | 50.6 | 30.2 | 12.6 | 3.7 | 9.8 | 52.9 | 19.6 | 14.0 |
| 8 | 1.5 | 0.3 | 2.8 | 23.4 | 72.1 | 0.1 | 0.3 | 5.1 | 32.9 | 61.4 | 3.5 | 13.3 | 57.6 | 22.1 | 3.6 | 2.7 | 10.9 | 31.3 | 44.8 | 10.3 | 8.2 | 9.7 | 26.0 | 43.4 | 12.7 |
| 9 | 2.0 | 0.2 | 1.5 | 18.1 | 78.2 | 0.2 | 0.1 | 2.1 | 25.7 | 71.8 | 2.0 | 7.4 | 55.1 | 29.2 | 6.3 | 0.9 | 7.6 | 25.1 | 50.6 | 15.8 | 5.7 | 4.5 | 19.8 | 48.8 | 21.1 |
| 10 | 37.7 | 19.3 | 15.7 | 11.1 | 16.2 | 24.8 | 37.9 | 16.8 | 13.2 | 7.3 | 5.0 | 25.8 | 52.0 | 15.4 | 1.9 | 4.7 | 21.7 | 28.0 | 37.1 | 8.5 | 0.9 | 11.8 | 29.6 | 39.7 | 18.0 |
| 11 | 1.6 | 1.8 | 16.3 | 27.9 | 52.5 | 1.5 | 5.6 | 28.8 | 38.9 | 25.2 | 6.2 | 26.3 | 57.7 | 9.0 | 0.7 | 6.0 | 22.5 | 40.6 | 26.2 | 4.8 | 15.8 | 28.5 | 37.9 | 15.9 | 1.9 |
| 12 | 5.1 | 8.3 | 25.0 | 21.8 | 39.8 | 27.9 | 35.6 | 27.6 | 5.9 | 3.0 | 15.1 | 39.7 | 42.3 | 2.7 | 0.3 | 22.8 | 49.2 | 20.2 | 5.2 | 2.6 | 47.3 | 42.4 | 9.3 | 0.6 | 0.3 |
| 13 | 33.8 | 20.3 | 33.4 | 6.0 | 6.5 | 23.4 | 34.7 | 34.7 | 5.5 | 1.7 | 5.1 | 24.9 | 64.5 | 4.8 | 0.7 | 4.6 | 20.2 | 56.6 | 15.6 | 3.0 | 0.5 | 7.0 | 59.4 | 22.6 | 10.5 |
| 14 | 56.7 | 21.8 | 20.2 | 0.5 | 0.9 | 9.7 | 14.9 | 62.8 | 10.4 | 2.3 | 5.9 | 17.0 | 72.8 | 4.0 | 0.3 | 3.4 | 14.1 | 60.4 | 17.0 | 5.0 | 3.7 | 12.1 | 55.2 | 18.7 | 10.2 |
| 15 | 0.5 | 0.1 | 12.6 | 23.0 | 63.8 | 2.2 | 10.3 | 64.0 | 13.7 | 9.7 | 1.3 | 11.4 | 76.8 | 8.3 | 2.2 | 3.9 | 18.9 | 60.9 | 11.6 | 4.7 | 14.4 | 29.8 | 52.5 | 2.9 | 0.5 |
| 16 | 0.4 | 0.4 | 17.9 | 21.3 | 60.1 | 2.2 | 8.2 | 60.7 | 16.1 | 12.9 | 4.5 | 21.0 | 66.8 | 6.4 | 1.4 | 6.3 | 20.8 | 54.9 | 12.6 | 5.5 | 19.4 | 31.6 | 46.2 | 2.3 | 0.5 |
| 17 | 43.4 | 23.0 | 22.6 | 3.5 | 7.5 | 19.7 | 29.7 | 42.1 | 6.8 | 1.6 | 6.8 | 24.4 | 65.7 | 2.8 | 0.3 | 4.1 | 20.8 | 56.8 | 14.3 | 3.9 | 16.2 | 38.0 | 38.9 | 4.6 | 2.2 |
| 18 | 0.1 | 0.9 | 35.0 | 18.9 | 45.1 | 9.7 | 27.4 | 53.3 | 5.5 | 4.1 | 5.3 | 25.0 | 67.1 | 1.8 | 0.8 | 16.7 | 41.8 | 38.2 | 1.7 | 1.6 | 27.0 | 35.5 | 36.1 | 1.0 | 0.3 |



| Case2 | Cluster | | | | | | | | | | | | | | | | | | | | | | | | |
|-------|---------|------|------|------|------|------|------|------|------|------|------|------|------|------|------|------|------|------|------|------|------|------|------|------|------|
| | 1 | | | | | 2 | | | | | 3 | | | | | 4 | | | | | 5 | | | | |
| Point | 2 | 1 | 0 | -1 | -2 | 2 | 1 | 0 | -1 | -2 | 2 | 1 | 0 | -1 | -2 | 2 | 1 | 0 | -1 | -2 | 2 | 1 | 0 | -1 | -2 |
| 1 | 28.2 | 44.1 | 22.8 | 3.8 | 1.1 | 22.5 | 32.9 | 23.9 | 16.9 | 3.7 | 0.9 | 9.0 | 53.0 | 29.3 | 7.7 | 3.2 | 9.6 | 18.9 | 49.7 | 18.7 | 14.3 | 24.6 | 22.4 | 30.5 | 8.2 |
| 2 | 0.3 | 5.4 | 21.6 | 46.6 | 26.2 | 2.3 | 14.6 | 20.5 | 36.6 | 26.0 | 6.3 | 36.1 | 48.6 | 7.8 | 1.3 | 9.2 | 43.6 | 20.9 | 18.7 | 7.7 | 3.3 | 25.1 | 23.1 | 31.8 | 16.7 |
| 3 | 1.3 | 3.4 | 16.0 | 46.6 | 32.6 | 5.3 | 12.2 | 19.5 | 35.5 | 27.5 | 13.5 | 35.5 | 44.5 | 6.0 | 0.5 | 6.3 | 22.4 | 29.0 | 27.1 | 15.1 | 4.2 | 13.0 | 24.7 | 34.6 | 23.5 |
| 4 | 24.2 | 25.6 | 35.3 | 13.2 | 1.8 | 19.1 | 13.3 | 31.8 | 26.0 | 9.9 | 0.4 | 2.2 | 39.7 | 41.2 | 16.6 | 2.3 | 1.3 | 6.7 | 46.6 | 43.0 | 6.2 | 5.4 | 15.2 | 42.6 | 30.6 |
| 5 | 21.5 | 47.0 | 23.0 | 5.4 | 3.1 | 20.4 | 34.0 | 21.0 | 19.3 | 5.4 | 0.6 | 9.0 | 47.7 | 33.1 | 9.5 | 3.4 | 16.2 | 14.0 | 45.0 | 21.4 | 13.0 | 32.7 | 18.5 | 26.8 | 9.0 |
| 6 | 3.0 | 8.7 | 36.9 | 34.5 | 16.9 | 1.4 | 4.4 | 21.9 | 40.9 | 31.4 | 6.6 | 25.2 | 53.4 | 12.8 | 2.0 | 0.3 | 2.6 | 17.9 | 49.5 | 29.8 | 1.9 | 7.1 | 26.9 | 43.1 | 21.0 |
| 7 | 13.8 | 29.2 | 47.9 | 6.5 | 2.6 | 11.4 | 15.6 | 53.5 | 13.6 | 5.9 | 2.2 | 10.5 | 65.8 | 17.1 | 4.5 | 0.7 | 2.4 | 35.9 | 41.1 | 19.8 | 2.1 | 4.3 | 40.1 | 35.0 | 18.5 |
| 8 | 1.0 | 1.0 | 13.1 | 48.6 | 36.4 | 3.8 | 8.7 | 16.3 | 40.6 | 30.6 | 10.8 | 27.5 | 52.6 | 8.8 | 0.3 | 3.2 | 12.2 | 26.1 | 39.4 | 19.1 | 2.0 | 7.4 | 18.6 | 44.3 | 27.7 |
| 9 | 0.8 | 1.0 | 6.9 | 47.8 | 43.5 | 2.8 | 3.8 | 13.2 | 41.9 | 38.4 | 6.3 | 18.0 | 55.4 | 18.9 | 1.5 | 2.7 | 11.0 | 22.8 | 40.8 | 22.8 | 0.7 | 3.3 | 14.3 | 45.7 | 36.1 |
| 10 | 4.8 | 14.3 | 33.1 | 32.5 | 15.2 | 33.4 | 56.8 | 8.4 | 1.3 | 0.1 | 0.7 | 9.6 | 48.6 | 32.6 | 8.5 | 4.6 | 7.0 | 14.4 | 53.0 | 21.0 | 8.4 | 33.5 | 22.7 | 27.9 | 7.5 |
| 11 | 0.6 | 6.1 | 32.6 | 38.5 | 22.1 | 8.1 | 21.9 | 30.3 | 23.2 | 16.5 | 15.5 | 42.9 | 39.8 | 1.8 | 0.0 | 5.7 | 19.9 | 29.3 | 31.3 | 13.8 | 6.4 | 21.1 | 34.3 | 28.7 | 9.4 |
| 12 | 6.6 | 31.7 | 30.5 | 16.9 | 14.3 | 22.8 | 40.4 | 21.6 | 5.7 | 9.4 | 26.1 | 48.2 | 24.7 | 0.9 | 0.2 | 22.9 | 43.6 | 18.4 | 8.3 | 6.9 | 38.2 | 46.5 | 12.7 | 1.8 | 0.7 |
| 13 | 3.8 | 14.3 | 63.1 | 13.1 | 5.8 | 32.8 | 52.7 | 14.3 | 0.2 | 0.1 | 0.9 | 9.0 | 33.9 | 12.6 | 3.6 | 5.1 | 9.7 | 44.9 | 29.9 | 10.4 | 6.2 | 30.2 | 45.2 | 14.2 | 4.2 |
| 14 | 27.4 | 34.7 | 35.7 | 1.8 | 0.5 | 22.5 | 23.0 | 48.6 | 4.7 | 1.1 | 4.0 | 15.5 | 68.6 | 9.5 | 2.4 | 5.4 | 12.8 | 50.4 | 23.2 | 8.3 | 2.9 | 9.8 | 52.5 | 26.1 | 8.7 |
| 15 | 0.4 | 1.4 | 40.1 | 30.5 | 27.6 | 3.1 | 11.9 | 51.7 | 15.6 | 17.7 | 4.3 | 19.0 | 40.6 | 5.6 | 0.6 | 3.3 | 18.5 | 51.9 | 16.1 | 10.2 | 8.7 | 31.3 | 54.3 | 3.9 | 1.7 |
| 16 | 0.2 | 2.8 | 41.6 | 28.4 | 26.9 | 7.8 | 17.3 | 43.7 | 14.7 | 16.5 | 12.0 | 35.6 | 49.7 | 2.6 | 0.2 | 4.9 | 20.2 | 44.2 | 18.3 | 12.4 | 11.3 | 28.8 | 48.2 | 8.1 | 3.6 |
| 17 | 23.7 | 33.7 | 35.7 | 4.2 | 2.6 | 22.8 | 37.6 | 32.7 | 4.3 | 2.6 | 7.8 | 28.6 | 57.9 | 4.7 | 1.0 | 4.8 | 15.3 | 44.3 | 26.4 | 9.2 | 11.0 | 31.0 | 42.0 | 13.5 | 2.6 |
| 18 | 0.4 | 8.4 | 62.2 | 12.3 | 16.7 | 6.9 | 23.1 | 50.9 | 6.6 | 12.5 | 12.0 | 36.8 | 50.4 | 0.5 | 0.3 | 19.3 | 48.3 | 25.3 | 3.1 | 4.1 | 24.6 | 42.0 | 30.8 | 1.3 | 1.3 |

In addition, Tables 10 and 11 show characteristics of each cluster interpreted and organized from Table 9. In case 1, many clusters can be interpreted in two theories agree or against. However, in case 2, an intermediate evaluation between agree and against can be inferred.

As described in this section, we conducted a comparison of the two cases for each method of handling the hidden intention responses. We considered that the approach of complementing the Non-declaration of intention responses is inappropriate for two reasons: 1. the cluster of Non-declaration of intention overall becomes very large; 2. It might engender misinterpretation because clusters with extreme tendencies to respond are classified.

Table 10 Characteristics of respective clusters (Case 1)

| Viewpoint | Cluster 1 | Cluster 2 | Cluster 3 | Cluster 4 | Cluster 5 |
|---------------------------------|-------------|-----------|-----------|---------------|---------------|
| Public support | Reduce | Reduce | Uncertain | Reduce | Reduce |
| Routes | Reduce | Reduce | Uncertain | Pros and Cons | Reduce |
| Number of services | Reduce | Reduce | Uncertain | Do not Reduce | Pros and Cons |
| Fare | Raise | Raise | Uncertain | Do not cut | Do not raise |
| Abolish | Agree | Uncertain | Uncertain | object | object |
| Public information, advertising | Unnecessary | Need | Need | Need | Need |
| Usability | Nothing | Uncertain | Uncertain | Uncertain | Existence |
| Pride | Nothing | Uncertain | Uncertain | Existence | Existence |
| Interest | Nothing | Uncertain | Uncertain | Existence | Uncertain |

Table 11 Characteristics of respective clusters (Case 2)

| Viewpoint | Cluster 1 | Cluster 2 | Cluster 3 | Cluster 4 | Cluster 5 |
|---------------------------------|---------------|-----------|--------------|---------------|---------------|
| Public support | Reduce | Reduce | Expand | Pros and Cons | Do not expand |
| Routes | Reduce | Reduce | Expand | Do not reduce | Do not expand |
| Number of services | Reduce | Reduce | Expand | Do not reduce | Uncertain |
| Fare | Pros and Cons | Raise | Do not raise | Pros and Cons | Do not Cut |
| Abolish | Agree | Uncertain | Object | Object | Object |
| Public information, advertising | Uncertain | Need | Need | Need | Need |
| Usability | Nothing | Uncertain | Existence | Uncertain | Existence |
| Pride | Uncertain | Uncertain | Existence | Existence | Existence |
| Interest | Nothing | Uncertain | Uncertain | Existence | Existence |

(3) Classification by the pattern of strength of intention

To classify the pattern of strength of intention and reveal the tendency of attitude for the responses, we aggregated and organized each response as five patterns of strength of intention (Table 12), and conducted a cluster analysis. The analysis was conducted for the sample excluding error response ($n=16,888$).

Table 12 Classification of responses by the pattern of strength of intention

| Pattern of strength of intention | Point |
|----------------------------------|--|
| Declaration of strong intention | Strongly agree: 2 Strongly object: -2 |
| Declaration of intention | Agree: 2 Object: -2 |
| Neither | Neither: 0 |
| <i>Do not know</i> | DK |
| Blank | Blank |

Figure 3 presents average frequencies related to the responses of the eight clusters that we adopted based on Table 12. Furthermore, Table 13 shows characteristics of the cluster and number of samples based on Figure 3.

The group organized around the responses of intention accounted for 80% of the total (clusters 1 and 2). These groups are considered to represent a normal response. In addition, the group that responded for many questionnaire items with blank or neither or *do not know* accounted for 15.8% of the total (clusters 6, 7 and 8). Furthermore, the group that blank and *do not know* appear together is only one sample in cluster 3. Therefore, we considered that these options are not distinguished with a meaning in the responses.

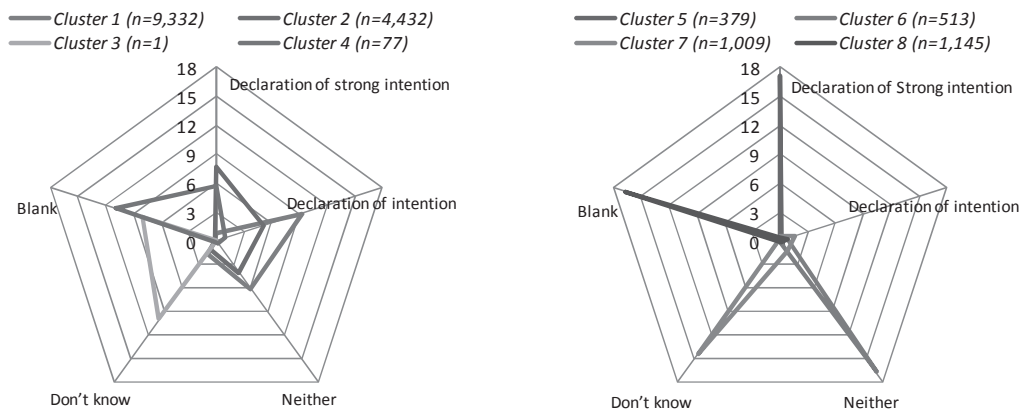


Figure 3 Average frequencies for responses by clusters based on the pattern of strength of intention.

Table 13 Characteristics of clusters and numbers of samples

| Cluster | Characteristics | Number of samples |
|---------|---|-------------------|
| 1 | Declaration of intention is a majority | 9,332 |
| 2 | Declaration of strong intention is a majority | 4,432 |
| 3 | Use of blank and <i>Do not know</i> | 1 |
| 4 | Most are blanks, and declarations of strong intention are few | 77 |
| 5 | Approximately only in declaration of strong intention | 379 |
| 6 | Approximately only in Neither | 513 |
| 7 | Approximately only in <i>Do not know</i> | 1,009 |
| 8 | Approximately only in Blank | 1,145 |

5. Conclusion

This study clarified resident awareness related to community buses for Izumi-shi, Osaka. Results of analyses, in addition to resident responses, clarified the following points.

1. To all questionnaire items, responses such as blank or *do not know* constituted around 20%. Particularly, around 40% of respondents replied neither about the questionnaire item such as own use or interest or pride.
2. The principal components are inferred as follows:
Reduction of public support, lack of interest in buses, support from fare hikes, and efficiency of business
3. Regarding handling of non-declaration of intention responses, we compared them using two techniques of supplement and deletion, but no difference was found principal component results.
4. However, regarding classification and interpretation, because it is difficult to obtain an appropriate result, supplementary treatment of non-declaration of intention responses is unsuitable as a technique.
5. Regarding the strength of the intention in the responses, the group of the responses mainly on the declaration of intention were 58.8% of all responses. In addition, the group of the responses mainly on declaration of strong intention constituted 26.2% of the whole. The group of responses of non-declaration of intention overall constituted 16%. Respondents using neither and *do not know* and blank properly were almost nonexistent.

References

- 1) Y. Kurashima, R. Kondo: Research on the image of shuttle bus, focused on frequency of use, *Proceedings of Infrastructure Planning*, Vol. 44 (CD-ROM), 2011(in Japanese)
- 2) Izumi city in Osaka: Report of resident questionnaires about public transport for residents of Izumi city in Osaka (prompt report),
<http://www.city.osaka-izumi.lg.jp/ikkrwebBrowse/material/files/group/44/01kekkahonpen.pdf>,2011(in Japanese)

Liquid / Liquid Near Interface Analysis by Micro-XRF Using Needle-Type Collimators

Yoshihiko NISHIDA and Kouichi TSUJI

(Received October 14, 2012)

Synopsis

We have developed a method of micro XRF using injection needle-type collimators. Two injection needle-type collimators were attached to an x-ray tube and the detector. The beam size of the primary x-rays was evaluated to be 740 μm , depending on the inner diameter of the first collimator for excitation. These injection needle-type collimators were inserted into solution samples. The end of each collimator was covered with an x-ray transparent plastic sheet. The x-ray fluorescence was detected by an energy-dispersive detector through the second collimator. The positions of the two injection needle-type collimators were fixed, while the glass container for sample solution was moved in x-y-z directions. Therefore, it was possible to perform in-situ XRF depth analysis and 3D-XRF analysis in the solution. This technique was applied to liquid-liquid near surface analysis. The distributions of Cu in HCl solution and Fe in MIBK solution were successfully obtained near the liquid-liquid interface.

KEYWORDS: Micro XRF, Elemental analysis, Extraction, Liquid/liquid interface, Depth analysis, 3D-XRF

1. Introduction

X-ray fluorescence spectrometry (XRF) has an advantage in that it can be operated at atmospheric pressure without complicated sample preparation of many types of samples including solid and liquid samples.¹⁾ In XRF analysis of liquid samples, the primary x-ray beam usually irradiates the surface of the sample solution (or the back of the solution thorough an x-ray transparent window) and XRF signals are detected at the outside of the sample solution, as shown in Fig. 1 (a). This usual method has a drawback in that the analytical depth in the liquid sample is considerably short because of strong absorption of the x-rays in the liquid.

Solid-liquid and liquid-liquid near interfaces are important sites where chemical reactions such as corrosion, metal plating, and solvent extraction occur. Therefore, an analytical method for in-situ monitoring of liquid samples has been required. The author's research group proposed in-situ XRF analysis of solutions using a monolithic glass collimator for the excitation and detection of x-rays.²⁾ The primary x-rays were introduced the glass tube (diameter: about 10 mm). The end of the glass tube was covered with an x-ray transparent plastic sheet. This glass tube was inserted into the sample solution, and the primary x-rays directly irradiated the solution through the plastic sheet. The x-ray fluorescence produced in the solution was detected through another glass tube by an energy-dispersive x-ray detector. To accomplish micro x-ray analysis of the solution, we proposed an XRF spectrometer using injection-needle type collimators as shown in Fig. 1(b).^{3,4)} In a previous study, injection needle-type collimators were inserted in an oyster (soft sample). Quantitative XRF analysis of Zn at a specific position (any x-y position and any depth) was performed.⁴⁾ However, analysis was difficult because the positions of the two needles changed in the solid material. In this paper, the technique was applied to the XRF analysis of solutions. We can freely position the injection needle-type collimators in the solution for XRF analysis of a specific region in the solution.

2. Experimental

Figure 1 (b) is a schematic diagram of the XRF spectrometry using injection needle-type collimators. In this work, the needle-type collimators were made of titanium tube (purity: 99.5%, outside diameter: 1.58 mm, inside diameter: 1.38 mm), and attached to an x-ray tube (Mo target, 40 kV, 20 mA) and an energy-dispersive x-ray detector (AMPTEK Inc., USA; XR-100CR, sensitive area: 7 mm², energy resolution: 187 eV at 5.9

keV). An x-ray tube and an x-ray detector were placed at a 90° angle between the primary x-ray beam and the direction of detection as shown in Fig. 1 (b). Both collimators were 3.5 cm long and the angle of the top of the needles was 45°. The tops of the collimators were covered with polyimide film (thickness: 7.5 μm) to prevent the solution from being introduced into the collimator.

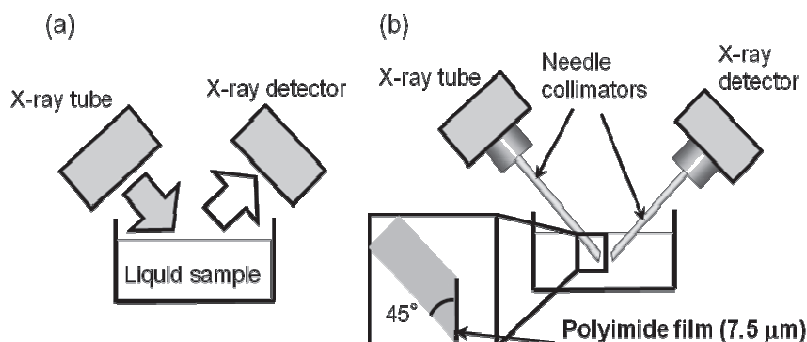


Fig. 1 Schematic diagrams of conventional XRF (a) and micro-XRF using injection needle-type collimators (b).

3. Results and Discussion

3.1. X-ray beam size

The beam size of the primary x-ray beam was evaluated by a wire scanning method. A Cu wire (diameter: 30 μm) was placed near the top of the collimator. The intensities of the x-ray fluorescence were recorded as a function of wire position. Figure 2 shows the intensity profile of Cu Kα as a function of scanned distance. The FWHM value of this profile was 1046 μm. As shown in the inset of Fig. 2, the actual beam size should be $FWHM / \sqrt{2}$. After taking the wire size into account, the corrected beam size was 740 μm.

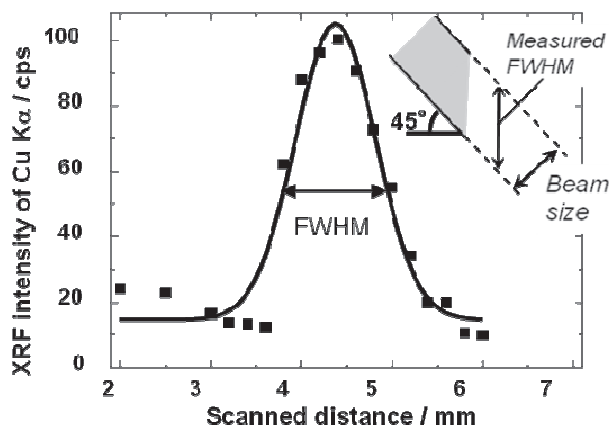


Fig. 2 Cu Kα intensity profile as a function of scanned distance.

3.2. Optimization of analytical region

The distance between the two needles was optimized by monitoring the intensity of the x-ray fluorescence originating from the liquid sample. In this paper, the distance between the needles is termed the “needle distance”. Fig. 3 (a) shows the relationship between Ni Kα intensity (7.47 keV) and the needle distance for Ni(NO₃)₂ solution. The measurement time was 300 s per point.

When the collimator touched the other collimator, we defined the needle distance as 0 mm. As shown in Fig. 2, the x-ray fluorescence of Ni Kα was detected with the highest efficiency at a needle distance of 600 μm.

Other solutions of different elements were also investigated. Fig. 3 (b) shows optimized needle distance as a function of the energy of x-ray fluorescence. When the energy of fluorescence x-ray was 8.6 keV or more, the optimized needle distance became saturated at about 1 mm. This result indicates that the needle distance should be adjusted to an optimum distance.

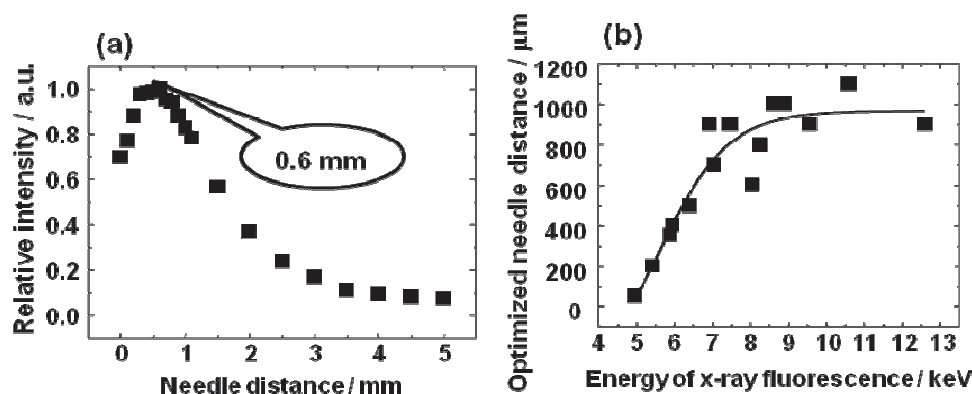


Fig. 3 Relationship between needle distance and relative intensity of Ni K α (a); effective needle distance as a function of x-ray fluorescence energy (b).

3.3. Detection limits

For quantitative analysis of a solution sample by micro-XRF, the relationship between Zn K α intensity and the concentration of Zn was investigated at a measurement time of 1000 s and a needle distance of 1000 μm , where Zn K α (8.6 keV) was detected at the highest intensity. A linear relationship (correlation coefficient: 0.999) is shown in Fig. 4. The detection limit of Zn was evaluated to be 2.0 ppm. Similarly, the detection limits of Fe, Cu and Pb were evaluated to be 6.1 ppm, 3.7 ppm, and 6.5 ppm, respectively. The Ti injection needles contain a small amount of Fe as impurity. Because of the x-ray fluorescence originating from the needle-type collimators, the detection limit of Fe was higher than that of the other elements. The detection limit of Pb was high, because a Pb L α (10.6 keV) peak was observed on a large continuous x-ray spectrum.

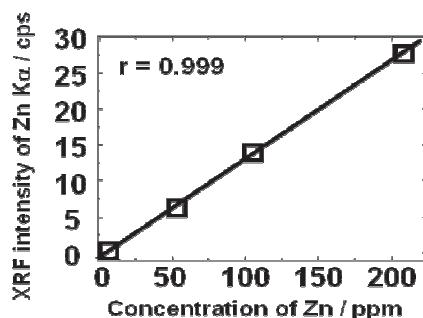


Fig. 4 Calibration curve of Zn K α .

3.4. Liquid-liquid near interface analysis

Finally, in-situ XRF analysis near the liquid-liquid interface was demonstrated. A glass container of solution sample was translated by using a Z-axis stage. Therefore, both needle-type collimators could be introduced into the solution at a specific depth.

A HCl solution (6 M) including Fe (1000 ppm) and Cu (1000 ppm) was prepared. Methyl-isobutyl-ketone (MIBK) was used to extract the Fe from the HCl solution. After the extraction, a depth analysis was performed for the two-phase solution (MIBK and HCl) for a measuring time of 100 s, at a needle distance of 200 μm and a step size of 200 μm .

Figure 5 (a) shows the normalized intensity profile of Cu K α and Fe K α as a function of the scanned distance. When the analytical area was in aqueous HCl phase, only the Fe K α and K β peaks were observed,

as shown in Fig. 5 (b). Figs. 5 (c) and (d) show XRF spectra obtained at the HCL-MIBK interface and the MIBK phase, respectively. As shown in Fig. 5 (a), in-situ micro-XRF method confirmed that the Fe that originally existed in the HCl solution was extracted into the MIBK solution.

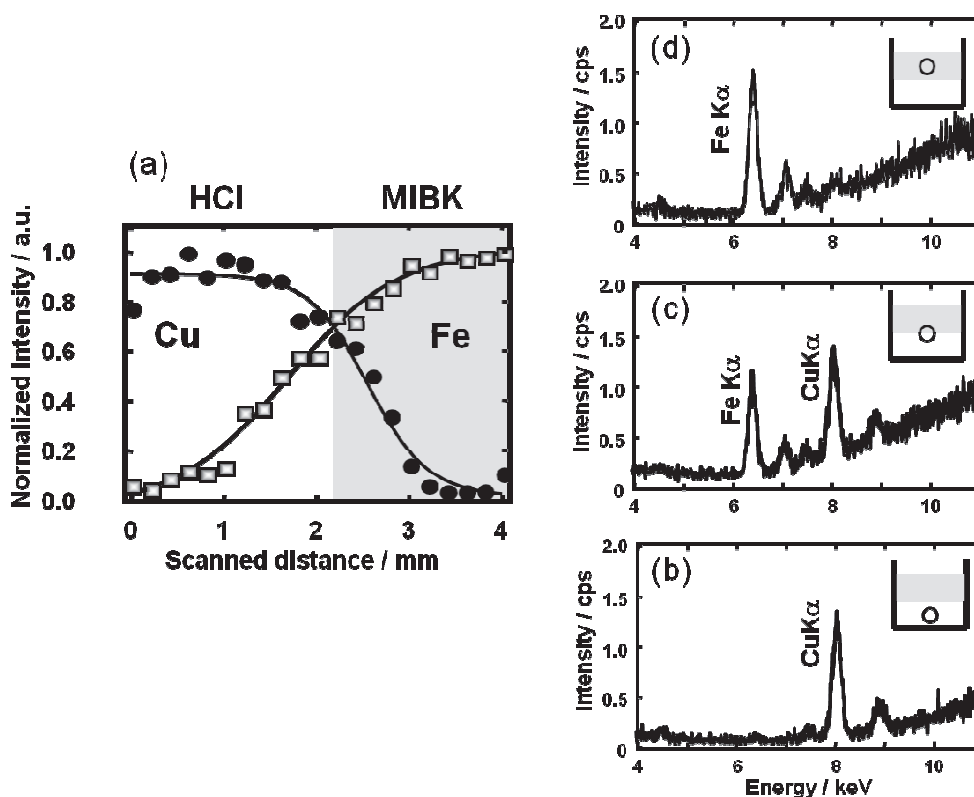


Fig. 5 Normalized intensity profiles of Cu K α and Fe K α as functions of scanned distance (a); XRF spectra measured at HCl solution phase (b), liquid-liquid interface (c), and MIBK phase (d).

4. Conclusions

A micro-XRF method using injection needle-type collimators based on titanium was proposed. The needles were attached to the x-ray tube and to the detector side. It was found that the optimum needle distance depended on the energy of the x-ray fluorescence. The detection limits of Fe, Cu, Zn, and Pb were evaluated to be 6.1 ppm, 3.7 ppm, 6.5 ppm and 2.0 ppm, respectively. Elemental depth analysis near the liquid-liquid interface was performed after the Fe was extracted from the HCl to MIBK phase. XRF spectra were successfully measured at different depths.

5. References

- 1) R. Van Grieken and A. A. Markowicz, *Handbook of X-Ray Spectrometry*, Marcel Dekker Inc., New York (2002).
- 2) K. Tsutsumimoto and K. Tsuji, *BUNSEKI KAGAKU*, **56**, 499 (2007).
- 3) A. Matsuda and K. Tsuji, *BUNSEKI KAGAKU*, **55**, 681 (2006).
- 4) K. Tsuji, A. Matsuda, K. Nakano and A. Okhrimovskyy, *Spectrochim. Acta B*, **61**, 460 (2006).

Abstracts of Papers

Published in Other Journals

Mechanical Engineering

CFD Analysis inside a CO₂ Rotary Compressor Shell to Improve Oil Separation and Reduce the Shell Size

Tetsuhide YOKOYAMA, Keisuke SHINGU, Shin SEKIYA, Hideaki MAEYAMA and Nobuya NISHIMURA

Proc. of the International Compressor Engineering Conference at Purdue, pp. 1230 (10 pages), Purdue, USA, (2012.7) (on CD-ROM) (2012)

A CO₂ rotary compressor uses refrigeration oil to lubricate and cool sliding parts and to seal the cylinder. It is difficult to separate the oil inside the shell at high pressure from CO₂ gas, whose difference in density from the oil is small. It remains an issue to retain high efficiency with the same shell size as a present hydro fluorocarbon (HFC) compressor. We explored an improvement in the oil separation by use of CFD analysis and identified two effective measures. One measure is to flatten a lower balance weight of the rotor to prevent the oil mist from moving up through the motor flow paths. Another measure is to set up a rotating disc over a protruding balance weight at the top of the rotor to increase the pressure in the upper space and allow the oil over the stator to return to the lower space by gravity. Experiments with an actual compressor verify that oil separation is improved to the target value.

In-situ Color Measurement and Photo-dome Photographing System for Food Quality Analysis

Hiroyuki IYOTA and Hideki SAKAI

Proc. of the International Congress on Food Engineering and Technology (IFET2012), 5A-1 (6 pages), Bangkok, Thailand (2012.3) (on CD-ROM)(2012)

We introduce two colorimetric methods for visual evaluation of foods. One is an in-situ color measurement during food processing using a spectrometer and a glass fiber probe, and the other is a color image photographing method using a spherical "photo-dome" in conjunction with image processing and quality evaluation analysis methods. A crumb of sliced white bread was used as the sample foodstuff to demonstrate the performance of the two methods. The baking process and the quality of the baked product were investigated. Producing delicious-looking food / delicious appearance is one of the qualities required incoming cooking equipments. The two color measurement methods introduced are very useful for evaluating cooking equipments from the visual aspects of foods.

Effect of Time-Dependent Humidity Profiles on Change in Food Color during Heating with Steam Convection Oven

Hiroyuki IYOTA, Yusuke MAMIYA, Tomohiro KAYANO, Junko YAMAGATA, Hideki SAKAI and Kuniko SUGIYAMA

Proc. of International Congress on Food Engineering and Technology (IFET2012), PP-12 (7 pages), Bangkok, Thailand (2012.3) (on CD-ROM) (2012)

Steam convection ovens are widely used in domestic and commercial applications. However, the effect of changes in humidity on food quality during heating is still not clear. This study was aimed at understanding this effect and investigating the optimization of oven operation. The steam mole fraction in the oven chamber and the color of the food surface were measured continuously under three steam supply operation modes. A crumb of white bread, pates of chicken breast and round of beef were used as samples. The food color change was found to be affected by the steam mole fraction (dew point temperature) depending on the operation mode, as well as by thermal properties, moisture content, and sensitivity to moisture and temperature, e.g., through protein denaturation and the Maillard reaction. The study results and measurement techniques can contribute to the technological advancement of steam utilization and to the optimization of oven operation.

Development of High-Temperature Wide-Range Humidity Sensor by Wetted Material Temperature Measurement (Improvement of Measurement Accuracy by Considering the Effect of Supplied Water)

Takashi KITAHARA, Hiroyuki IYOTA and Tamotsu INOUE

Trans. Jpn. Soc. Mech. Eng., Ser. B, Vol. 78, pp.686-696 (2012) (in Japanese)

A high-temperature wide-range humidity sensor has been developed using wetted material temperature measurement. A porous ceramic is used as a sensing element; it has a small tube for supplying water to maintain a wetted surface. However, the water supplied to the elements can affect the surface temperature. In

this study, we experimentally investigate the accuracy of the developed sensor and its contributing factors—convective heat transfer, evaporation, radiant heat, and the water supplied to the wetted material—under the conditions of a gas flow temperature of 200 °C, gas flow velocity of 3 or 5 m/s, flow rate of supplied water of 0.01–0.05 g/s, and steam mole fraction of 0.03–1.00. Further, we calculate the heat flux and the surface temperature using a one-dimensional heat transfer model to clarify the effects of the each of the abovementioned factors. Consequently, we conclude that the supplied water strongly affects the accuracy of the developed sensor. We also improve the measurement error of the steam mole fraction from 0.07 to 0.03 by the controlling the flow rate of the supplied water.

Simplified Measurement Method for Steam Mole Fractions Based on Temperature Measurement with Wet Spherical Material (Using Adiabatic Saturation Line Applied to High Temperature and High Humidity)

Hiroyuki IYOTA, Shogo ISSHIKI, Tamotsu INOUE and Junko YAMAGATA
Trans. Jpn. Soc. Mech. Eng., Ser. B, Vol. 78, pp.1267-1278 (2012) (in Japanese)

Superheated steam-containing hot air under atmospheric pressure has been used as a heating media for thermal processing such as food processing, cooking, sterilization, drying, and waste treatment. For these types of thermal processing, the steam mole fraction of the media sometimes strongly influences product quality. Hence, a simple method is required for measuring the steam mole fraction under a high temperature of more than 250°C. In this report, we propose an equation to calculate the steam mole fraction using the adiabatic saturation temperature for a wide range of temperatures and humidity values, i.e., from room temperature to 350°C and from room air to pure superheated steam. We also present a psychrometric chart with the steam mole fraction on the y-axis, which can indicate the presence of dry air and pure superheated steam. The values calculated by the proposed equation were in good agreement with values obtained in previous literature under comparable conditions. For developing a simple and convenient measurement method, a wet spherical gauze/brick is used for measuring the wet-bulb temperature. Its accuracy and applicability are investigated experimentally. The results show that this method can measure the steam mole fraction with an accuracy of less than 0.09 in the temperature range of 160–280°C. The causes of error and the methods for intending utilization are also investigated.

Development of the Paddy Seed Sterilization Device using Mixture of Superheated Steam and Hot Air Takahiro NODA, Yasuyuki HIDAKA, Mio YOKOE, Hiroyuki IYOTA, Akihiko OCHI, Toru NAKAMURA and Waichiro MATSUDA

IFT12 Book of Abstracts-Digital, ID:042-01, Las Vegas, USA (2012.6) (on CD-ROM)(2012)

For the safety of food supply, the reduction of pesticides use is suggested in agricultural production stage. Rice is the most important staple food for a large part of the world, and many agrochemicals are used for sterilization in the production stage. The paddy seed is especially an important target of sterilization, as it carries many pests. In this study, we tried to sterilize seed-borne diseases by using the mixture of the superheated steam and hot air to develop chemical-free sterilization method of paddy seed.

We developed the sterilization test device in which the paddy was conveyed by the vibration feeder made from the perforated board and the paddy was sterilized for 2 seconds for the heating air flowing through the hole of the board. The temperature of the heating air was set at 200 degrees, and the molar fraction of superheated steam was controlled at 0.67.

In order to confirm the sterilization effect, 100 grams of Blast-diseased paddies were treated by the test device. The paddies were then immediately cooled by ambient air to keep the seed germination and dry the condensed water. 50 grains of selected paddies were put in the agar media for 2 days in the incubator set at 25 degrees. We then counted the number of conidium germination of Blast and evaluated the sterilization effect. The healthy paddies were also treated by the test device in the same manner, and measured seed germination rate. The conidium germination rate of Blast was 0.0 %, whereas the rate without treatment was 31.0 %. The seed germination rate was 98 % and no significant difference ($p < 1$ %) between the paddy with and without treatment was observed. These results showed the sterilization method has potential to alternate agrochemicals and contribute to the food safety.

Development of High-Temperature Wide-Range Humidity Sensor by Wetted Material Temperature Measurement (Application of Porous Ceramic into Sensing Element)

Tamotsu INOUE, Hiroyuki IYOTA and Shogo ISSHIKI
Trans. Jpn. Soc. Mech. Eng., Ser. B, Vol. 78, pp.1451-1461 (2012) (in Japanese)

We applied the theory of a psychrometer to develop a humidity monitoring system by using cylindrical porous ceramic as a sensing element. This system contains a section for supplying/discharging water. Several types of porous ceramics were made and the effects of porosities and pore size distributions on capillary water transfer were investigated. Also, we tested the performance of this system in terms of its response time and measurement accuracy. The capillary water transfer was higher in the conditions that porosity was larger and pore size distribution was wider. In addition, at a gas flow rate of 1 m/s and a gas temperature less than 310 °C, the error of the steam mole fraction was observed to be less than 10 %. Further, the system had a 90 % response time of less than 60 s and this time was shorter as humidity increased at a gas temperature of 200 °C, a gas flow of 1 m/s, a flow rate of supplied water of 0.01 g/s and a water temperature of 25 °C when a sensing element diameter was 9 mm.

Development of Browning Scale of Baked Foods Based on Color Measurement

Hideki SAKAI and Hiroyuki IYOTA

Conference Proceedings of AIC 2012 Interim Meeting of the International Colour Association (AIC), pp.258 - 261, Taipei, Taiwan (2012. 9)(2012)

We measured the surface colors of plain cookies, sliced breads, and grilled fish (pacific saury) at various stages of baking and made their color charts (browning scales) based on color measurements. A large spherical dome with a diameter of 600 mm, whose inner surface was painted white, was used to illuminate large food samples uniformly by D65 fluorescent lamps. We placed food samples at various stages of baking in the middle of the dome and recorded their colors by a digital camera. Then, we derived color-corrected images using the X-Rite ColorChecker as the color standard. The baked color of each food was found to be dominated by the lightness, L^* ; color changes in a^* and b^* of each food during baking were well described by the regression equations with L^* . Using these regression equations, browning scales of plain cookies, sliced breads and grilled fish have been developed.

Theoretical Analysis of Several Problems Related to Solid-Liquid Wetting Phenomena

Kenji KATOH and Takahiro ITO (Nagoya University)

Science of Machine, Vol. 64, pp. 378-388 (2012) (in Japanese)

Several phenomena related to wetting behavior are investigated theoretically. The problems are generally classified into two categories, i.e., one is quasi-static wetting behavior and the other is related to dynamic wetting in which the contact angle is dependent on the three-phase contact line velocity. In the former, we treat here the dropping of liquid in a tilted thin pipe having a closed upper end and the detachment from a pendant drop attached to a curved surface. In those problems, the macroscopic energy equilibrium condition is theoretically estimated with including the work due to wetting behavior. The critical inclination of pipe and the separated volume obtained from the instability condition agreed well with those measured experimentally. In the latter, the velocity dependence of contact angle is investigated with the help of molecular dynamics (MD) technique. The flow field near the contact line is analyzed by insisting slip condition at the wall. The MD results show that the dynamic contact angle is strongly dependent on the force balance on the wall, in which slip coefficient is included in the viscous drag and the wetting force due to contact angle difference between static and dynamic cases are taken into consideration.

Heat Transfer Enhancement and Pressure Loss in a Channel with a Vortex Generator (Effect of Prandtl number)

Kenji KATOH, Tatsuro WAKIMOTO and Takashi NISHIMURA

Trans. of Jpn. Soc. Mech. Eng., Ser. B, Vol. 78, No. 2012-JBR-0310 (2012) (in Japanese)

The efficiency index η , (i.e., the ratio between heat transfer enhancement and drag increase from a smooth channel), is discussed in a channel with a delta wing-type vortex generator (VG) installed on the wall in laminar and turbulent flow. In this report, the effect of Prandtl number Pr on η is mainly discussed by use of the equation obtained in the preceding report to estimate various effects on the heat transfer enhancement. From the results of direct numerical simulation, η decreases slightly in the turbulent flow with Pr , while it increases noticeably in the laminar flow. In the laminar flow, since there is no background turbulence in the smooth channel, the fluctuation generated by VG directly enhances the heat transfer, which is greater at high Pr where the thermal diffusion effect is weakened. In addition, the increase of convective heat transfer near the wall has an important effect on the good efficiency. In the turbulent flow, on the other hand, the efficiency index slightly decreases with Pr since the turbulence generated by VG is not strongly dependent on the Prandtl number. The influence of the notched hole beneath the wing is discussed from the numerical results.

The Influence of Pressure Gradient-Wall Normal Velocity Correlation on Turbulent Prandtl Number

Kenji KATOH, Tatsuro WAKIMOTO and Naoki NISHIOKA

Trans. of Jpn. Soc. Mech. Eng., Ser. B, Vol. 78, No. 2012-JBR-0248 (2012) (in Japanese)

The similarity between turbulent heat transfer and Reynolds stress is investigated using the equations written in Lagrange description. The correlation between pressure gradient fluctuation in the flow direction and wall-normal velocity [term (B)] depresses the Reynolds stress, which makes the turbulent Prandtl number Prt less than unity. Based on the trajectories of fluid particles, an algebraic equation was theoretically derived to correlate the term (B) to Prt . Using the database of the trajectories calculated by DNS, the change of Prt with regard to (B) was actually estimated from the equation. The slight decrease of (B) causes the dramatic reduction of Prt in the log-law region, while the change of Prt in the near-wall region is hardly recognized. This is caused by the fact that the Reynolds stress or turbulent heat transfer in the log-law region are influenced by the fluid particles coming from further positions compared with the near-wall region.

Spontaneous Dropping of Liquid Column in a Tilted Capillary Pipe with an Upper Lid

Kenji KATOH and Tatsuro WAKIMOTO

J. of JSEM, Vol. 12 (Special Issue), pp. 105-1110 (2012)

A theoretical and experimental study is conducted to discuss the spontaneous dropping of liquid in a vertical capillary pipe with a lid at the top end. The system energy was calculated when the pipe is inclined to the horizontal direction. The pendant liquid surface formed at the pipe end becomes unstable if the infinitesimal energy change is negative when the three-phase contact line shifts upward on the pipe inner wall. The critical inclination of the pipe is calculated theoretically and the results agree with those obtained experimentally for various kinds of test liquids.

Instability of a Planar Liquid Sheet Formed with Surfactant Aqueous Solution

Tatsuro WAKIMOTO, Ryousuke FUJII and Kenji KATOH

Jpn. J. of Multiphase Flow, Vol. 25, No. 5, pp. 511-518 (2012) (in Japanese)

Growth characteristics of instability waves of a planar liquid sheet formed with surfactant solution has been clarified. It is widely reported that a liquid sheet jet oscillates in sinuous shape because of Kelvin-Helmholtz instability and their growth rate depends on surface tension. If the liquid is surfactant solution, the growth characteristic depends on time-dependent surface tension referred to as dynamic surface tension because adsorption of surfactant molecules to newly formed surface requires certain time. In this study, the wave growth affected by the dynamic surface tension has been investigated as following. At first, the relationship between the growth rate of the wave and time-invariant surface tension was determined using ethanol aqueous solutions with different concentrations. Secondly, the dynamic surface tension of the surfactant solution was measured, and surface tension varying with the distance from the nozzle was estimated. Thirdly, spatially varying amplitude of the wave is calculated from the results of above two steps. Finally, the calculated wave amplitude was compared with measured amplitude for surfactant solution. The good agreement between calculated amplitude and experimental one proved that growth characteristic for surfactant solution depends on dynamic surface tension.

A Study on Perforation of a Liquid Sheet Caused by Thermocapillary Effect

Tatsuro WAKIMOTO, Masahiro KOMATSU and Kenji KATOH

Trans. of Jpn. Soc. Mech. Eng., Ser. B, Vol. 78, No. 789, pp. 1083-1094 (2012) (in Japanese)

The perforation of a thin liquid sheet by thermocapillary effect has been investigated. In a radial liquid sheet, which is produced by release of a liquid film spreading on a disk into the air, a laminar-turbulent transition occurs just outside the disk edge. The coherent turbulent structure after the transition forms the extremely thin liquid sheet locally and perforates it. In addition, the perforation is promoted by the impingement of a hot air flow on the thin liquid sheet. This perforation promotion requires specific condition of liquid flow velocity and airflow temperature. This study proposed the theoretical model of thermocapillary induced perforation of the thin liquid sheet and predicted the specific condition for the thermal perforation promotion in the radial liquid sheet. This model representing time diminishing sheet thickness is derived from a momentum balance between inertial force, Marangoni force and Laplace pressure. A simplified model gives the simple algebraic equation expressing the time required to the perforation. The validity of the theory is verified by comparing the theoretical perforation time with that calculated from a numerical simulation based on CIP method. The specific condition for the perforation promotion, which is estimated from the theoretical

perforation time, agrees well with experimentally observed one. This agreement demonstrated that the perforation promotion is caused by thermocapillary effect.

Suppression of Disintegration of Fan Liquid Sheet by Surfactant

Tatsuro WAKIMOTO and Kenji KATOH

J. of JSEM, Vol. 12 (Special Issue), pp. 111-115 (2012)

Disintegration process of aqueous surfactant solutions injected from a fan spray nozzle has been clarified. The thin sheet of the surfactant solution, as represented by soap film, is stable by surface chemical effect and breaks up hard. In this study, this effect on the atomization of the fan liquid sheet has been investigated. Surface chemical stability was evaluated by Ross-Miles method and two types of the test liquids, which had same hydrodynamic physical properties and different surface chemical stability, were prepared. Measured break-up length, which was defined as the distance from the nozzle tip to the end of the liquid sheet, for the two test liquids indicated that the surface chemical stability obviously suppress the disintegration of the liquid sheet.

Effect of Air Injection on Drag-Reducing Surfactant Solution in an Upward Vertical Pipe Flow

Koichi ARAGA, Syuhei KOMIYAMA, Tatsuro WAKIMOTO and Kenji KATOH

J. of JSEM, Vol. 12, No. 3, pp. 105-111 (2012)

The values of heat-transfer coefficients decrease in a drag-reducing surfactant solution flow. Therefore, it is necessary to develop an effective method for enhancing the heat transfer of a surfactant solution flow. The objective of this study is to examine the heat transfer enhancement effect when microbubbles are injected into a drag-reducing surfactant solution flow. Specifically, the relationship between microbubble size and the heat transfer enhancement of a surfactant solution flow was investigated experimentally. Microbubbles were generated using a porous metal pipe placed in a test pipe. Microbubbles having different sizes were generated by using three types of porous metal pipes. The flow patterns observed in air microbubble-surfactant solution two-phase flows were fine bubbly; these patterns were independent of microbubble size. The heat transfer enhancement effect depends on the air-surfactant solution flow ratio or microbubble size. An increase in the air-surfactant solution flow ratio or decrease in the microbubble size leads to a greater heat transfer enhancement effect.

Nonlinear Vibration and Numerical Simulation of a Cylindrical Liquid Storage Tank (Nonlinear Behavior of Oval-Type Vibration)

Akira MAEKAWA and Katsuhisa FUJITA

Trans. Jpn. Soc. Mech. Eng., Ser. C, Vol. 77, No. 783, pp. 4034-4042 (2011) (in Japanese)

This Paper describes a nonlinear behavior of oval-type vibration in a cylindrical liquid storage tank which is high order vibration mode in the circumferential direction of the wall (axial half wave number $m \geq 1$ and circumferential wave number $n \geq 2$). When the vibration experiment of a cylindrical liquid storage tank was conducted by exciting its base, a nonlinear behavior of oval-type vibration occurred, especially at large excitation. The nonlinear behavior of oval-type vibration was dynamically simulated by nonlinear explicit finite element analysis method considering fluid-structure interaction as well as large deformation. It can be concluded the proposed numerical analysis method can simulate the nonlinear behavior of oval-type vibration accurately.

Motion and Vibration Analysis for Multi-Vehicles of a Roller Coaster on the 3D Trajectory

Katsuhisa FUJITA, Chihiro NAKAGAWA and Hiroaki TOSHIMITSU

Trans. Jpn. Soc. Mech. Eng., Ser. C, Vol. 77, No. 784, pp. 4543-4554 (2011) (in Japanese)

The motion and vibration for multi-vehicles of a roller coaster which move on the complicated three-dimensional trajectories are investigated. A roller coaster is treated with here as a concrete example of moving body. By using differential algebraic equations (DAE), the simulation method for moving bodies on 3D trajectory is proposed in this paper. In the previous papers, the simulation method using s-u-z coordinate for a single vehicle has been shown. In this paper, the analysis method which uses the global coordinate x_g - y_g - z_g is shown. In addition, the simulation method for multi-vehicles of a roller coaster is proposed. In order to solve the instability of the simulation analysis, the stabilization method proposed by Baumgarte is adopted. When all of connecting points are taken into consideration as constraint conditions, it is found to be too severe, and some play is necessary at connecting points for practical applications to an actual roller coaster. Lastly, the validity of the proposed simulation method by comparing with the experiment which has been reported in previous paper is examined.

Influence of Fluid Viscosity and Structural Specifications on Stability in the Vicinity of Critical Velocity of an Elastic Beam Subjected to Confined Axial Flow

Katsuhisa FUJITA and Ayumi OHKUMA

JSME Journal of System Design and Dynamics, Vol. 5, No. 8, pp. 1593-1604 (2011)

Evaluation methodologies for the flow-induced vibration of an elastic beam subjected to an axial flow confined in a narrow passage are reported. In this paper, by using the analytical method already proposed by one of authors, a parameter study is performed on the dynamic stability of an elastic beam subjected to axial flow confined a narrow passage. The effects of support conditions of structures, structural damping, and fluid characteristics on the dynamic stability are clarified. Especially, paying attention on the vicinity of critical velocity, the effects of stabilization or destabilization on flutter and divergence are investigated by changing fluid viscosity and structural damping.

A Consideration on Nonconservative Elastic Stability of a Beam Subjected to Axial Force Considered to be Fluid Force

Katsuhisa FUJITA and Akihide GOTOU

Trans. Jpn. Soc. Mech. Eng., Ser.C, Vol.78, No.789, pp. 1565-1574 (2012) (in Japanese)

The dynamic stability problem of machines and structures is one of the important subjects for a long time. Recently, they are considered to be relatively flexible for loads as they become large-sized and light-weighted. By the way, in the conventional dynamic stability analysis, many problems of the structural analysis have been dealt with as a conservative system. However, in the problems which are acted by fluid forces such as air and water in space structures and marine structures so on, the dynamics of structures are affected by the deflection of the structure. That is, the treatment of a nonconservative system such as a follower force becomes important. In this paper, the stability of non-conservative system of a beam is investigated when the fluid force acting on a cantilever subjected to the axial flow is considered to be an axial force. The fundamental study is performed by using the discrete model of 2 degree of freedom systems. Moreover, this is expanded to the continuous system of a cantilever. And, the physical consistency between a discrete model and a continuous one and the effect of damping are discussed.

Basic Study on Active Vibration Control Methods of Axisymmetric Elastic Beam Subjected to the Annular Flow

Atsuhiko SHINTANI, Shoji TAKADA, Tomohiro ITO and Katsuhisa FUJITA

Trans. Jpn. Soc. Mech. Eng., Ser.C, Vol.78, No.785, pp.1-11 (2012) (in Japanese)

Flow-induced vibration occurs in the structures subjected to annular beam in the narrow passage. Once the vibration occurs, the vibration becomes larger. In this paper, active vibration control of the axisymmetric elastic beam subjected to annular flow is investigated. Fluid-structure coupled equations based on the Euler-Bernoulli type partial differential equation and Navier-Stokes equation are derived including control terms. In this paper, two kinds of control methods using piezoelectric actuator and air pressured actuator are proposed. Applying the optimal control law to the coupled system, the unstable behavior is stabilized. Simulation studies are performed to investigate the efficiency of the proposed control methods and the effects of the actuator position on control performance.

A Consideration on Nonconservative Elastic Stability of a Beam Subjected to Axial Force Considered to be Fluid Force

Katsuhisa FUJITA and Akihide GOTOU

Proceedings of the 10th International Conference on the Flow-Induced Vibration (& Flow-Induced Noise), Dublin, Ireland, 3-6 July 2012, Flow-Induced Vibration Edited by Meskell & Bennett, ISBN 978-0-9548583-4-6, pp.375-382 (2012)

The dynamic stability problem of machines and structures is one of the important subjects for a long time. By the way, in the conventional dynamic stability analysis, many problems of the structural analysis have been dealt with as a conservative system. However, as it is thought that some problems may be affected by the deflections of a structure, the treatment of a nonconservative system such as a follower force becomes important. In this paper, the stability of nonconservative system of a beam is investigated when the fluid force acting on a beam subjected to the axial flow is considered to be an axial force. The fundamental study is performed by using the discrete model of 2 degree of freedom systems. Moreover, this is expanded to the continuous models of a cantilever, a simply supported beam and a free-free beam. And, the physical consistency between a discrete model and a continuous one and the effect of damping are discussed.

Dynamic Stability of an Elastic Beam Subjected to Follower Forces

Katsuhisa FUJITA and Akihide GOTOU

Proceedings of ASME Pressure Vessels and Piping Division Conference, Toronto, Ontario, Canada, PVP2012-78278 in CD-ROM (2012)

The stability of nonconservative system of a beam is investigated when an elastic beam is subjected to follower forces. The mathematical formulations for a conservative system and a nonconservative system are established regarding to a uniform cantilever subjected to a concentrated force and a uniform distributed force axially. The displacement of a uniform cantilever is assumed to be obtained by superposing the modal functions which are normal modes in a vacuum, and is estimated by applying the Galerkin method. Changing the forces, the eigenvalue analysis is performed, and the root locus is calculated for the stability analysis. When the system is considered to be conservative, the divergence phenomenon is confirmed to appear first. On the other hand, when the system is considered to be nonconservative, the flutter phenomenon is confirmed to appear first although the critical force becomes high. And, by changing the structural damping, the destabilized effect due to the damping is confirmed when an elastic beam is subjected to follower forces.

Motion and Vibration of a Roller Coaster Consisting of Multi-Vehicles Modeled by Two Wheels on 3D Trajectory

Katsuhisa FUJITA and Hiroaki TOSHIMITSU

Proceedings of the 6th Asian Conference on Multibody Dynamics, August 26-30, 2012, Shanghai, China, 670000 in CD-ROM (2012)

A motion and vibration of a roller coaster consisted of multi-vehicles, which moves on a complicated three-dimensional trajectory, is investigated in consideration of air resistance. By using differential algebraic equations (DAE), the simulation method for moving bodies on 3D trajectory is proposed in this paper. In the previous papers, the simulation method using s-u-z coordinate for a single vehicle has been shown, and a roller coaster has been modeled as a one-wheel vehicle. In this paper, it is modeled as a two-wheel vehicle. In addition, the simulation method for multi-vehicles of a roller coaster is proposed. In order to solve the instability of the simulation analysis, the stabilization method proposed by Baumgarte is adopted. When all of connecting points are taken into consideration as constraint conditions, it is found to be too severe, and some play is necessary at connecting points for practical applications to an actual roller coaster. Lastly, the validity of the proposed simulation method by comparing with the experiment and the simulation results using the one-wheel vehicle reported in the previous paper is examined.

Field Tests of Microbiologically Influenced Corrosion of Type 304 Stainless Steels: Effects of Seasonal Change in Bacterial Consortia and Chloride Concentration

Hiroshi KAWAKAMI, Takeshi ARAKI, Yoshihiro SATO and Yasushi KIKUCHI

The 16th International Congress on Marine Corrosion and Fouling, June 24-28, 2012, Seattle, Washington, U.S.A., pp. 49 (2012)

Type 304 stainless steel and copper alloyed antibacterial stainless steel were subjected to field tests. Plain coupon specimens dry polished with #1500 emery paper were prepared from type 304 stainless steel, as well as copper alloyed stainless steel. For type 304 stainless steel, tungsten inert gas welded coupon specimens with/without scale removal polish treatment were also prepared. The specimens were subjected to field tests at two eras in Osaka, Japan; one was the Osaka bay era and the other was in the Dotonbori river. The latter era was about five kilometers above the Osaka bay era, where sea water from the estuary and fresh water from an upper side of the river were alternatively fed in by operating a lock gate twice in a day. Seasonal change in bacterial consortia and its effects on microbiologically influenced corrosion was studied.

Planning Path by Using 3-dimensional Map Including Vertical Information

Tomoki TAJIRI, Rei OGAMI, Yogo TAKADA, Atsushi IMADU and Tadao KAWAI

Proceedings of ICIUS, MoPmC-4, CD-ROM (2011)

In this paper, we have tried generating a path from the start position to the goal position which is movable with mobile robots. The shortest path is usually the best route. But there may be high steps or steep slopes in a real environment. It is not possible for the mobile robot with wheels to move in the direction because there is the steep slope or the high step. Q-Learning is one of the method which is often used to planning path. We have made a robot learn to get path which has less gradient of ground with Q-Learning. The effectiveness of this method is investigated with an actual robot in the real environment that has steps and slopes. The experimental result shows the effectiveness of this approach.

Self-position Estimation of Small Fish Robot Based on Visual Information from Camera

Yogo TAKADA, Tsuyoshi NAKAMURA, Keisuke KOYAMA and Tomoyuki WAKISAKA

Journal of the Japan Institution of Marine Engineering, Vol.47, No.3, pp. 138-146 (2012) (in Japanese)

Autonomously working small fish robots are ideal for surveys of fish resources and underwater structural inspections where electric wires hinder the movement of the robot or where radio signals, such as GPS, cannot be received. For practical usage, the fish robot needs to estimate its self-position to swim autonomously in water. Using visual information from images taken from the bottom facing camera, self-position estimation becomes possible. Digital image correlation and tracking method is often used to measure deformation or strain of material and visualization of flow in water. Although self-position estimation of aquatic robots becomes possible when this method is applied, microcomputers (PIC, H8, AVR etc.) cannot be used for the digital image correlation method since they are unable to perform the calculations in real-time. In this study, self-position estimation was tested utilizing the real-time digital image correlation method by using a FPGA (Field Programmable Gate Array). VHDL programming for FPGA and the FPGA equipped circuit board have been originally developed. This FPGA board executes both the control of the swimming fish robot and image processing at the same time. Results confirm that the small fish robot can measure swimming distance by itself.

Target following control of Small Fish Robot FOCUS Based on Color Information

Yogo TAKADA, Tsuyoshi NAKAMURA, Keisuke KOYAMA and Tomoki TAJIRI

Trans. Jpn. Soc. Mech. Eng., Ser.C, Vol. 78, No. 792, pp. 2924-2934 (2012) (in Japanese)

It is necessary for a small aqua robot to search for a target in order to investigate creatures such as fishes in a river or lake. However, control signals by electric wave from outside do not reach a robot easily in water. Therefore, aqua robots must search the target autonomously without signals from outside. It is important for a robot to gaze forward and recognize the target in water. In this study, we have used a fish robot named FOCUS which can swim in water by using the tail fin. This robot has some micro CMOS cameras and a FPGA circuit board for data processing. A red object is detected with the CMOS camera. In addition, FPGA calculates where the red object is located in the image. This robot controls the tail fin mechanism and submersible system in order to decide the course of the robot in response to the calculated positional coordinates. We have confirmed that this robot can recognize a color target and follow the target in water.

Target Following and Self-position Estimation of Small Fish Robot FOCUS

Yogo TAKADA, Tsuyoshi NAKAMURA, Keisuke KOYAMA, Noboru FUKUZAKI, Tomoki TAJIRI and Tomoyuki WAKISAKA

Journal of the Japan Institution of Marine Engineering, Vol. 47, No. 5, pp. 108-113 (2012) (in Japanese)

Autonomous small fish robots are ideal for surveys of fish resources and underwater structural inspections where electric wires hinder the movement of the robot or where radio signals, such as GPS, cannot be received. For practical usage such as taking pictures of fishes in the sea, the fish robot needs to follow the target fish and estimate its self-position to swim autonomously in water. The authors have developed a small fish robot named FPGA Offline Control Underwater Searcher (FOCUS) which has some micro CMOS cameras and an FPGA circuit board for data processing. Red objects can be detected with the CMOS camera. Using visual information from images taken from the bottom facing camera, self-position estimation becomes possible. The self-position estimation has been tested utilizing a real-time digital image correlation method using an FPGA. Development of a VHDL program for the FPGA and the mounting of FPGA on a circuit board have been conducted for target following and self-position estimation. This FPGA board executes both the control of the swimming fish robot and image processing at the same time. Results confirm that the small fish robot can follow the target and can measure simultaneously its self-position.

Analysis for Flow around a Fish Robot by Three-dimensional Fluid-structure Simulation and Evaluation of the Propulsive Performance

Yogo TAKADA, Toshinori OCHIAI, Noboru FUKUZAKI, Tomoki TAJIRI and Tomoyuki WAKISAKA

Proc. of the Fifth International Symposium on Aero Aqua Bio-Mechanisms, Taipei, Taiwan, ISABMEC2012, S41.pdf (2012)

The propulsion velocity of fish robots are very slow compared with live fishes. It is necessary to swim at a several times faster speed than the current robots for various usages. Therefore, we are searching for the method of making the robot swim fast. The simulation before making robot is important. We have made the computational simulation program of three-dimensional fluid-structure analysis. The flow around the caudal

fin can be examined by analyzing the fin as an elastic body. We compared the results of numerical analysis with the results of experiment. As a result, both were corresponding well. Moreover, the flexibility of caudal fin has been examined by using the computational simulation.

Effect of Colloidal Silica in Chromate Film on Adhesion of Paint

Keisuke HARA, Koichi OTSUKA, Makoto IMANAKA and Yoshihiro SAWADA

J. Adhesion Soc. Jpn., Vol. 48, pp. 204-210 (2012) (in Japanese).

Effect of colloidal silica addition in a chromate coating film on interfacial physical adhesive force between the coating film and a paint layer was studied. The physical adhesive force resulting from the chromate film on a steel sheet and the paint layer coated steel sphere was evaluated by an interfacial pull-off test. The interfacial force was measured by deflection of an aluminum cantilever beam which was bonded the painted steel sphere. Two kind of steel sheets modified with chromic acid which contained colloidal silica or no silica were prepared. Physical adhesive force was higher with colloidal silica containing chromate treated steel sheet than with no colloidal silica treated steel sheet. The effect of colloidal silica on the physical adhesive force shows the same tendency of adhesive strength evaluated as the peeling probability with the cross-cut method and the critical strain energy release rate at interfacial crack initiation using an end notched flexure specimen. These results are verified that the addition of colloidal silica in chromate film is effective to increase the physical adhesive force with paint layer, so the adhesive strength becomes stronger.

Filament Winding Moulding of Biodegradable Composites Using Ramie Yarns

Hayato NAKATANI, Tatsuro KOSAKA, Katsuhiko OSAKA, Jun YOSHIDA and Yoshihiro SAWADA

J. of the Soc. of Materials Science, Japan, Vol. 61 No. 3, pp.286-291 (2012) (in Japanese)

An experimental investigation of fabricating biodegradable composite pipes by filament winding (FW) method using ramie yarn as continuous fibre reinforcements is conducted. Though ramie fibres are discontinuous fibres in origin, ramie yarns can be handled as continuous fibre due to high aspect ratio of the fibre. Influence of use of the yarn on mechanical properties of the FW pipes is also evaluated. Axial and circumferential tensile tests are conducted for the FW pipes fabricated with various winding tensions. Results demonstrate that the winding tension affects not fracture load but only fibre volume fraction of the composites. Furthermore, properties of ramie yarn in FW pipes have been focused on. It has been shown that the elastic modulus of FW pipes using ramie yarns is lower than that of angle-ply laminates while mechanical properties of FW pipes and angle-ply laminates using glass or carbon fibre are comparable. From experimental evidences, it has been found that waviness of the ramie yarns caused by their own large diameter strongly affects the mechanical properties of the FW pipes, and that the ramie yarns do not exert their properties adequately in the FW pipes.

Impact Damage Detection of FRP Laminates Based on Spectrum Analysis of Lamb Waves

Akihiro WADA, Shinya MOTOGI and Tomohiro YAMASAKI

Trans. Jpn. Soc. Mech. Eng., Ser. A, Vol. 78, No. 790, pp. 879-889 (2012)(in Japanese)

A new technique using Lamb waves has been proposed to detect impact damages in FRP laminates nondestructively. Conventional ultrasonic testing such as C-scan requires two-dimensional scanning for whole area inspection because the inspected area by one operation is relatively small. In this study, for quick detection of a localized defect, spectrum analysis of Lamb waves is demonstrated. Instead of wave velocity or attenuation, acousto-ultrasonic parameters (AU parameters), which are based on the amplitude spectrum of the broadband signal, are introduced to improve the precision of the inspection. Among the several AU parameters, A2 and A4/A3 parameters, which represent the centroid and the torsion of the spectral density curve respectively, are found to be more useful to identify a localized defect in laminated composite plates. It is also found that the inspection accuracy depends on the wave propagation direction reflecting to the scattering of higher frequency waves, and can be improved by use of burst waves.

Reduction of Extrusion Force in Equal Channel Angular Pressing

H. UENO, K. KAKIHATA, A. VINOGRADOV, Y. KANEKO and S. HASHIMOTO

Tribologist, Vol.8, pp. 506-513 (2011)(in Japanese)

The purpose of this study is to reduce the extrusion force in course of Equal Channel Angular Pressing (ECAP) by introducing a head shape of billet into the rectangular die channel and the selection of a suitable lubricant. It is found that a significant reduction of the start extrusion force is realized by applying the head shape having an inclination by 45 degrees to the die path. Then we found that newly developed fluorinated grease is much more efficient to reduce the friction force between materials and die walls than the widely used lithium grease with graphite and molybdenum disulfide. The reduction rate of the extrusion force in ECAP is estimated to be 80% by the effects of head shape of billet and lubricant. Finally, it is reported, at the

first time, that ECAP forming of SUS316L austenitic stainless steel has been realized at 150°C by the above two improvements.

Fatigue Crack Growth and Related Microstructure Evolution in Ultrafine Grain Copper Processed by ECAP

A. VINOGRADOV, T.KAWAGUCHI, Y.KANEKO and S.HASHIMOTO

Mater. Trans., Vol. 53, pp.101-108 (2012)

Fatigue crack growth tests were carried out using centre-cracked tensile (CCT) specimens of ultrafine grained (UFG) copper, aiming at clarifying microstructure evolution around the fatigue crack tip and at better understanding of fatigue crack propagation mechanisms. The fatigue crack growth tests revealed that UFG copper had the lowest threshold stress intensity factor range ΔK_{th} . On the other hand, the crack growth rates were almost identical among the UFG and conventional specimens tested at higher ΔK_{th} regime. From the microstructure observation after the fatigue crack growth test, significant grain growth was detected in the intimate vicinity to the fracture surface in UFG copper. The size of the grown grains in the UFG copper increased with increasing stress intensity factor range and with the size of the cyclic plastic zone.

Fabrication and Vickers Hardness of Electrodeposited Ni-Cu Alloy with Composition Gradient

K.UEMORI and Y.KANEKO

J. Japan Inst. Metals, Vol.76, pp. 309-313 (2012) (in Japanese)

A Ni-Cu alloy film with high composition gradient was fabricated by electrodeposition technique. Because the chemical composition of the electrodeposit depends on the applied electrochemical potential in solution containing nickel and copper ions, we could grow the gradient-composition Ni-Cu alloy film by applying a continuously variable potential wave. To obtain a relatively thick film on a substrate, the Ni-Cu layers with high positive and negative gradients were stacked alternately during the electrodeposition. In X-ray diffraction analyses, the gradient-composition film exhibited a very broad peak lying between Ni and Cu peaks, although two diffraction peaks appeared in an electrodeposited Ni/Cu multilayer fabricated using a rectangular potential wave. This broad X-ray peak was consistent with the gradient composition. Vickers hardness of the gradient-composition film was higher than that of the Ni/Cu multilayer with 100 nm layer thickness, by a factor of 1.8. The strength increment in the gradient-composition film could be explained by high-density misfit dislocations which uniformly distributed in the film.

Acoustic Emission during Hydrogen Charging of a Pipeline Steel

D.L MERSON, S.I. DEMENTIEV, A.V. IOFFE, P.V. SUVOROV and A.VINOGRADOV

ISIJ International, Vol. 51, No. 10, pp. 1682-1687 (2011)

Acoustic emission (AE) during hydrogen-induced cracking (HIC) of low-carbon pipeline steel immersed into H₂S containing media was investigated aiming at discriminating between damage mechanisms and getting a better insight on the kinetics of damage. Two kinds of steel samples - sensitive and resistant to hydrogen induced cracking - were tested. Three different kinds of acoustic emission signals were discriminated by a cluster analysis involving either spectral shape recognition or parametric c-means classifier. It is demonstrated that AE is associated with three primary mechanisms involving hydrogen bubbles evolution, sulfide film formation and fracture due to HIC. Hence, AE is shown to be very efficient for quantitative description of hydrogen induced damage accumulation in steels.

Enhanced Fatigue Properties of Nanostructured Austenitic 316L Stainless Steel

H.UENO, A.VINOGRADOV, K. KAKIHATA, Y.KANEKO and S.HASHIMOTO

Acta Materialia, Vol. 59, pp. 7060–7069 (2011)

The present communication reports on the substantial improvement in monotonic and cyclic strength of austenitic 316L stainless steel nanostructured during equal channel angular pressing (ECAP). The ultimate tensile strength and the fatigue limit after ECAP exceed 1.3 GPa and 550 MPa, respectively, while the ductility was not fully compromised. Microstructural observations showed that these excellent mechanical properties can be attributed to the nanostructure created due to intensive twinning, with an inter-twin spacing of 30–40 nm.

Probing Shear-Band Initiation in Metallic Glasses

D. KLAUMÜNZER, A. LAZAREV, R. MAAß, F.H. DALLA TORRE, A. VINOGRADOV and J.F.

LÖFFLER

Physical Review Letters, Vol. 107, pp. 185502 (2011)

In situ acoustic emission monitoring is shown to capture the initiation of shear bands in metallic glasses. A model picture is inferred from stick-slip flow in granular media such that the origin of acoustic emission is attributed to a mechanism of structural dilatation. By employing a quantitative approach, the critical volume change associated with shear-band initiation in a metallic glass is estimated to be a few percent only. This result agrees with typical values of excess free volume found in the supercooled liquid regime near the glass transition temperature.

The Control of Texture to Improve High-Cyclic Fatigue Performance in Copper after Equal-Channel Angular Pressing

D. ORLOV and A. VINOGRADOV

Material Science and Engineering A, Vol. 530, pp. 174–182 (2011)

High-cyclic fatigue life in ultra-fine grained materials fabricated by equal channel angular pressing (ECAP) suffers from a specific shear texture induced during the fabrication as has been demonstrated in the present study on the example of pure copper. This texture promotes orientation of the easy glide crystallographic planes to be aligned parallel to the shear plane in ECAP. If specimens for the following fatigue tests are cut parallel to the pressing direction, the alignment of the easy glide crystallographic planes deteriorates the fatigue performance. It is demonstrated that the deteriorative effect can be alleviated through the controlled degradation of the texture. This goal can be achieved through (i) a consecutive ECAP processing up to equivalent strains of more than $\epsilon \geq 8$ requiring eight and more passes, or (ii) a pure-shear based post-ECAP processing to the equivalent strains as low as $\epsilon = 0.22$. The second route is thought to be most effective in practical applications where improved fatigue performance is of concern.

On the Strain Rate Dependence of Acoustic Emission During Hydrogen-Assisted Cracking of High Carbon Steel

E. D. MERSON, D.L. MERSON, M.M. KRISHTAL and A. VINOGRADOV

Journal of Acoustic Emission, Vol. 29, pp. 210-219 (2011)

The classic problem of hydrogen-assisted cracking (HAC) is revisited in the present work aiming at clarification of damage mechanisms leading to failure of hydrogen charged high-carbon steels under load. Plastic deformation and hydrogen-assisted intergranular and transgranular fracture have been clearly distinguished by acoustic emission (AE) at different strain rates. AE features corresponding to these major mechanisms are discussed.

Dominant Role of Dislocation Hardening in Monotonic and Cyclic Strength of Severely Plastically Deformed Metals

A. VINOGRADOV, M. MARUYAMA, Y. KANEKO and S. HASHIMOTO

Philosophica Magazine, Vol. 92, pp.666–689 (2012)

The present study aims at clarifying the role of dislocation strengthening in fatigue of materials manufactured by severe plastic deformation (SPD) techniques. Employment of single crystals hardened via equal channel angular pressing (ECAP) helps to minimise or completely eliminate the effect of high angle boundaries on strengthening and fatigue behaviour. Both monotonic strength and high cycle fatigue (HCF) resistance were improved significantly after the first ECAP pressing, when low-angle dislocation configurations dominate in the microstructure. The essential role of dislocation accumulation during severe plastic deformation is highlighted for both tensile and fatigue strength (SPD). Dilute alloying of copper by silver stabilises the deformation microstructure and further improves the fatigue properties considerably.

Continuous Acoustic Emission during Intermittent Plastic Flow in α -Brass

A. VINOGRADOV and A. LAZAREV

Scripta Materialia, Vol. 66, pp.745–748 (2012)

The Portevin–Le Chatelier effect which is usually associated with discontinuities in plastic flow has been studied in α -brass using an acoustic emission (AE) technique. It is found that intermittent plastic flow in the high-strain-rate regime corresponding to A-type serrations on the stress–strain diagram is accompanied by a continuous AE signal reflecting a smooth dynamics of emitting sources. No individual transient AE signals, which could be associated with rapid dislocation avalanches, have been resolved at different timescales.

Evolution of Fractal Structures in Dislocation Ensembles during Plastic Deformation

A. VINOGRADOV, I. S. YASNIKOV and Y. ESTRIN

Physical Review Letters, Vol. 108, pp.205504 (2012)

Based on the irreversible thermodynamics approach to dislocation plasticity of metals, a simple description of the dislocation density evolution and strain hardening was suggested. An analytical expression for the fractal dimension (FD) of a cellular (or tangled) dislocation structure evolving in the course of plastic deformation was obtained on the basis of the dislocation model proposed. This makes it possible to trace the variation of FD of the dislocation cell structure with strain by just measuring the macroscopic stress-strain curve. The FD behavior predicted in this way showed good agreement with the experimentally measured FD evolution at different stages of deformation of a Ni single crystal and a Cu polycrystal. One new result following from the present model is that the FD of the bulk dislocation structure in a deforming metal peaks at a certain strain close to the onset of necking. The significance of fractal analysis as an informative index to follow the spatial evolution of dislocation structures approaching the critical state is highlighted.

Effect of Strain Rate on Acoustic Emission During Hydrogen Assisted Cracking in High Carbon Steel

E.D. MERSON, M.M. KRISHTAL, D.L. MERSON, A.A. EREMICHEV and A. VINOGRADOV

Materials Science and Engineering A, Vol. 550, pp.408-417 (2012)

Hydrogen charging of a high carbon spring steel exerts a profound effect on the ductility and damage accumulation during three-point-bending testing. Since the acoustic emission (AE) technique reflects perhaps in the best way microfracturing dynamics, it is found particularly useful for real-time capturing of hydrogen assisted cracking and overall in situ tracing of damage evolution during deformation. In the present work the propensity for hydrogen assisted cracking, its mechanisms and strain rate dependence are investigated using integral characterization of AE paired with microstructure investigations. Analysis of experimental data suggests that two competitive mechanisms operate during three-point bending deformation of the high carbon steel: (i) highly localized plastic deformation and (ii) brittle intercrystalline and transcrystalline cracking promoted by hydrogen influence. The synergistic interplay between these two mechanisms is discussed.

Improvement of Fatigue Strength of a Mg–Zn–Zr Alloy by Integrated Extrusion and Equal Channel Angular Pressing

A. VINOGRADOV, D. ORLOV and Y. ESTRIN

Scripta Materialia, Vol. 67, pp.209-212 (2012)

Fatigue performance under axisymmetric push–pull loading of a magnesium alloy Mg–6Zn–0.5Zr (ZK60) after processing by integrated extrusion and equal-channel angular pressing was investigated. Such processing was shown to nearly treble the endurance limit of the alloy, raising it to 160 MPa. It was established that the high-cycle fatigue performance of ZK60 is primarily controlled by dislocation substructure, grain size and crystal orientation, rather than the presence of intermetallic particles.

A New Method For AE Signal Processing: “Virtual Sensor” Technique

S.LAZAREV, A. LAZAREV, F.PLETENEV and A.VINOGRADOV

Proc. of World Congress on Acoustic Emission, Beijing, China, 2011, pp.210-215 (2011)

A new method of signal recognition is proposed upon the assumption that the AE signal is created by a highly correlated source within a solid body. It therefore should have a more stable phase than an arbitrary noise at the same frequency. Hence, in contrast to the Fourier transform, the proposed “resonance” method attempts to emphasize the phase of the signal.

Continuous Acoustic Emission During Intermittent Plastic Flow of a-Brass

A.LAZAREV, R.TAKEDA and A.VINOGRADOV

Proc. of World Congress on Acoustic Emission, Beijing, China, 2011 pp.179-184 (2011)

The long-standing problem of AE during plastic deformation in materials is revisited with new experimental capabilities provided by broadband threshold less AE data streaming with high acquisition rate followed by detailed spectral and statistical analysis of waveforms. No apparent evidence for the presence of dislocation avalanches or any related steep changes in the behaviour of dislocation ensembles is found.

Mechanisms of Plastic Deformation and Acoustic Emission in ZK60 Mg Alloy

A.VINOGRADOV, A. DANYUK and E.POMPONI

Proc. of 7th Int. Conference of Acoustic Emission, Granada, Spain 12-15 Sept. 2012 (CD edition)(2012)

Since most of wrought magnesium alloys, including ZK60, are relatively new, understanding of their mechanical behaviour is still vague. One of the main challenges in designing Mg alloys is the improvement

of their ductility, which relies heavily on clear understanding of the synergistic interplay between two primary deformation mechanisms – dislocation glide and twinning. The present study is aimed at clarification of the role of both mechanisms operating in Mg alloys using the acoustic emission (AE) technique. The Fourier spectral analysis paired with the novel signal categorization technique has been utilized in the present work for this purpose. The stages of deformation are discussed in view of the interaction between main underlying mechanisms.

Real-time Acoustic Emission Classification: New Evolutionary Approach

E. POMPONI and A. VINOGRADOV

Proc. of 7th Int Conference of Acoustic Emission, Granada, Spain 12-15 Sept. 2012 (CD edition) (2012)

Since most of wrought magnesium alloys, including ZK60, are relatively new, understanding of their mechanical behaviour is still vague. One of the main challenges in designing Mg alloys is the improvement of their ductility, which relies heavily on clear understanding of the synergistic interplay between two primary deformation mechanisms – dislocation glide and twinning. The present study is aimed at clarification of the role of both mechanisms operating in Mg alloys using the acoustic emission (AE) technique. The Fourier spectral analysis paired with the novel signal categorization technique has been utilized in the present work for this purpose. The stages of deformation are discussed in view of the interaction between main underlying mechanisms.

Formation of the Microstructure of TiO₂ Film Through Anodic Oxidation of Titanium

Y. YOKOGAWA, T. YASUKI, T. HIROTOMI, A. NAKAMURA and I. KISHIDA

Mater. Sci. Eng., Vol. 18, pp. 182003 (2011)

Recent titanium oxide nanotube arrays have attracted attention for their applications. Titanium oxide nanotubes were prepared under potentiostat conditions (10 - 60 V) for various times (1 min - 3 hr). SEM observations revealed that the pore sizes of the nanotubes have a tendency to increase with an increase in the applied potential in the NH₄F-glycerol-H₂O electrolyte. Some corrosive pores were observed on the surface of titanium substrate at 40 V for 1 minute at 40°C. The pores covered the surface of the titanium substrate after 10 minutes, and some small pores were observed in the inner part of the pores, which should correspond to the combining of some small adjacent pores into a large one. The combining of the tubes were observed after 2 h and 3 h anodization times, and the nanotube arrays seem to be formed upward from the SEM side-views. The photocatalytic activity of the titanium oxide nanotubes was evaluated according to the JIS standard (JIS R 1703-2). The R factor of the titanium oxide nanotube arrays formed at 40 V and 40 °C for a 3h the anodization time was 9.71 n mol/l·min, which was twice that of the titanium oxide thin film obtained by the rf-sputtering method.

Synthesis of Microporous Materials and Their VSC Adsorption Properties,

Y. YOKOGAWA, H. MORIKAWA, M. SAKANISHI, H. UTAKA, A. NAKAMURA and I. KISHIDA

Mater. Sci. Eng., Vol. 18, pp. 192011 (2011)

Oral malodor is caused by volatile sulfur compounds (VSC) such as hydrogen sulfide (H₂S), methyl mercaptan and dimethyl sulfide produced in mouth. VSC induces permeability of mucous membrane and oral malodor formation. Thus, the adsorbent which highly adsorbs VSC should be useful for health in mouth and may prevent teeth from decaying. The microporous material, hydrotalcite, was synthesized by a wet method, and the H₂S adsorption was studied. The samples, identified by powder X-ray diffraction method, were put into glass flask filled with H₂S gas. The initial concentration of H₂S was 30 ppm. The change in concentrations of H₂S was measured at rt, and the amount of H₂S absorbed on the hydrotalcite for 24 h was 300 micro L/g. The samples were taken out from the above glass flask and put into a pyrolysis plant attached to gas chromatography-mass spectrometry to determine the amount of H₂S desorbed from samples. Only 3 % of H₂S was desorbed when heated at 500 °C. H₂S in water was also found to adsorb into hydrotalcite, which was confirmed by the headspace gas chromatography with flame photometric detector. The hydrotalcite material should be expected to be an adsorbent material, useful for health in mouth.

TEM Observation of Biomolecules on/in Mesoporous SBA-15

Yoshiyuki YOKOGAWA, Akira SAITO, Naoki OGAWA, Atsutomu NAKAMURA and Ippei KISHIDA

Key Engineering Materials. Vol. 493-494, pp. 728-731 (2012)

The encapsulation and immobilization of biomolecules on/in mesoporous silica materials (MPS) have been studied by using transmission electron microscopy (TEM). The mixture of tetraethyl orthosilicate (TEOS) and the triblock copolymer as a template was stirred, hydrothermally treated to form the mesoporous

SBA-15 structure, and heat-treated at 550 °C. SEM observation indicated that long and narrow particles were linked together in the long axis direction to form secondary particles of SBA-15. UV-spectrometry was performed to determine the amount of bovine serum albumin (BSA), cytochrome C, myoglobin or β -lactoglobulin encapsulated on/in SBA-15. The time profiles for adsorption of proteins can be well described by intraparticle diffusion model. The TEM observations of proteins on/in mesoporous SBA-15 revealed that proteins were embedded on/in mesoporous SBA-15 and the protein behaviors given by TEM observations may correspond to the intraparticle diffusion model.

Synthesis and Characterization of Iron Oxide Embedded Hydroxyapatite Bioceramics

Ereath Beeran ANSAR, Manmadhan AJEESH, Yoshiyuki YOKOGAWA, Wilfried WUNDERLICH and Harikrishna VARMA

J. Amer. Ceram. Soc., Vol. 95, No. 9, pp. 2695–2699 (2012)

A homogeneous dispersion of nano iron oxide (IO) crystallites inside the hydroxyapatite (HA) particles was achieved by a co-precipitation method. This highly stable colloidal dispersion of magnetic nano composite (HAIO) was made without the use of any surfactants. The *in situ* generated dispersion of the composite powders showed submicron HA particles with ~5 nm iron oxide inside. The phase analysis results showed the presence of hydroxyapatite (HA) and iron oxide with no tertiary phase. The enhancement of relative peak intensities with increased percentage of iron oxide phase in X-ray diffraction analysis suggests the formation of iron oxide together with HA without affecting the phase purity of the latter, which is important when the biological behavior of HA is concerned. This also confirms the quantitative nature of the precipitated nanocomposites. The High Resolution Transmission Electron Microscope (HRTEM) of the composite shows elongated crystal flakes or platelike surfaces of HA crystallites having particle sizes in the range 70–100 nm. HRTEM with XRD analysis matches HAIO only with iron oxide particles of Magnetite (Fe₃O₄) and HA phases. The FTIR data confirm that the introduction of iron oxide did not produce any considerable change in the chemical structure of HA.

Fabrication of Porous Hydroxyapatite Ceramic Scaffolds with High Flexural Strength Through the Double Slip-Casting Method Using Fine Powders

Yin ZHANG, Deshuang KONG, Yoshiyuki YOKOGAWA, Xia FENG, Yaqiu TAO and Tai QIU

J. Am. Ceram.Soc., Vol. 95, No. 1, pp.147–152(2012)

A new technique of twice combining the slip-casting and polymer sponge methods using a slip with different viscosity is introduced in the study to prepare bimodal pore size hydroxyapatite scaffolds, which provides a better control over the microstructures of scaffolds and enhances their mechanical properties. With the technique, we were able to produce scaffolds with mechanical and structural properties that cannot be attained by either the polymer sponge or slip-casting methods alone, or by the polymer sponge and slip-casting once method.

The flexural strength of porous ceramics scaffolds should depend on porous framework. In this study, a new approach combining the twice slip-casting and polymer sponge methods to fabricate porous HAp scaffolds was developed that has the combined advantages of both the methods. A flexural strength of 73.3 MPa for the scaffold with porosity of 52.5% was developed. The resultant bimodal porous HAp ceramics scaffolds should show very high flexural strength. This study shows that the bimodal pore structure of an HAp scaffolds obtained could be potentially suitable for applications as a biomedical bone replacement material.

VSC Adsorptive Properties into Ion Exchanged Zeolite Materials in Gaseous and Aqueous Medium

Y. YOKOGAWA, M. SAKANISHI, N. MORIKAWA, A.NAKAMURA, I. KISHIDA and H.K.VARMA

Procedia Engineering, Vol. 36, pp.158-172 (2012)

The microporous materials, zeolite, were synthesized and the H₂S adsorption into microporous material was studied. Zeolite has three dimensional framework structure in which SiO₄ and AlO₄ tetrahedrons are bonded, and generally contains alkali metal or alkali-earth metal atoms as univalent or bivalent cations. These electrostatic effect results in the surface potential of zeolite materials, and may influence the adsorptive properties. Two kinds of zeolite materials, LTA (Zeolite A) and MFI (ZSM-5), which have different Si/Al ratios, were synthesized by a wet method. Some starting materials were dissolved in water, and the mixture was heated, filtered, washed, and dried. The Ag-doped zeolite materials were prepared as follows. The sample was put into 2M silver nitrate solution and stirred. The obtained specimen was filtered and washed with water, then dried at 90°C for 24 hrs. The samples, identified by powder X-ray diffraction method, were put into a 5 L glass flask filled with H₂S gas. The initial concentration of H₂S was 30 ppm. When 0.02 g of LTA was applied, the concentration of H₂S fell to 84% for first 2 hours, and was decreased with time. The

equilibrium did not seem to reach even for 24 hours. The amount of LTA was increased to be 0.2 g, and then the concentration of H₂S was decreased to be less than 20 % for 24 hrs. In case of Ag-doped LTA, the concentration of H₂S dropped to be 24 % for 2 hrs and to be almost 0 % for 4 hrs. The exchanges of alkali metal or alkali-earth metal atoms to univalent or bivalent metal ions zeolite material remarkably improves the H₂S reduction. The amount of adsorbed H₂S onto LTA was larger than onto MFI. The difference in the amount of adsorbed H₂S between two types of zeolites can be explained by the surface potential. Polarity of zeolites depends on their Si/Al ratio. XRD patterns of the LTA and H₂S adsorbed LTA specimens seem to be almost identical, and the peaks corresponding to Ag₂S was not observed. So sulfur may be included in zeolite structure. The XRD analysis should be investigated in great detail for further study. H₂S in aqueous medium was also found to adsorb into microporous material, which was confirmed by the headspace gas chromatography with flame photometric detector. The microporous material should be expected to be an adsorbent material, useful for health in mouth.

Synthesis, Characterization and in vitro Studies of Zinc and Carbonate Co-Substituted Nanohydroxyapatite for Biomedical Applications

G. Suresh KUMAR, A. THAMIZHAVEL, Y. YOKOGAWA, S. Narayana KALKURA and E.K. GIRIJA
Materials Chemistry and Physics, Vol. 134, No. 2–3, pp.1127–1135 (2012)

Ionic substitutions have been proposed as a tool to improve the properties of hydroxyapatite (HA). Zinc and carbonate co-substituted HA have been synthesized by precipitation method and characterized by XRD, FT-IR, XRF, FESEM and TEM. Comparative studies were carried out with HA, zinc substituted HA and carbonate substituted HA. Zinc substituted HA exhibited less dissolution and apatite forming ability but more decomposition into TCP at 1400 °C when compared with carbonate substituted HA. When zinc is co-substituted with carbonate it exerted a control over the apatite forming ability of HA which was found to lie in between the individual substituted samples without compromising the dissolution behavior of CHA. Also, decomposition was reduced to a greater extent. Hence tailoring the properties of HA to the desired extent can be achieved by simultaneous substitution of zinc and carbonate.

Fabrication of Hydroxyapatite Calcite Nanocomposite

E.K. GIRIJA, G. Suresh KUMAR, A. THAMIZHAVEL, Y. YOKOGAWA, S. Narayana KALKURA and R. NARAYAN

Advances in Bioceramics and Porous Ceramics IV: Ceramic Engineering and Science Proceedings, Vol. 32, pp.3-11, John Wiley & Sons, USA (2011)

Hydroxyapatite (HA) and calcite are known natural biomineral. HA is known to be bioactive and bioresorbable but the rates are too low. On the other hand, calcite is highly biodegradable. The combination of HA and CaCO₃ can compromise the demerits of each other. Here a method is presented for the simultaneous synthesis of HA and calcite employing sol-gel process. The product obtained was a nanocomposite with enhanced bioactivity and elastic constants and fracture toughness similar to that of HA.

The VSC Adsorption on Hydrotalcite Through Topochemical Reactions

Yoshiyuki YOKOGAWA, Yutaro YAGI, Hroya SANO, Atsutomu NAKAMURA and Ippei KISHIDA
Key Engineering Materials, Vol. 529-530, pp 650-653 (2013)

Volatile sulfur compounds (VSCs) such as hydrogen sulfide (H₂S), methyl mercaptan and dimethyl sulfide produced in mouth. Some oral (Gram-negative) bacteria produce VSCs, which induces permeability of mucous membrane, cause the oral malodor, dental caries, color change of the dental fillings. Thus, material which adsorbs VSCs should be useful to keep health in mouth. Previously, we reported the H₂S adsorptive properties of zeolite and hydrotalcite materials having micro pores. The amount of H₂S adsorbed on the zeolite or hydrotalcite at room temperature was found to be around 300-400 ppm, and 3 % of H₂S was desorbed when heated at 400 °C. The hydrotalcite, whose composition is Mg_{1-x}Al_x(OH)₂A_{x/n}·mH₂O, where A is CO₃²⁻, and x is 0.25, was heat-treated at 500 °C, and put into aqueous solution containing H₂S. In this study, the relation between heat-treatment temperature and the sulfide adsorption on hydrotalcite in aqueous solution was investigated. The hydrotalcite materials were hydrothermally synthesized and identified by powder X-ray diffraction method. The change in concentrations of H₂S in aqueous solution was measured using FPD gas chromatography (GC). The concentrations of H₂S was decreased with time for the hydrotalcite heated at 500 °C or 600 °C, and fell to 20 % for 12 hours. But, the concentration was decreased by 40% for 12 hours for the hydrotalcite materials heated at higher temperature. XRD and FT-IR analysis revealed that the sulfides were into or out of the hydrotalcite structure through topochemical reactions.

Time-Dependent Protein Adsorptive Behavior on/in Mesoporous Silica Materials

Yoshiyuki YOKOGAWA, Yuta YAMATO, Shinji ITO, Atsutomo NAKAMURA and Ippei KISHIDA
Key Engineering Materials, Vol. 529-530, pp 646-649 (2013)

The time – dependent adsorptive behavior of biomolecules on/in mesoporous silica materials (MPS) have been studied by using transmission electron microscopy (TEM). Highly ordered hexagonal mesoporous silica materials (SBA-15) synthesized were immersed in phosphate buffer saline (PBS) solution containing cytochrome C for 2, 48, and 120 hours at 4 °C. After that, MPS materials were rinsed with PBS solution, and then immersed in PBS solution without cytochrome C. The amount of protein adsorbed on/in MPS materials soaked for 2, 48, and 120 hours was 75 mg/g, 135 mg/g and 178 mg/g, respectively. The time profiles for adsorption of proteins can be well described by intraparticle diffusion model. The holes of MPS materials were observed to be overlapped with stained proteins for first 2 hours immersion. The stained proteins were observed between primary particles and partly inside the mesoporous channels in the MPS material immersed for 48 hours. For MPS immersed for 120 hours, stained proteins were observed in almost all meso-scale channels of MPS. The ratio of desorbed proteins from those embedded on/in MPS materials was 13 % in case of the MPS materials immersed in PBS containing cytochrome C for 2 hours, while 8 % in case of the MPS materials immersed for 48 and 120 hours. Cytochrome C may be strongly embedded on/in MPS materials due to the electrostatic effect.

L2-well-posed Cauchy Problem for Fourth-order Dispersive Equations on the Line

Shigeo TARAMA

Electron. J. Diff. Equ., Vol. 2011, No. 168, pp. 1-11 (2011)

In this paper we consider the Cauchy problem for dispersive equations on the real line and study the well-posedness of the above problem in the space of square integrable functions. Treating the equations with the constant dispersive term, we investigate the conditions on the lower order terms for the well-posedness. The sufficient and necessary conditions are known for the equations with the third order dispersive term. In the case of fourth order dispersive term, the sufficient conditions are known but their necessity is shown under some additional conditions. In this paper we prove that the known sufficient conditions are also necessary for the well-posedness.

Electrical Engineering

SU-8 ridge-waveguide with holographic grating embedded in nanoimprinted groove,

Tahito AIDA, Takao TOKUHARA, Shusuke ASAHI, Hiroya MATSUKAWA, Hiroshi KUMAGAI

Microelectronic Engineering, Vol. 98, pp.258-261, (2012).

Fabrication of SU-8 slab- and ridge-waveguides with holographic grating for DFB laser, effectively utilizing nanoimprint technology (NIL), is presented. Rhodamine-6G-doped SU-8 slab- and ridge-waveguides were embedded in grooves defined by NIL in UV curable resin. Utilization of NIL made it easier to form such a three-dimensional micro structure consisting of ridge stripe and fine corrugation grating. TE-polarized 587 nm laser and TE-polarized 594 nm light emissions were observed from the slab- and ridge-waveguides, respectively, when the waveguides were irradiated by 532 nm pulsed Nd:YAG laser.

Floating three-dimensional display with 360-degree viewing angle

D. MIYAZAKI, N. AKASAKA, K. OKODA, Y. MAEDA, and T. MUKAI

Stereoscopic Displays and Applications XXIII, Proc. Soc. Photo-Opt. Instrum. Eng., Vol. 8288, pp. 82881H-1-82881H-6 (2012).

The aim of this research is to develop a full-parallax auto-stereoscopic display system, which can generate a floating three-dimensional (3-D) image viewable from a surrounding area. A 3-D display method based on the combination of integral imaging, 360-degree scanning with a rotating mirror, and imaging in the air with a concave mirror is proposed. A scanning system is composed of a hemisphere concave mirror and a mirror scanner, which is located around the center of the concave mirror. By putting an image generated by an integral imaging system into the scanning system, a floating stereoscopic image can be formed around the center of the concave mirror. When the mirror scanner rotates and the image on the integral imaging system is switched in accordance with mirror angle, each directional image can be observed from each viewing angle. The feasibility of the proposed method was examined by preliminary experiments. The abilities of generation of a floating full-parallax image and a floating auto-stereoscopic image with 360-degree viewing angle are demonstrated.

Volumetric three-dimensional display based on scanning by an optical real image

D. MIYAZAKI

The First Korea-Japan Workshop on Digital Holography and Information Photonics, DHIP 2011, pp. 61-62 (2011).

The volumetric display can form a true three-dimensional (3-D) image, whose pixels are distributed in a 3-D space. Volumetric display methods have been proposed to form a floating 3-D images from a two-dimensional (2-D) real image moved quickly with an optical scanner for scanning a 3-D space. Demonstrations of volumetric display systems for verifying the proposed method are described. Concave mirrors or a micro-mirror array device are used as imaging optical elements, and a digital micromirror device (DMD) is used as a 2-D spatial light modulator with a high frame rate. In order to form a volumetric image, the DMD displays a few hundreds of cross-sectional images of a 3-D object, while the real image is moved with a mirror scanner.

Improvement of confocal three-dimensional measurement with an inclined plane using a dynamic light source with a digital micromirror device

K. SUE, D. MIYAZAKI, T. MUKAI

The First Korea-Japan Workshop on Digital Holography and Information Photonics, DHIP 2011, pp. 93-94 (2011).

The confocal system with an inclined plane can measure three-dimensional profile of an object surface at higher speed than conventional systems. However a pitch of the pinhole-array fixes its measurement resolution of the direction which is vertical to both the optical axis and a scanning direction. It is difficult to improve the direc-

tional resolution, because the pitch of the pinholes need to keep off crosstalk. In this study we use a digital micromirror device (DMD) in place of pinhole-array. To change the distribution of sampling points dynamically. We propose the algorithm to arrange the pattern of DMD for effective measurement using the information that is acquired in advance.

Volumetric display using a rotating prism sheet and two concave mirrors

Y. MAEDA, D. MIYAZAKI, T. MUKAI

The First Korea-Japan Workshop on Digital Holography and Information Photonics, DHIP 2011, pp. 91-92 (2011).

We developed a volumetric display using a rotating prism sheet for scanning an image plane. Rays of a two dimensional image displayed on a screen are collimated by a first concave mirror and scanned by the rotating prism sheet. The rays are formed as a real image plane by a second concave mirror. Accumulation of the image planes forms a volumetric image in midair. The size of the image was approximately $6 \times 6 \times 6$ cubic centimeters.

Three-dimensional display based on volume scanning with a floating real image

D. MIYAZAKI

The 12th International Meeting on Information Display, IMID 2012, 59-1 (2012).

Three-dimensional (3-D) display technologies based on 3-D scanning with an optical real image are described. A volumetric display generates a 3-D image consisting voxels distributed in the air. Optical imaging devices, such as a concave mirror and a micro-mirror array device, are used to form a real image. A mirror scanner and a rotating prism sheet are examined for 3-D scanning. In addition, a display system, which can generate a floating 3-D image viewable from a surrounding area, is described. This display system utilizes integral imaging, scanning with a rotating mirror, and imaging in the air with a concave mirror.

Frequency-Tunable Terahertz Electromagnetic Wave Emitters Based on Undoped GaAs/*n*-Type GaAs Epitaxial Layer Structures Utilizing Sub-Picosecond-Range Carrier-Transport Processes

H. TAKEUCHI, J. YANAGISAWA, S. TSURUTA, H. YAMADA, M. HATA, and M. NAKAYAMA
J. Lumin., Vol. 131, pp. 531–534 (2011).

We have investigated sub-picosecond-range carrier-transport processes in undoped GaAs/*n*-type GaAs (*i*-GaAs/*n*-GaAs) epitaxial layer structures with various *i*-GaAs-layer thicknesses d ranging from 200 to 2000 nm, focusing on the relation between carrier-transport processes and terahertz electromagnetic wave frequency. Initially, using numerical simulation and photoreflectance measurement, we confirm that a decrease in d enhances the built-in electric field in the *i*-GaAs layer. In the time-domain terahertz waveform, it is observed that the intense monocycle oscillation induced by the surge current of photogenerated carriers, the so-called first burst, is followed by the oscillation patterns originating from the coherent GaAs longitudinal optical (LO) phonon. From the Fourier power spectra of the terahertz waveforms, it is clarified that the decrease in d causes a high frequency shift of the band of the first burst. Consequently, we conclude that, in the sub-picosecond time range, the photo-generated carriers are monotonously accelerated by the built-in electric field without being affected by intervalley scattering. The present conclusion signifies that the frequency-tunable terahertz emitters are realized by controlling *i*-GaAs-layer thickness. We also find the intensity of the coherent LO phonon band is enhanced by a decrease in d .

DOI:10.1016/j.jlumin.2010.09.022

Detection of a Coherent Longitudinal Optical Phonon in a GaAs Buffer Layer Optically Covered with a GaSb Top Epitaxial Layer Using Terahertz Spectroscopy

H. TAKEUCHI, S. TSURUTA, and M. NAKAYAMA
AIP Conf. Proc., Vol. 1416, pp. 84–87 (2011).

We demonstrate that, in a GaSb/GaAs epitaxial structure, the coherent longitudinal optical (LO) phonon in the GaAs layer optically covered with the GaSb top layer is observed utilizing terahertz spectroscopy. In the terahertz-wave measurement, the Fourier power spectrum of the terahertz waveform exhibits both the GaAs and the GaSb LO phonons; namely, the coherent LO phonon in the optically covered GaAs buffer layer is observed in the terahertz-wave measurement. This fact demonstrates that the instantaneous surface potential modulation originating from the impulsive carrier excitation by the pump pulses reaches the GaAs buffer layer. This surface potential modulation generates the coherent GaAs LO phonon.

DOI:10.1016/1.3671704

Electric Field Effects on Reduced Effective Masses of Minibands at the Mini-Brillouin-Zone Center and Edge in a GaAs/AlAs Superlattice

M. NAKAYAMA and T. KAWABATA
J. Appl. Phys., Vol. 111, 053523 (4 pages) (2012).

We have investigated the electric-field-strength dependence of the reduced effective masses of the minibands in a GaAs/AlAs superlattice embedded in a *p-i-n* diode structure with use of electroreflectance spectroscopy. Frantz-Keldysh (FK) oscillations are observed in the energy region between the $n=1$ heavy hole to electron transition at the mini-Brillouin-zone center ($k_z=0$: Γ point) and that at the edge ($k_z=\pi/D$: π point), where D is the superlattice period. Analyzing the FK oscillations, we evaluate the reduced effective masses at the Γ and π points as a function of electric field strength. The evaluated reduced effective masses are consistent with the values estimated from the calculated miniband dispersion relations in a low electric field regime. It is found that the reduced effective masses tend to be heavier at a given electric field strength. Considering the electric-field-strength dependence of eigenstates calculated using a transfer-matrix method, we conclude that an increase of the reduced effective masses originates from weak localization of the electron envelope function in the transformation process from the miniband to Stark-ladder states in Wannier-Stark localization.

DOI: 10.1063/1.3692051

Frequency-Tunable Quantum Beats under a Franz–Keldysh Oscillation Condition in a GaAs/Al_xGa_{1-x}As Superlattice

T. HASEGAWA, Y. TAKAGI, and M. NAKAYAMA

Appl. Phys. Express, Vol. 5, 041202 (3 pages) (2012).

We have investigated quantum beats (QBs) related to miniband states under a Franz–Keldysh oscillation condition in a GaAs/Al_{0.1}Ga_{0.9}As superlattice. Franz–Keldysh oscillations, which correspond to electric-field-induced oscillations of optical transition energies in a miniband regime, were clearly detected by electroreflectance spectroscopy. The frequency of the QB changes markedly with an increase in the electric field strength. This frequency change corresponds to the difference between the energy of the $n=1$ heavy-hole exciton and that of the Franz–Keldysh oscillation, depending on the electric field strength. The frequency tunability of this QB is quite different from that of a Bloch oscillation.

DOI: 10.1143/APEX.5.041202

Ultrafast Optical Response Originating from Carrier-Transport Processes in Undoped GaAs/*n*-Type GaAs Epitaxial Structures

T. HASEGAWA, Y. TAKAGI, H. TAKEUCHI, H. YAMADA, M. HATA, and M. NAKAYAMA

Appl. Phys. Lett., Vol. 100, 211902 (4 pages) (2012).

We have investigated ultrafast optical responses of undoped GaAs/*n*-type GaAs (*i*-GaAs/*n*-GaAs) epitaxial structures at room temperature using a reflection-type pump-probe technique. The built-in electric field in the *i*-GaAs layer is controlled by its thickness. It is found that the decay time of a photoexcitation-induced reflectivity change in a sub-picosecond range decreases with an increase in the built-in electric field strength. The observed optical response is related to the transport process of photogenerated carriers from the *i*-GaAs layer to the *n*-GaAs layer. The shortest response time about 60 fs demonstrates that the *i*-GaAs/*n*-GaAs structure is useful for ultrafast optical applications.

DOI: 10.1063/1.4720157

Intense Monochromatic Terahertz Electromagnetic Waves from Coherent GaAs-like Longitudinal Optical Phonons in (11*n*)-oriented GaAs/In_{0.1}Al_{0.9}As Strained Multiple Quantum Wells

H. TAKEUCHI, S. ASAI, S. TSURUTA, and M. NAKAYAMA

Appl. Phys. Lett., Vol. 100, 242107 (4 pages) (2012).

We demonstrate that, in (11*n*)-oriented GaAs/In_{0.1}Al_{0.9}As strained multiple quantum wells, the terahertz electromagnetic wave from the coherent GaAs-like longitudinal optical (LO) phonon is enhanced by a piezoelectric field originating from a tensile strain in the GaAs layer. The presence of the tensile strain is confirmed using Raman scattering spectroscopy. The Fourier power spectrum of the terahertz waveform shows that the intensity of the terahertz band of the coherent GaAs-like LO phonon increases as the index n approaches 1. The amplitude of the GaAs-like LO phonon is proportional to the piezoelectric field in the strained GaAs layer.

DOI: 10.1063/1.4729125

Quantum Beats of Type-I and Type-II Excitons in an In_xGa_{1-x}As/GaAs Strained Single Quantum Well

O. KOJIMA, K. MIZOGUCHI, and M. NAKAYAMA

J. Appl. Phys., Vol. 112, 043522 (4 pages) (2012).

We have investigated the quantum beat of the type-I heavy-hole (HH) and the type-II light-hole (LH) excitons in an In_{0.15}Ga_{0.85}As/GaAs strained single quantum well (SQW) using a reflection-type pump-probe technique. The type-II LH exciton consists of the electron and LH located in the In_{0.15}Ga_{0.85}As and GaAs layers, respectively. The energies of the type-I and the type-II excitons were evaluated with photoreflectance spectroscopy. The exciton states were calculated based on a variational method. The time-domain signals clearly show the oscillatory structure with the period corresponding to the splitting energy of the HH and the LH excitons. From the pump-energy dependence of the Fourier transform spectrum and intensity, it is concluded that the oscillation originates from the quantum beat of the type-I HH and the type-II LH excitons.

DOI: 10.1063/1.4748339

Control of Rabi Splitting Energies in CuCl Microcavities with HfO₂/SiO₂ Distributed Bragg Reflectors

M. NAKAYAMA, K. MIYAZAKI, T. KAWASE, and D. KIM

Physics Procedia, Vol. 29, pp. 6-11 (2012).

The exciton-photon interaction in CuCl microcavities with HfO₂/SiO₂ distributed Bragg reflectors has been investigated from the viewpoint of the active-layer-thickness dependence of the interaction energy, the so-called vacuum Rabi splitting energy. The active layer thickness was changed from $\lambda/32$ to $\lambda/5$, where λ corresponds to an effective resonant wavelength of the lowest-lying Z_3 exciton. We performed angle-resolved reflectance measurements, and clearly detected three cavity-polariton modes originating from the lower, middle, and upper polariton branches in a strong coupling regime of the Z_3 and $Z_{1,2}$ excitons, and cavity photon. The incidence-angle dependence of the cavity-polariton energies was analyzed with a phenomenological Hamiltonian for the strong coupling. The vacuum Rabi splitting energies are systematically controlled from 22 (37) to 68 (122) meV for the Z_3 ($Z_{1,2}$) exciton with an increase in the active layer thickness. The active-layer-thickness dependence of the Rabi splitting energy is quantitatively explained using a simple model for quantum-well microcavities.

DOI: 10.1016/j.phpro.2012.03.68

Time Evolution of Terahertz Electromagnetic Waves from Undoped GaAs/*n*-type GaAs Epitaxial Layer Structures Clarified with Use of a Time-Partitioning Fourier Transform Method

H. TAKEUCHI, S. TSURUTA, H. YAMADA, M. HATA, and M. NAKAYAMA

Physics Procedia, Vol. 29, pp. 30-35 (2012).

We have investigated the time evolution of terahertz electromagnetic waves caused by the surge current of photogenerated carriers, the so-called first burst, in two *i*-GaAs/*n*-GaAs epitaxial layer structures with different *i*-GaAs layer thicknesses of 500 and 1200 nm. The terahertz waveform of the first burst shows a narrowing with a decrease in the thickness of the *i*-GaAs layer. In accordance with the above phenomena, it is observed in the Fourier power spectra that the band of the first burst shows a high frequency shift with a decrease in the *i*-GaAs layer thickness. We elucidate the origin of the high frequency shift, focusing on the time-domain dynamics of the photogenerated carriers: we apply the time-partitioning Fourier transform, which is useful to investigate the time evolution of the frequency. From the time-partitioning Fourier power spectra, we obtain the evidence that the acceleration after the carrier generation dominates the time evolution of the frequency component leading to the high frequency shift.

DOI: 10.1016/j.phpro.2012.03.687

Exciton Polaritons in a CuBr Microcavity with HfO₂/SiO₂ Distributed Bragg Reflectors

M. NAKAYAMA, Y. KANATANI, T. KAWASE, and D. KIM

Phys Rev. B, Vol. 85, 205320 (5 pages) (2012).

We have investigated the characteristics of exciton-photon strong coupling in a CuBr bulk microcavity that consists of a CuBr active layer with an effective thickness of $\lambda/2$ and HfO₂/SiO₂ distributed Bragg reflectors: λ corresponds to an effective resonant wavelength of the lowest-lying exciton. The CuBr crystal has three excitons labeled Z_f , $Z_{1,2}$ and Z_3 at the Γ point, where the Z_f exciton originates from a triplet state, which is peculiar to CuBr. Angle-resolved reflectance spectra measured at 10 K demonstrate the strong coupling behavior of the Z_f , $Z_{1,2}$ and Z_3 excitons and cavity photon, resulting in the formation of four cavity-polariton branches. Analyzing the cavity-polariton dispersion relations based on a phenomenological Hamiltonian for the strong coupling, we evaluated the vacuum Rabi-splitting energies of the Z_f , $Z_{1,2}$ and Z_3 excitons to be 31, 108, and 84 meV, respectively. These Rabi-splitting energies reflect the magnitudes of the oscillator strengths of the relevant excitons. Furthermore, we precisely measured angle-resolved photoluminescence (PL) spectra of the lower polariton branch under a weak excitation condition. In the bottleneck region, the population of the cavity polaritons is negligible, and the PL intensity at $k=0$ is the highest. These facts suggest that the relaxation process of the cavity polaritons is not affected by a bottleneck effect.

DOI: 10.1103/PhysRevB.85.205320

Photoluminescence Properties of Self-Assembled Monolayers of CdSe and CdSe/ZnS Quantum Dots

H. YOKOTA, K. OKAZAKI, K. SHIMURA, M. NAKAYAMA, and D. KIM

J. Phys. Chem. C, Vol. 116, pp. 5456-5459 (2012).

The photoluminescence (PL) properties of self-assembled monolayers (SAMs) of CdSe and CdSe/ZnS quantum dots (QDs) were investigated. From measurements of the temperature dependence of PL spectra, it is demonstrated that the thiol group, which is a constituent of the reagent for formation of the SAM, degrades the PL properties during the SAM formation process. With an additional dipping treatment in a Cd(ClO₄)₂ aqueous solution with pH = 10, the band-edge PL intensity is increased remarkably. The improvement of PL properties is attributed to QD surface modification with a Cd(OH)₂ layer. On the other hand, the defect-related PL band is not observed at all, even at 10 K, in the SAMs of CdSe/ZnS core/shell QDs. This fact indicates that the ZnS shell layer prevents degradation of the PL properties during the SAM process.

Active-Layer-Thickness Dependence of Rabi Splitting Energies in ZnO Microcavities

T. KAWASE, D. KIM, and M. NAKAYAMA

Phys. Status Solidi C, Vol.9, pp. 1797-1800 (2012).

We have investigated the active-layer-thickness dependence of Rabi splitting energies in ZnO microcavities. We fabricated ZnO microcavities using rf magnetron sputtering for the HfO₂/SiO₂ distributed Bragg reflector and pulsed-laser deposition for the ZnO active layer. In order to control of the Rabi splitting energies, the active layer thickness was changed from $\lambda/2$ to $3\lambda/2$. In angle-resolved reflectance spectra at 10 K, the cavity polaritons resulting from the strong coupling between A, B, and C excitons peculiar to ZnO and the cavity photon were clearly detected. We estimated the energies of the exciton-photon interaction, the so-called Rabi splitting energies, from the analysis of the cavity polariton dispersions using the phenomenological Hamiltonian for the strong exciton-photon coupling. The Rabi splitting energies markedly increase with an increase in the active layer thickness. The active-layer-thickness dependence of the Rabi splitting energies are explained by a semiquantitatively analysis. Consequently, we have succeeded in the control of the Rabi splitting energies in the ZnO microcavities. DOI 10.1002/pssc.201100583

Wavelength tuning characteristics of idler waves in terahertz-wave parametric oscillator using optical double resonance

Y. TAKIDA, T. OHIRA, Y. TADOKORO, H. KUMAGAI, and S. NASHIMA

IEEJ Transactions on Electronics, Information and Systems, Vol. 132, No. 8, p.1299-p.1300 (2012). (in Japanese)

We experimentally investigated the wavelength tuning of oscillating idler (Stokes) waves by slightly translating the position of a mirror constituting an enhancement cavity in a terahertz (THz)-wave parametric oscillator (TPO) with optical double resonance. The wide tuning range of the idler wavelength was from 781.5 to 787.3 nm, corresponding to the frequency range of THz (signal) waves from 0.7 to 3.5 THz. The measured intersecting angle between pump and idler waves was in good agreement with the theoretical calculation of the noncollinear phase-matching condition in all the above tuning range.

Enhancement effect of fundamental lights with external cavity on second harmonic generation - Comparison between CW and mode-locked picosecond pulsed mode-

T. OHIRA, Y. TAKIDA, Y. TADOKORO, and H. KUMAGAI

IEEJ Transactions on Electronics, Information and Systems, Vol. 132, No. 8, p.1273-p.1277 (2012). (in Japanese)

Recently, external enhancement cavities have been employed for the improvement of the conversion efficiency in various wavelength conversions. Indeed, the external enhancement cavities are very attractive because they are constructed without any sophisticated optical configuration and therefore we have expected that they are so applicable in the enhancement of the fundamental lights as to be utilized with a variety of light sources. In this study, we demonstrated the second harmonic generations (SHGs) of both an infrared continuous wave (CW) light and a mode-locked picosecond pulsed light in a similar external enhancement cavity with the same BiB₃O₆

(BiBO). Then we confirmed the enhancement effects for both lights. The maximum output power of the CW second harmonic light was 430 mW and then the conversion efficiency was 54%. On the other hand, the maximum output power of the picosecond pulsed second harmonic light was 560 mW and then the conversion efficiency was 70%. These values are excellent results in SHG with BiBO crystal in spite of the relatively low fundamental power. From the SHG output characteristics, we performed comparison of the optimization conditions of both external enhancement cavities and the characteristics of the enhancement effects.

Coherent electro-optical detection of THz-wave generated from synchronously pumped picosecond THz parametric oscillator

Y. TAKIDA, T. OHIRA, Y. TADOKORO, H. KUMAGAI and S. NASHIMA

Proceedings of SPIE, Vol. 8240, 82400A p.1-p.6 (2012).

Terahertz (THz) radiation via parametric down-conversion of optical pulses in a nonlinear optical crystal is an attractive way to develop frequency tunable THz-wave sources. Therefore, we have focused on developing low-laser-power pumped THz-wave parametric sources and then successfully demonstrated a synchronously-pumped picosecond THz parametric oscillator (TPO) in pump-enhanced idler-resonant cavity with a bulk 5 mol% MgO-doped lithium niobate (MgO:LN) crystal. In this paper, toward coherent electro-optical (EO) detection of THz waves generated from our synchronously pumped picosecond TPO, we reported time-domain measurements of the THz electric fields using a bowtie-shaped low-temperature grown gallium arsenide (LT-GaAs) photoconductive (PC) antenna as a THz detector. As a result, we obtained temporal waveforms of the THz electric pulses, for the different number of Si-prism couplers, and then found that the radiated THz waves separated multiple unanticipated pulses by use of the arrayed-prism coupling technique. Also, we compared the time-domain system with a Fourier transform Michelson interferometer using a high resistance silicon (Si) beam splitter, from the some viewpoints. The present results reveal great prospects for the realization of THz spectroscopy and imaging applications using our THz-wave source.

Tunable terahertz parametric oscillator synchronously pumped by mode-locked picosecond Ti:sapphire laser with MgO-doped LiNbO₃

Y. TADOKORO, Y. TAKIDA, T. OHIRA, H. KUMAGAI and S. NASHIMA

Proceedings of SPIE, Vol. 8240, 82401K p.1-p.6 (2012)

A terahertz (THz) parametric oscillator (TPO), which was based on the optical parametric process, in a doubly-resonant external enhancement cavity synchronously-pumped by a mode-locked picosecond Ti:sapphire laser with the center wavelength of 780 nm and the average output power of 850 mW, was built. Our TPO cavity including four mirrors and a 5 mol% MgO-doped LiNbO₃ (MgO:LN) crystal with Si-prism couplers for the output coupling of the THz wave was designed so as to circulate both pump and idler waves in the same cavity simultaneously. Furthermore, we utilized a Hänsch-Couillaud method to stabilize the cavity. As a result, we developed an easily and continuously tunable picosecond TPO by changing the noncollinear phase-matching condition. The tunable wavelength range of the idler wave was from 782 to 787 nm, which corresponded to the THz frequency range from 1.0 to 3.4 THz according to the law of energy conservation. In addition, the measured angle between the pump and idler waves, which varied from 0.6 to 2.5 degrees, showed a good agreement with the theoretical calculation of the noncollinear phase-matching condition in all the above tuning range.

Comparative study on THz time-domain spectroscopy using 780-nm 1.3-ps laser pulses with different detections of LT-GaAs photoconductive antenna and ZnTe electro-optic sampling

Y. TADOKORO, Y. TAKIDA, H. KUMAGAI, S. NASHIMA and A. KOBAYASHI

Proceedings of SPIE, Vol. 8604 (2013) accepted

We developed a picosecond THz-TDS system with a mode-locked Ti:sapphire laser with the central wavelength of 780 nm, pulse duration of 1.3 ps. A bow-tie- or dipole-shaped PC antenna on low-temperature grown GaAs (LT-GaAs) and ZnTe were used for the PC antenna and EO sampling, respectively. As a result, the sensitivity and SNR of obtained THz-wave pulse with the bow-tie antenna were higher than any other measurement with

the dipole antenna and EO crystal. The obtained THz-wave pulses had different detection limits up to approximately 0.6, 0.9, and 1.2 THz with the bow-tie, dipole antenna, and EO crystal, respectively.

Tunable picosecond THz-wave generation based on trapezoidal MgO:LiNbO₃ crystal in novel pentagram-shaped pump-enhancement cavity.

Y. TAKIDA, Y. TADOKORO, H. KUMAGAI, S. NASHIMA and A. KOBAYASHI

Proceedings of SPIE, Vol. 8604 (2013) accepted

We have succeeded in developing a tunable picosecond THz-wave source by using a surface-emitted configuration which consists of a trapezoidal MgO-doped LiNbO₃ (MgO:LiNbO₃) crystal and a pump-enhancement cavity folded in the shape of a pentagram. By slightly translating the position of one of the cavity mirrors, we experimentally find that the THz-wave peak frequency is tunable in the range from 0.9 to 3.5 THz with the average output power of dozens of nanowatts. The maximum THz-wave average power is up to 40 nW around 2 THz at the pump power of 800 mW, which is several times higher than the THz-wave output generated by using rectangular MgO:LiNbO₃ crystals for Si-prism-coupled configuration under the same pump condition.

Fabrication of a rotary optical delay stage for rapid-scanning time-domain spectroscopy system between terahertz and the mid-infrared region

S. NASHIMA, H. NAKAMINE, and M. HOSODA

J. Jpn. Soc. Infrared Science & Technology, Vol.22, No.2, (2012), in press. (in Japanese)

We have customized a rotary optical delay stage for a rapid scanning time domain spectroscopy system between terahertz and the mid-infrared region. It measured a temporary electromagnetic wave, which enabled detection of electromagnetic wave in 118-ps temporal range under 0.17-s measurement time. A typical signal to noise ratio of 1.5×10^3 was achieved within 150 sec, which is 1.8 times greater than that obtained by a standard lock-in detection based on stepper motor optical delay stage. The accuracy of Fourier transform amplitude spectrum is increased 4.8 times compared to that for lock-in based detection.

Quantitative analysis on mixed organic solution using terahertz time domain spectroscopy

S. NASHIMA, R. NISHIMURA, and M. HOSODA

International Symposium on Terahertz Nanoscience (TeraNano 2011), Workshop of International Terahertz Research Network (GDR-I), November, 2011, Osaka, Japan

The effective dielectric permittivity of mixed organic solution was measured by terahertz time domain spectroscopy (THz-TDS). The experimentally obtained effective dielectric permittivity of hexane/toluene mixed organic solution was compared with that calculated using the effective medium approximation (EMA) model. This model accurately fits the complex dielectric permittivity from 0.5 to 3.0 THz. The mixing ratio inference obtained by the THz-TDS measurement agrees well with that obtained using the mass analysis.

Quantitative analysis on toluene contents in hexane solution using terahertz time domain spectroscopy

S. NASHIMA, R. NISHIMURA, and M. HOSODA

37th International Conference on Infrared, Millimeter and Terahertz Waves (IRMMW-THz2012), Sep. 2012, Wollongong, Australia.

The effective dielectric permittivity of a mixed organic solution was measured by terahertz time domain spectroscopy (THz-TDS). The experimentally obtained effective dielectric permittivity of hexane/toluene mixed organic solution was well fitted by the effective medium approximation (EMA) model. Discrepancy between experimental results and calculations from 0.5 to 3.0 THz is estimated to be 0.28%.

Parametric generation of terahertz-wave in picosecond enhancement cavity (I)

— **Details of terahertz-wave generation** —

Y. TAKIDA, H. KUMAGAI, S. MAEDA, T. OHIRA, and S. NASHIMA

J. Jpn. Soc. Infrared Science & Technology, Vol.21, No.2, pp. 75-79 (2012) (in Japanese)

Terahertz (THz)-wave parametric sources via stimulated Raman scattering in lithium niobate (LiNbO_3) crystal are able to generate widely frequency-tunable THz-waves at room temperature. We have successfully demonstrated a doubly-resonant THz-wave parametric oscillation in picosecond enhancement cavity using the noncollinear phase-matching geometry in a 5 mol% MgO-doped LiNbO_3 crystal. In this paper, we focus on details of the property of THz-wave generation. With the enhancement cavity which consisted of four mirrors, we achieved 50 MW/cm^2 of lower generation threshold of THz-wave than other conventional externally-pumped THz-wave parametric oscillators. Furthermore, we obtained the wavelength tunability of idler (Stokes) wave from approximately 781.5 to 786.0 nm, which corresponds to the frequency range of THz-wave from 0.7 to 3.0 THz.

Parametric generation of terahertz-wave in picosecond enhancement cavity (II)

— Evaluation of enhancement cavity —

H. KUMAGAI, Y. TAKIDA, S. MAEDA, T. OHIRA, and S. NASHIMA

J. Jpn. Soc. Infrared Science & Technology, Vol.21, No.2, pp. 80-84 (2012) (in Japanese)

The previous paper reported that a pumping threshold of THz-wave parametric oscillation of 50 MW/cm^2 was demonstrated with the picosecond enhancement cavity which consisted of four mirrors and then that it was much lower than those of other conventional externally-pumped THz-wave parametric oscillators. The novel quasi-CW enhancement cavity where the simultaneous enhancements for both pump and idler (Stokes) waves was realized with the lower threshold of THz-wave parametric oscillation, was evaluated here in comparison with that of the CW through SHG experiments where evaluation results regarding optical enhancements in similar cavities existed.

Tunable Picosecond Terahertz-Wave Parametric Oscillators Based on Noncollinear Pump-Enhanced Idler-Resonant Cavity

Y. TAKIDA, T. OHIRA, Y. TADOKORO, H. KUMAGAI, and S. NASHIMA

Journal of Selected Topics in Quantum Electronics, in press.

We have succeeded in developing tunable picosecond terahertz (THz)-wave parametric oscillators (ps-TPOs) by employing a noncollinear pump-enhanced idler-resonant cavity. As a parametric gain medium, we use two different shapes of unpoled, 5 mol% MgO-doped lithium niobate ($\text{MgO}:\text{LiNbO}_3$) crystal: (1) a rectangle for Si-prism output-coupler technique; and (2) a trapezoid for surface-emitted configuration. Unlike conventional nanosecond TPOs (ns-TPOs), these ps-TPOs are synchronously pumped by a mode-locked 1.5-ps Ti:sapphire laser operating at 780 nm. To overcome the high pump threshold due to the strong absorption by $\text{MgO}:\text{LiNbO}_3$ in the THz region, we employ a pump-enhanced cavity which is carefully designed for the noncollinear double resonance of both pump and idler waves. By slightly translating the position of one of the ps-TPO cavity mirrors, we experimentally find that the THz-wave frequency is continuously tunable from 1.0 to 3.2 THz with the average output power of several nanowatts. In all the above tuning range, especially above 2 THz, the THz-wave output of the surface-emitting ps-TPO using the trapezoidal $\text{MgO}:\text{LiNbO}_3$ crystal is enhanced several times more than that of the Si-prism-coupled ps-TPO using the rectangular $\text{MgO}:\text{LiNbO}_3$ crystal due to the suppression of the absorption loss in $\text{MgO}:\text{LiNbO}_3$.

Coherent electro-optical detection of THz-wave generated from synchronously pumped picosecond THz parametric oscillator

Y. TAKIDA, T. OHIRA, Y. TADOKORO, H. KUMAGAI, and S. NASHIMA

SPIE Photonics West 2012, Jan., 2012, San Francisco, USA

Terahertz (THz) radiation via parametric down-conversion of optical pulses in a nonlinear optical crystal is an attractive way to develop frequency tunable THz-wave sources. Therefore, we have focused on developing low-laser-power pumped THz-wave parametric sources and then successfully demonstrated a synchronously-pumped picosecond THz parametric oscillator (TPO) in pump-enhanced idler-resonant cavity with a bulk 5 mol% MgO-doped lithium niobate ($\text{MgO}:\text{LN}$) crystal. In this paper, toward coherent electro-optical (EO) detection of THz waves generated from our synchronously pumped picosecond TPO, we reported time-domain measurements of

the THz electric fields using a bowtie-shaped low-temperature grown gallium arsenide (LT-GaAs) photoconductive (PC) antenna as a THz detector. As a result, we obtained temporal waveforms of the THz electric pulses, for the different number of Si-prism couplers, and then found that the radiated THz waves separated multiple unanticipated pulses by use of the arrayed-prism coupling technique. Also, we compared the time-domain system with a Fourier transform Michelson interferometer using a high resistance silicon (Si) beam splitter, from the some viewpoints. The present results reveal great prospects for the realization of THz spectroscopy and imaging applications using our THz-wave source.

Tunable terahertz parametric oscillator synchronously pumped by mode-locked picosecond Ti:Sapphire laser with MgO-doped LiNbO₃

Y. TADOKORO, Y. TAKIDA, T. OHIRA, H. KUMAGAI, and S. NASHIMA

SPIE Photonics West 2012, Jan., 2012, San Francisco, USA

A terahertz (THz) parametric oscillator (TPO), which was based on the optical parametric process, in a doubly-resonant external enhancement cavity synchronously-pumped by a mode-locked picosecond Ti:sapphire laser with the center wavelength of 780 nm and the average output power of 850 mW, was built. Our TPO cavity including four mirrors and a 5 mol% MgO-doped LiNbO₃ (MgO:LN) crystal with Si-prism couplers for the output coupling of the THz wave was designed so as to circulate both pump and idler waves in the same cavity simultaneously. Furthermore, we utilized a Hänsch-Couillaud method to stabilize the cavity. As a result, we developed an easily and continuously tunable picosecond TPO by changing the noncollinear phase-matching condition. The tunable wavelength range of the idler wave was from 782 to 787 nm, which corresponded to the THz frequency range from 1.0 to 3.4 THz according to the law of energy conservation. In addition, the measured angle between the pump and idler waves, which varied from 0.6 to 2.5 degrees, showed a good agreement with the theoretical calculation of the noncollinear phase-matching condition in all the above tuning range.

Multimode Peierls distortion in triangular lattice

K. MIYOSHI and A. TERAJ

Phys. Status Solidi B **249**, pp. 967-970 (2012).

We have studied the multimode Peierls states in the electron-lattice system on a triangular lattice with a three-quarter-filled electronic band. Below the transition temperature, we have found many stable states of nearly same free-energy. Focusing our attention on the lowest free-energy state, we have found that the Peierls order parameter continuously increases from zero just below the transition temperature. When the temperature is raised from the region lower than the critical temperature, multiple phonon modes are simultaneously softened at the same temperature as when the temperature is lowered from the region higher than the critical temperature. These results tell us that the transition is of the second order. The non-softened modes are also found to condense due to nonlinear coupling between the non-softened modes and the softened modes. The degeneracy of the phonon modes observed at the higher temperature region is partially lifted at the lower temperature region. DOI 10.1002/pssb.201100745

Electron correlation effects on multimode Peierls distortion in the two-dimensional electron-lattice system

Y. MATSUMOTO and A. TERAJ

Phys. Status Solidi C **9**, pp. 1183-1185 (2012).

The electron correlation effects on the multimode Peierls (MMP) state in the Peierls Hubbard model on the two-dimensional square lattice with the half-filled electronic band is investigated, taking account of the on-site interaction (U) and the nearest neighbor interaction (V), by using the variational Monte Carlo method based on the Gutzwiller wave function. The Peierls distortion amplitude is enhanced as U is increased, showing the first-order phase transition from the MMP state to the antiferromagnetic state. The Peierls distortion amplitude is also enhanced by V . The first-order phase transition from the MMP state to the charge-ordered state occurs at a critical value of V . There is no coexistence of the Peierls distortion and the charge order. DOI: 10.1002/pssc.201100664

Microscopic reversibility of quantum open systems

T. MONNAI

J.Phys.A, 45 125001 (2012)

The transition probability of an isolated system for a time-dependent unitary evolution is invariant under the reversal of protocols. In this paper, we generalize the expression of microscopic reversibility to externally perturbed large quantum open systems, which provides a model-independent equality between time forward and reversed joint transition probabilities. A time-dependent external perturbation acts on the subsystem during a transient duration, and subsequently the perturbation is switched off so that the total system would thermalize. We concern ourselves with the net transition probability for the subsystem from the initial to final states after a time evolution during which the energy is irreversibly exchanged between the subsystem and reservoir. The time-reversed probability is given by the reversal of the forcing protocol and the initial ensemble. Microscopic reversibility equates the time forward and reversed probabilities, and therefore appears as a thermodynamic symmetry for open quantum systems.

Stranski-Krastanow growth of copper overlayers on the Ni(110) surface

Tsuneo FUKUDA, Kenji UMEZAWA (Osaka Prefecture University), and Hiroshi NAKAYAMA

Surface Science Vol. 606, pp. 1221-1226 (2012).

Cu overlayer formation on the Ni(110) surface was studied using scanning tunneling microscopy (STM) in an ultrahigh vacuum. Room-temperature deposition of Cu onto a Ni(110) surface exhibited layer-by-layer growth up to 6 monolayers (MLs), followed by three-dimensional island formation, i.e., the Cu overlayer growth on the Ni(110) surface is classified as Stranski-Krastanow growth. At the initial growth stage, anisotropic two-dimensional islands were elongated in the close-packed $[1\bar{1}0]$ direction. The nucleation of the second layer was strongly affected by the morphology of the first layer, and the second-layer islands also extended in the $[1\bar{1}0]$ direction. The third and further layers grew two-dimensionally. Detailed STM images showed mosaic features due to Cu and Ni alloying. Three-dimensional islands were observed for Cu deposition beyond 6 ML. The (110)-oriented top surface of the islands had stripes along the $[001]$ direction. In addition, bumps extending in the $[1\bar{1}0]$ direction were formed on these island surfaces, indicating threading dislocation through the island to relieve the compressive stress of the overlayers. An atomic model of the bump compatible with the STM image was proposed.

Multi-Color See-Through Retinal Projection Head-Mounted Display

Katsushi TAKAICHI and Hideya TAKAHASHI

ICIC Express Letters, Vol.6, 5, pp.1291-1296 (2012).

We developed a multi-color see-through retinal projection head-mounted display (HMD). Its notable features are the extremely deep focal length and the high contrast image by using the principle of the Maxwellian view. It consists of an image projection optics system and a holographic optical element (HOE). The HOE is used as a combiner that superimposes the virtual image on the real scene to realize a function of the see-through. The HOE also works as a condenser lens to achieve the Maxwellian view. See-through HMDs provide an effective capability for Mixed Reality tools such as a personal mobile information display. In this application, since the capability to display color images is important, the HOE can be reconstructed by some primary colors. This paper describes the principle of the proposed multi-color see-through retinal projection HMD and also describes the experimental results.

Wide-Viewing Angle Three-Dimensional Display Based on the Ray Reconstruction Method Using Multiple Micro-Projectors

Hideya TAKAHASHI, Kenta HIROOKA, and Kenji YAMADA (Osaka University)

Proc.SPIE-IS&T Electronic Imaging, Vol.8288, pp. 828824-828824-6 (2012).

We propose an omnidirectional three-dimensional (3D) display system. This is a tool for communication around a 3D image among a small number of people. This 3D display system consists of multiple basic 3D display units. The basic unit consists of a micro-projector, a lenticular lens array sheet, and a cylindrical lens. In this basic unit, since a screen is not used, the light rays from a micro-projector pass through a lenticular lens array sheet and observed directly. Thus, the spatial density distribution of projected light rays is partial. To average the spatial density of projected light rays, we use a cylindrical lens. To increase the viewing angle, we aligned multiple basic units in a circle, and displayed 3D images at the center of the circle. To verify the effectiveness of the proposed 3D display, we constructed the prototype system. This prototype consists of 8 basic units. They are aligned 18-degree apart in a circle and the radius is 95 mm. The maximum size of displayed 3D images is 35 mm x 40 mm x 35 mm. The viewing angle of a 3D image is 124-degree. This paper describes the principle of proposed 3D display system, and also describes the experimental results.

Extending Cycle Life of Lithium-Ion Batteries Consisting of Lithium Insertion Electrodes: Cycle Efficiency Versus Ah-Efficiency

Kensuke NAKURA, Yuta OHSUGI, Mitsuyasu IMAZAKI, Kingo ARIYOSHI, Tsutomu OHZUKU
J. Electrochem. Soc., **158**, A1243-A1249 (2011).

Capacity fading of the cell consisting of lithium titanium oxide (LTO; $\text{Li}[\text{Li}_{1/3}\text{Ti}_{5/3}]\text{O}_4$) and lithium aluminum manganese oxide (LAMO; $\text{Li}[\text{Li}_{0.1}\text{Al}_{0.1}\text{Mn}_{1.8}]\text{O}_4$) is examined in a three-electrode configuration at 55°C. Capacity fading observed during 400 cycles at 55°C is explained in terms of the state of charge (SOC) of the LTO-negative and LAMO-positive electrodes. At the discharge-end voltage of 0 V for the LTO/LAMO cell, the SOC of LTO is always 0% although LAMO is expected to be 0% in its SOC from the basic research results on Ah-efficiency obtained in Li/LTO and Li/LAMO cells. In order to understand the anomalous capacity fading, the LTO/LTO and LAMO/LAMO cells are fabricated and examined at 55°C, and the current due to the side reactions at the LTO and LAMO electrodes is determined. The current at the LTO electrode is much larger than that at the LAMO electrode, which is in reverse order in our common understanding on LTO and LAMO in non-aqueous lithium cells. From these results, extending cycle life is discussed in terms of the cycle efficiency versus Ah-efficiency. Difficulties to describe cell chemistry underlying the capacity fading are also discussed.

Potentiostat for Electrochemical Measurements

Kingo ARIYOSHI
Electrochemistry, **80**, 602-607 (2012) (in Japanese)

Epitaxial Crystal Growth and Solid-State Polymerization of Piperonyl Muconate on the {001} Surface of KCl Crystal for Controlling Polymer Chain Alignment

Katsuya ONODERA, Chiaki TANIOKU, and Akikazu MATSUMOTO
ACS Applied Materials & Interfaces, **4**(4), 2280-2287 (2012)

The authors studied the crystal growth of piperonyl (*E,E*)-muconate [bis(3,4-methylenedioxybenzyl) (*E,E*)-muconate, MDO] on inorganic crystalline substrates during vapor deposition for the control of polymer chain alignment by the subsequent solid-state photopolymerization of the MDO monomer thin films deposited on the substrate. The authors controlled the arrangement of the MDO molecules and the polymer chains produced on the substrate, depending on the lattice parameters of the substrate surfaces used. The epitaxial crystal growth of MDO on the {001} plane of a KCl single crystal was observed under the condition that the crystal lattice lengths of MDO agreed with the specific space distance of the substrate; i.e., the KCl cubic crystal resulted in a d_{110} value of 4.45 Å, which was very close to the value of the monomer stacking distance in the MDO crystal ($d_s = 4.43$ Å). However, slightly large and too small d_{110} values for KBr and NaCl, respectively, resulted in the less controlled and no epitaxial crystal growth of MDO. The irradiation of polarized UV light on the MDO thin-film crystal produced highly regulated polymer alignment in a specific direction on the KCl substrate.

Pressure-Sensitive Adhesion System Using Acrylate Block Copolymers in Response to Photoirradiation and Postbaking as the Dual External Stimuli for On-Demand Dismantling

Tadashi INUI, Eriko SATO, and Akikazu MATSUMOTO
ACS Applied Materials & Interfaces, **4**(4), 2124-2132 (2012)

We have demonstrated the validity of a new type of pressure-sensitive adhesion system using block copolymers containing a poly(2-ethylhexyl acrylate) (P2EHA) segment as the low glass transition temperature polymer and a poly(*tert*-Bu acrylate) (PtBA) or poly(isobornyl acrylate) (PIBoA) segment as the reacting polymer in the presence of a photoacid generator (PAG). This adhesion system can be easily debonded because of a change in the polymer properties of the adhesives by acid-catalyzed deprotection uniquely occurring during the photoirradiation followed by postbaking. We investigated the transformation of PtBA and PIBoA into poly(acrylic acid) using IR spectroscopy and a thermogravimetric analysis in the presence of *p*-toluenesulfonic acid and the PAGs. The block copolymers with a well-defined molecular structure were then synthesized by atom transfer radical polymerization, and their adhesive properties were evaluated using the 180° peel test. The block copolymers showed superior adhesion property than a random copolymer and polymer blends, due to the microphase separation of the block copolymers. A drastic change

in the adhesive strength of the block copolymers was observed in response to the dual external stimuli consisting of UV irradiation and the subsequent heating.

Facile Synthesis of Main-Chain Degradable Block Copolymers for Performance Enhanced Dismantlable Adhesion

Eriko SATO, Takashi HAGIHARA, and Akikazu MATSUMOTO

ACS Applied Materials & Interfaces, **4**(4), 2057-2064 (2012)

Block copolymers consisting of readily degradable polyperoxides and non-degradable vinyl polymers as the block segments were successfully synthesized by reversible chain transfer catalyzed polymerization, which is one of living radical polymerization techniques. The block copolymers showed characteristic morphology and wettability being different from the polymer blends. When block copolymers containing polyperoxide and polymethacrylate blocks were heated below 150 °C, the polyperoxide blocks were completely degraded and the polymethacrylate blocks were recovered without degradation. Block copolymers containing a poly(2-ethylhexyl methacrylate) block were then investigated as a dismantlable adhesion material, which requires adequate bonding strength during use and easy debonding on demand. Among the several block copolymers, the one consisting of poly(2-ethylhexyl methacrylate) and polyperoxide from Me sorbate (PPMS) ($M_n = 4900$) exhibited good performance as a pressure-sensitive adhesive (PSA). After heating the test specimens in a temperature range from 60 to 100 °C, PSA performance, which was evaluated by 180° peel strength and shear holding power measurements, was significantly diminished. Especially, after heating at 100 °C for 1 h, spontaneous debonding of some test specimens was observed because of the evolution of volatile acetaldehyde from PPMS.

Thermally Stable Polysulfones Obtained by Regiospecific Radical Copolymerization of Various Acyclic and Cyclic 1,3-Diene Monomers with Sulfur Dioxide and Subsequent Hydrogenation

Naruki TANAKA; Eriko SATO, and Akikazu MATSUMOTO

Macromolecules, **44**(23), 9125-9137 (2011)

We synthesized the thermally stable alternating copolymers from various acyclic and cyclic alkyl-substituted 1,3-diene monomers with sulfur dioxide (SO₂) as the starting comonomers by radical copolymerization and subsequent hydrogenation. It was revealed based on the DFT calculation results using model reactions as well as the thermodynamic analysis of polymerization that some propagation steps were reversible and the highly 1,4-regiospecific sequences of the poly(diene sulfone)s (PDSs) were consequently produced via a free radical propagation mechanism. The stereochemical structures of the PDSs obtained from cyclic 1,3-diene monomers, such as 1,3-cyclopentadiene and 1,3-cyclohexadiene, were also established. based on the DFT calculations. Transparent films with a refractive index of 1.53-1.55 were readily obtained by casting the PDS solutions, being confirmed to be amorphous by wide-angle X-ray diffraction measurements. The decomposition of the PDSs started below 150 °C, but hydrogenation produced thermally stable polymers, of which the onset temperatures of decomposition were higher than 280 °C. The hydrogenation conversion significantly depended on the position of an alkyl substituent on the polymer main chain. A ternary copolymerization system consisting of both cyclic and acyclic diene monomers with SO₂ was carried out in order to simultaneously modify the thermal properties as well as the solubility of the resulting polymers.

Functional Materials Designed by Using Reactive Polymers

Eriko SATO, Akikazu MATSUMOTO

Coating Technology, **47**(9), 309-319 (2012) (in Japanese)

There has been considerable interest in the application of reactive polymers including degradable polymers to functional materials which irreversibly or reversibly change their properties. Among various reactive polymers, block copolymers containing a reactive polymer block and network polymers having cleavable cross-linking points or degradable chains are one of the attractive polymeric materials which exhibit large property changes. The strategy and design of functional materials using the reactive polymers will be reviewed with a focus on our current investigations.

Development of Dismantlable Adhesion Materials Using Acrylic Block Copolymers

Akikazu MATSUMOTO, Eriko SATO

In *Kobunshi No Kakyo To Bunkai III (Cross-linking and Degradation of Polymers III)*, Edited by Masahiro

TSUNOOKA, Masamitsu SHIRAI, CMC, pp. 210-216 (2012) (in Japanese)

Report from the 57th Polymer Research Symposium (Kobe)

Akikazu MATSUMOTO

Kobunshi (High Polymers, Japan), **60**(10), 762 (2011) (in Japanese)

Report on the 4th Asian Conference on Adhesion (ACA)

Akikazu MATSUMOTO

Journal of the Adhesion Society of Japan, **48**(2), 81-82 (2012) (in Japanese)

Dismantlable Adhesion Using Acrylic Block Copolymers for On-Demand Debonding (Hot Topics)

Akikazu MATSUMOTO

Kobunshi (High Polymers, Japan), **61**(2), 53 (2012)

Control of Interface Structure and Properties Using Reversibly Cross-linkable Polymers (Hot Topics)

Eriko SATO

Kobunshi (High Polymers, Japan), **61**(4), 180 (2012)

Development of Dismantlable Adhesion Materials Responsible to Dual Stimuli

Akikazu MATSUMOTO

The 124th Regular Meeting of Workshop on Pressure-Sensitive Adhesion, The Adhesion Society of Japan, Invited Lecture, Osaka, January 13, 2012 (in Japanese)

Synthesis of High Performance and Functional Polymers by Radical Polymerization: Crystalline Polymers and Degradable Polymers

Akikazu MATSUMOTO

The 308th Monthly Meeting of the Rubber Technology Forum, Invited Lecture, Osaka, February 15, 2012 (in Japanese)

Dismantlable Adhesion Materials Response to Dual Stimuli Using Photoacid Generators

Akikazu MATSUMOTO

The 192nd Meeting of the Photopolymer Forum, Invited Lecture, Tokyo, June 13, 2012, Preprints, pp. II 1-5 (in Japanese)

Polymer Materials Design by Radical Polymerization: Present, Past, and Future

Akikazu MATSUMOTO

The 57th Polymer Summer School of the Society of Polymer Science, Japan, Invited Lecture, Otsu, July 17-19, 2012, Abstracts, pp. 35-38 (in Japanese)

Polymer Materials Design by Radical Polymerization: Are the Reactions First? Otherwise, the Materials?

Akikazu MATSUMOTO

The 78th Workshop on Polymers for Young Researchers in Kansai, Kansai Branch of the Society of Polymer Science, Japan, Invited Lecture, Kobe, July 28-29, 2012, Abstracts, pp. 7-20 (in Japanese)

Solid-State Reactions of Organic Crystals under UV, X-ray, and γ -ray Irradiations: Reaction Control and Materials Design

Akikazu MATSUMOTO

The 51st UV/EB Workshop of Osaka Nuclear Science Association (ONSA), Invited Lecture, Osaka, August 10, 2012, Abstracts, pp. 10-17 (in Japanese)

Designing of Functional Materials Using Reactive Polymers

Eriko SATO

The 11th Workshop of Polymer Materials of Chugoku-Shikoku Branch of the Society of Polymer Science,

Japan, Invited Lecture, Tokushima, November 4, 2011 (in Japanese)

Photoreactions of Polymer Thin Films and Reversible Transformation of Their Properties

Eriko SATO

The Regular Meeting of Kansai Hybrid and Interface, Kansai Branch of the Adhesion Society of Japan, Invited Lecture, Osaka, July 31, 2012 (in Japanese)

Micro-X-ray Fluorescence (book chapter)

Kouichi TSUJI

In *Encyclopedia of Analytical Chemistry, Supplementary vol. S1-S3*, eds. R.A. Meyers, John Wiley & Sons, Ltd. Chichester, UK, pp.1949-1972 (2011).

Development of 3D-XRF method for inside analysis of solid materials, - top performance in the world- (book chapter)

Kouichi Tsuji

In *Keywords for Success of Industry-University Cooperative Study*, Maruzen, (2011) 271-282. (in Japanese)

Dictionary of Technical Terms in Analytical Chemistry (book)

(Technical terms related to X-ray analysis were written by Tsuji)

Kouichi Tsuji

In *Dictionary of Technical Terms in Analytical Chemistry*, Ohmsha, (2011) 1-451. (in Japanese)

Development of a New Confocal 3D-XRF Instrument with an X-ray Tube

Kouichi TSUJI and Kazuhiko NAKANO

J. Anal. At. Spectrom., Vol. 26, pp. 305-309 (2011)

A new 3D-XRF instrument was developed with a fine-focus X-ray tube. The depth resolution of the developed instrument was 13.7 mm at the energy of Au L β (11.4 keV). Compared with the previous 3D-XRF instrument developed in the author's research group, the depth resolution was improved by a factor of 3–4. A small dependence of depth resolution on X-ray energy was also confirmed for the new instrument. The depth resolution was varied from 22.6 mm to 13.7 mm for an energy range from 5.4 keV to 11.4 keV, respectively. A few layered materials were measured by two (previous and new) 3D-XRF instruments. As expected, the new 3D-XRF instrument gave a depth profile with a high-resolution. In addition, a 3D-structured material was proposed and developed to evaluate the 3D-imaging performance. The material consisted of two cylindrical patterns of Au having a micrometre-scale structure. Elemental imaging performance was compared by using this 3D-structured material for two different 3D-XRF instruments.

Depth Elemental Imaging of Forensic Samples by Confocal micro-XRF Method

Kazuhiko NAKANO, Chihiro NISHI, Kazunori OTSUKI, Yoshinori NISHIWAKI, and Kouichi TSUJI

Anal. Chem., Vol. 83, pp.3477-3483 (2011).

Micro-XRF is a significant tool for the analysis of small regions. A micro-X-ray beam can be created in the laboratory by various focusing X-ray optics. Previously, nondestructive 3D-XRF analysis had not been easy because of the high penetration of fluorescent X-rays emitted into the sample. A recently developed confocal micro-XRF technique combined with polycapillary X-ray lenses enables depth-selective analysis. In this paper, we applied a new tabletop confocal micro-XRF system to analyze several forensic samples, that is, multilayered automotive paint fragments and leather samples, for use in the criminalistics. Elemental depth profiles and mapping images of forensic samples were successfully obtained by the confocal micro-XRF technique. Multilayered structures can be distinguished in forensic samples by their elemental depth profiles. However, it was found that some leather sheets exhibited heterogeneous distribution. To confirm the validity, the result of a conventional micro-XRF of the cross section was compared with that of the confocal micro-XRF. The results obtained by the confocal micro-XRF system were in approximate agreement with those obtained by the conventional micro-XRF. Elemental depth imaging was performed on the paint fragments and leather sheets to confirm the homogeneity of the respective layers of the sample. The depth images of the paint fragment showed homogeneous distribution in each layer except for Fe and Zn. In contrast, several components in the leather sheets were predominantly localized.

Wavelength Dispersive X-ray Fluorescence Imaging

Kouichi TSUJI, Takashi OHMORI, and Makoto YAMAGUCHI

Anal. Chem., Vol. 83, pp.6389-6394 (2011).

A new wavelength-dispersive X-ray fluorescence (WD-XRF) imaging spectrometer equipped with a two-dimensional X-ray detector was developed in the laboratory. Straight polycapillary optics was applied instead of a soller slit, which is used in conventional WD-XRF spectrometers. X-rays were guided through the straight polycapillary to the exit of the optics by X-ray external total reflections. X-ray fluorescence was dispersed by an analyzing crystal (LiF(200)), keeping the information of elemental distribution on the surface of the sample. The energy resolution of the developed spectrometer was 130-152 eV at the Zn KR peak. X-ray elemental images of Cu KR and Ni KR were successfully obtained by an X-ray CCD detector at the corresponding diffraction angles. The analytical performance of this technique, and further improvements are discussed.

Enhancement of XRF Intensity by Using Au Coated Glass-Capillary

Takashi NAKAZAWA, Kazuhiko NAKANO, Masaru YOSHIDA, and Kouichi TSUJI

Advances in X-ray Analysis, Vol. 54, pp. 238-246 (2011).

Enhancement of XRF intensity was investigated by using an Au coated glass-capillary. Au was electroplated on an inner wall of the glass-capillary with a thickness of 100 nm. The Au coated glass-capillary was attached to a micro focus x-ray tube. The XRF intensity from the pure metal samples was measured by a silicon drift x-ray detector. It was confirmed that the intensity of XRF was enhanced by using Au coated glass-capillary by factors of 1.1 to 1.5 times. The XRF intensity profile was also measured by wire scanning method to investigate the reason. The trace of primary x-ray beams was calculated considering x-ray total reflection. The calculated results of agreed well with the experimental XRF intensity profile. The reason of enhancement XRF intensity was that the primary x-rays were totally reflected on the inner wall of glass-capillary.

Enhancement of XRF Intensity by Using Au-Coated Glass Monocapillary

Takashi NAKAZAWA, Kazuhiko NAKANO, Masaru YOSHIDA, and Kouichi TSUJI

Powder Diffraction, Vol. 26, pp.163-167 (2011).

Results on using X-ray optics with a monocapillary attached to a microfocus Mo X-ray tube for a high-intensity XRF analysis are reported. Au-coated glass monocapillaries with 400 and 700 μm inner diameters were used to obtain focused and intensive incident Mo X-rays for the measurements of XRF intensities from pure metal samples. Intensity enhancements obtained by using the Au-coated monocapillaries were found to be up to 1.5 times higher than those obtained by using similar inner diameter uncoated glass capillaries. The XRF intensity profiles were measured by the wire scanning method to investigate the reasons. The traces of the incident X-rays were calculated by taking into account of X-ray total reflection of the incident X-rays from the inner wall of the capillaries. The calculated XRF intensity profiles agree with those of the measured XRF intensity profiles. The observed enhancements in XRF intensity were the results of the incident X-rays emitted from the Mo X-ray tube being totally reflected on the inner wall of the Au-coated monocapillaries.

Surface and Interface Analysis by X-ray Fluorescence (review article)

Kouichi TSUJI

Journal of the Adhesion Society of Japan, Vol. 47, pp.444-452 (2011) (in Japanese).

Micro XRF Analysis and Elemental Imaging (review article)

Takashi NAKAZAWA, Kazuhiko NAKANO, and Kouichi TSUJI

Bunseki, 11, pp. 654-661 (2011) (in Japanese).

Solvothermal Synthesis of ITO Nanoparticles and their Application to the Transparent Conductive Film

Noritsugu KOMETANI and Masaya FUJII

The Review of High Pressure Science & Technology, Vol.22, No.2, pp.129-134 (2012).

Indium tin oxide (ITO) nanoparticles have been synthesized from the mixed ethylene glycol solution of indium(III) chloride, tin(II) chloride and sodium hydroxide by the solvothermal process with the addition of oleylamine or oleic acid as a protective reagent. The x-ray diffraction patterns of particles synthesized at 250°C show that the ITO begins to be produced after the reaction duration of 6 h when oleylamine is added to the reaction solution, indicating a promoting effect on the ITO formation, whereas only indium oxyhydroxide is formed when oleic acid is used. The transmission electron microscopic observation has revealed that ITO nanoparticles obtained by the addition of oleylamine are monodisperse and their size increases from 4–5 nm to 50–60 nm with elongating reaction duration from 6 to 96 h. ITO thin films are prepared by the multiple deposition of a collodion membrane incorporating synthesized ITO nanoparticles on the glass substrate followed by sinter at 400–500°C. They exhibit a good transparency in the visible region and a specific resistivity as low as 1.0 Ω·cm.

Hydrothermal Synthesis of Metal Nanoparticles

Noritsugu KOMETANI

Jasco Report Special Issue of Supercritical Fluids, Vol.11, pp.11-16 (2012).

This paper reviews the recent results of our studies on the hydrothermal synthesis of metal nanoparticles using the flow-type reactor system. The formation mechanism of silver nanoparticles under the hydrothermal conditions has been examined by in-situ monitoring of the absorption spectra of reaction solutions in the high-temperature high-pressure reactor. It is found that the silver nanoparticle is partially dissolved in subcritical water at 350°C, resulting in the bimodal size distribution of obtained nanoparticles. The hydrothermal reactor having a T-shaped junction has been developed for the purpose of the preparation of size-controlled metal nanoparticles. The results indicated that ultrafine silver nanoparticles with narrower size distribution can be obtained using this reactor system because of the rapid mixing of reaction solutions at the T-shaped junction. The hydrothermal synthesis of copper nanoparticles has also been demonstrated, suggesting that this method has broad utility for various types of metal nanoparticles.

Photochromic Polymers Bearing Various Diarylethene Chromophores as the Pendant: Synthesis, Optical Properties, and Multicolor Photochromism

Hiroyasu NISHI, Tomoko NAMARI, and Seiya KOBATAKE

J. Mater. Chem., Vol. 21(43), pp. 17249–17258 (2011).

Photochromic polymers with various diarylethene derivatives were synthesized by a conventional radical polymerization of styrene derivatives having diarylethene chromophores as the pendant. All the polymers exhibited reversible photochromism in the film as well as in solution, while the photocyclization conversion in the film decreased in comparison with that in solution because of a restriction of the conformational structure in the solid state. Although the photocyclization and photocycloreversion quantum yields at the initial stage of the reactions in the film were comparable to those in solution, the apparent cycloreversion quantum yield decreased along with the reaction, which is derived from a distribution of the quantum yields in the solid state. Finally, the photochromic terpolymers consisting of three diarylethene monomers which show photochromism changing color to cyan, magenta, and yellow were synthesized. The terpolymers were demonstrated to show bright colors including black, green, red, and blue both in solution and in the solid state by selective bleaching processes. Such multicolor photochromic polymers composed of diarylethene derivatives have a potential for rewritable photochromic display devices.

Facile Preparation of Gold Nanoparticle with Diarylethene Polymers by Disodium Malate and Its Photoreversible Optical Properties

Hiroyasu NISHI and Seiya KOBATAKE

Dyes and Pigments, Vol. 92(2), pp. 847–853 (2012).

We have developed a synthetic procedure of gold nanoparticle covered with polystyrene (Au-poly(St)) using organic acid salts, followed by a ligand exchange reaction. First, various chain lengths of polystyrenes (poly(St)s) bearing thiol-end group were used as the covering agent of gold nanoparticle prepared by reduction using trisodium citrate. The resulting nanoparticles with ca. 13 nm diameter were dispersed in toluene when the molecular weight of the ligand poly(St) is larger than 1200. Larger sized Au-poly(St) could be obtained using disodium malate instead of the citrate. The colloidal gold nanoparticle with ca. 40 nm diameter was easily prepared only by changing the reducing agent. Finally, we have demonstrated to prepare

larger sized gold nanoparticle covered with a photochromic diarylethene polymer that shows large change in local surface plasmon resonance absorption according to the photochromic reaction even in a solution.

Femtosecond Laser Photolysis Studies on Temperature Dependence of Cyclization and Cycloreversion Reactions of a Photochromic Diarylethene Derivative

Yukihide ISHIBASHI, Toshiyuki UMESATO, Seiya KOBATAKE, Masahiro IRIE, and Hiroshi MIYASAKA
J. Phys. Chem. C, Vol. 116(7), pp. 4862–4869 (2012).

Temperature dependencies of cyclization and cycloreversion processes of a photochromic diarylethene derivative, 1,2-bis(2-methyl-3-benzothienyl)perfluorocyclopentene, were investigated by steady-state spectroscopy and femtosecond laser photolysis methods. Steady-state measurements revealed that the cyclization reaction quantum yield and the fraction of the conformer with C_{2v} symmetry favorable for the cyclization (antiparallel, AP conformer) were independent of temperature in the range of 253–343 K. These results indicated that the cyclization reaction of the AP conformer in the open-ring isomer in the excited state had no apparent temperature dependence and suggested that the fate of the excited AP conformer in the open-ring isomer, such as cyclization or deactivation to the ground state, was determined at the conical intersection. On the other hand, the cycloreversion reaction was dependent on the temperature; the reaction quantum yield increased together with a decrease in the lifetime of the excited state of the closed-ring isomer with increasing temperature. On the basis of the adiabatic energy surface for the reaction profiles, it was deduced that the rapid deactivation into the ground state took place in the S_1 state in competition with the activated pathways leading to the conical intersection where the cycloreversion occurred.

Plasmonic Enhancement of Gold Nanoparticles on Photocycloreversion Reaction of Diarylethene Derivatives Depending on Particle Size, Distance from the Particle Surface, and Irradiation Wavelength

Hiroyasu NISHI, Tsuyoshi ASAHU, and Seiya KOBATAKE
Phys. Chem. Chem. Phys., Vol. 14(14), pp. 4898–4905 (2012).

We newly synthesized various sized gold nanoparticles covered with photochromic polymers consisting of diarylethenes with various structures to investigate an effect of the gold nanoparticles on the photocycloreversion reaction of the diarylethene chromophores upon irradiation with visible light. The gold nanoparticles covered with the photochromic polymers exhibited reversible changes in localized surface plasmon resonance (LSPR) absorption along with the photochromic reaction depending on the diameter of the particle, the distance between the gold surface and the chromophore, and the structure of the diarylethene chromophore. The rate of the photocycloreversion reaction of the chromophores around the particle was enhanced by the gold nanoparticles and the degree of the enhancement was affected by the diameter of the particle and the distance from the gold surface, while a structural difference in the diarylethene chromophore had no effect on the degree of the enhancement. The larger enhancement of the photocycloreversion reaction was observed by irradiation at longer wavelength side than visible light corresponding to the LSPR frequency.

Morphology, Wettability and Photomicro patterning of Superhydrophobic Surface with High Adhesive Force by Crystal Growth of a Photochromic Diarylethene

Daichi KITAGAWA and Seiya KOBATAKE
Chem. Sci., Vol. 3(5), pp. 1445–1449 (2012).

A photochromic diarylethene, 1,2-bis(2-methyl-6-nitro-1-benzothiophen-3-yl)perfluorocyclopentene, can undergo crystallization from the amorphous film in poly(methyl methacrylate) at 130°C. The contact angle with water on the film changed from 82° to 132° upon crystallization. Moreover, by heating at 180 °C, the contact angle increased to 154°, showing a superhydrophobic surface (water contact angle > 150°). The change in the contact angle can be ascribed to the surface roughness change by the crystal growth. The superhydrophobic surface also showed high-water adhesive properties. Patterning of the superhydrophobic and hydrophobic surfaces was performed using a photomask by photoirradiation leading to a resolution of about 10 μm. The contact angle on the photoirradiated area was reduced to 138° along with lowering of the surface roughness because of poorer crystal growth of the photoirradiated crystals. Such a superhydrophobic surface with high adhesive force is useful for water capturing devices.

Systematic Study on the Thermal Cycloreversion Reactivity of Diarylethenes with Alkoxy and Alkyl Groups at the Reactive Carbons

Hiroaki SHOJI, Daichi KITAGAWA, and Seiya KOBATAKE

Res. Chem. Intermed. in press.

The relationship between the thermal cycloreversion reactivity of diarylethenes and the bulkiness of the substituents at the reactive carbons was systematically investigated. Two photochromic diarylethenes, 1,2-bis(2-isobutoxy-5-phenyl-3-thienyl)perfluorocyclopentene and 1,2-bis(2-neopentoxy-5-phenyl-3-thienyl)perfluorocyclopentene, were newly synthesized and their optical properties and thermal cycloreversion reactivity were examined, because there is insufficient data for diarylethenes with alkoxy groups at the reactive carbons. The steric substituent constant was employed to correlate the relationship between the thermal cycloreversion reactivity of diarylethenes with alkyl and alkoxy groups at the reactive carbons and the bulkiness of the substituent. A good correlation was obtained for the substituent constant using CH₂ instead of oxygen in the alkoxy groups. The results indicate that this is a very useful strategy for the design of novel diarylethenes with desired thermal cycloreversion reactivity.

Plasmonic Enhancement of a Photocycloreversion Reaction of a Diarylethene Derivative Using Individually Dispersed Silver Nanoparticles

Hiroyasu NISHI, Tsuyoshi ASAH, and Seiya KOBATAKE

Chem. Phys. Chem. in press.

The fabrication of silver nanoparticles covered with polymers with a well-defined core-shell structure and the quantitative evaluation of the plasmonic enhancement effect on a photochemical reaction in the vicinity of these silver nanoparticles individually dispersed in a medium are described. The photocycloreversion reaction of a diarylethene polymer in the vicinity of silver nanoparticles was enhanced by 2-6 times relative to the reaction without the nanoparticles. The promotion of the photocycloreversion reaction is due to enhancement of the electromagnetic field near the surface of the silver core.

Photoresponsive Actuator of Diarylethene Molecular Crystals

Seiya KOBATAKE

Jpn. J. Optics (Kogaku), Vol. 41(2), pp. 66–70 (2012) (in Japanese).

Materials that can reversibly change shape and/or size in response to external stimuli have attracted much attention as an actuator. Especially, a light-driven actuator allows remote operation without any direct contact. This paper describes herein single-crystalline photochromism of diarylethenes, light-driven deformation of the diarylethene crystals, and a potential application to the actuator.

Crystalline Photochromism (2.4)

Masahiro IRIE and Seiya KOBATAKE

In *Advanced Materials System, One Point 8, Photochromism*, Kyoritsu Shuppan, pp. 42–52 (2012) (in Japanese).

Photoresponsive Crystal Shape Change of Photochromic Diarylethenes

Seiya KOBATAKE

14th Asian Chemical Congress (14 ACC), Invited Lecture, Bangkok, Thailand, September 5–8, 2011; Abstract INV0248, p. 243 (2011).

Photoresponsive Crystal Shape Change of Photochromic Diarylethenes

Seiya KOBATAKE

7th Handai Nanoscience and Nanotechnology International Symposium, Invited Lecture, Osaka, November 10–11, 2011; Abstract C-3, pp. 42–43 (2011).

Photofunctional Organic Crystals Actuated by Photoirradiation

Seiya KOBATAKE

Research Group on Imaging Display and Materials/Research Group on Polymers for Microelectronics and Photonics, The Society of Polymer Science, Japan, Invited Lecture, Amagasaki, December 21, 2011;

Abstract, pp. 5–6 (2011) (in Japanese).

Current and Future Trends of Single Crystalline Photochromism of Diarylethenes

Seiya KOBATAKE

38th Study Meeting, 174th Committee on Molecular Nanotechnology, Japan Society for the Promotion of Science, Invited Lecture, Kyoto, March 2, 2012; Abstract, pp. 7–12 (2012) (in Japanese).

Design and Function of Photochromic Molecular Materials in the Solid State

Seiya KOBATAKE

61st Symposium on Macromolecules, Invited Lecture, Nagoya, September 19–21, 2012; *Polymer Preprints*, Vol. 61(2), 4506–4508 (2012) (in Japanese).

Synthesis of Silaoxazolinium Salts of Weakly Coordinating Anions: Structures and Catalytic Properties in Aldol Reaction

Anugu Chandra, Sheker Reddy, Zhang Chen, Tohru Hatanaka, Tatsuya Minami and Yasuo Hatanaka, *Organometallics*, in press.

Synthesis and structures of silaoxazolinium salts and their application to the catalytic Mukaiyama aldol reaction are reported. Reaction of *N*-amidomethyl(dimethyl)chlorosilane or *N*-amidomethyl[bis(trimethylsilyl)]chlorosilane with metal salts of weakly coordinating anions such as CsB[3,5-(CF₃)₂C₆H₃]₄ (TFPB anion) and Na[CB₁₁H₁₂] (carba-*closo*-dodecaborate anion) gave the corresponding five-membered ring silaoxazolinium salts in high yields (93–97%). The structures of a series of silaoxazolinium salts were determined by X-ray crystal analysis as well as ²⁹Si NMR spectra. It has been revealed that the silicon atoms of silaoxazolinium salts are nearly completely free from the coordination of anions and the geometries of the silicon centers are distorted tetrahedral. The ²⁹Si chemical shifts of salts appeared in a range of 31 to 49 ppm, indicating the appreciable silylium cation character of the silicon. Silaoxazolinium salt of TFPB anion exhibited effective catalytic activity for the Mukaiyama aldol reaction of unactivated ketones such as cyclohexanone and acetophenone, giving high yields of the corresponding aldol products. The catalytic activity is highly dependent on the nature of the counter anions and the substituents on the silicon. DFT calculation of silaoxazolinium cation has disclosed that positive charges of silaoxazolinium cations are mainly located at the silicon atoms, while the nitrogen atoms and oxygen atoms are negatively charged.

Configurational Labile Silyl Triflimides: Application to Asymmetric Diels-Alder Reaction

Yuhstake Sakaguchi, Yuhki Iwade, Tetsuo Kurata, Tohru Hatanaka, Tatsuya Minami and Yasuo Hatanaka *Chem. Commun.* in press.

²⁹Si NMR studies of chiral silyl triflimides and asymmetric Diels-Alder reaction catalyzed by chiral silyl triflimides are reported. Effectiveness of new silicon catalysts was comparable to those of the best catalysts for Diels-Alder reaction so far reported. NMR studies strongly suggested that configurational lability of stereogenic pentacoordinate silicon center led to the high enantioselectivities.

Flavin-binding of Azoreductase: Direct Evidences for Dual-binding Property of Apo-azoreductase with FMN and FAD

Toshihiko OOI, Daiki OGATA, Ken'ichiro MATSUMOTO, Gen NAKAMURA, Jian YU, Min YAO, Masaya KITAMURA, and Seiichi TAGUCHI

J. Mol. Cat. B:Enzymatic, Vol. 74, pp. 204–208 (2012).

The flavin selectivity of the flavoenzymes is considered to be very strict in terms of the functional expression of the enzyme. However, we found that an FMN-dependent azoreductase from *Bacillus* sp. B29 exhibited up to 60% of the activity of native AzrA harboring FMN upon the addition of a FAD cofactor. The FAD binding to the apo-form of AzrA was identified by spectrophotometric analysis, and the bound FAD was stably retained in the enzyme molecule without degradation to FMN. On the other hand, no effect of riboflavin on the activity of AzrA was detected and there was no obvious quenching of riboflavin detected with addition of apoAzrA. By a docking simulation of FAD into structure of a homolog of AzrA (AzoR from *Escherichia coli*), we created a FAD-binding model. Taking all of these results together, it is proposed that the isoalloxazine ring of FAD localizes at the same site and plays the same role as that of FMN in AzrA.

Construction and Humanization of a Functional Bispecific EGFR × CD16 Diabody Using a Refolding System

Ryutaro ASANO, Makoto NAKAYAMA, Hiroko KAWAGUCHI, Tsuguo KUBOTA, Takeshi NAKANISHI, Mitsuo UMETSU, Hiroki HAYASHI, Yu KATAYOSE, Michiaki UNNO, Toshio KUDO, and Izumi KUMAGAI

FEBS J., Vol. 279, pp. 223–233 (2012).

We previously reported the construction and activity of a humanized, bispecific diabody (hEx3) that recruited T cells towards an epidermal growth factor receptor (EGFR) positive tumor. Herein, we describe the construction of a second functional, fully humanized, anti-EGFR bispecific diabody that recruits another subset of lymphocyte effectors, the natural killer cells, to EGFR-expressing tumor cells. After we confirmed that an anti-EGFR × anti-CD16 bispecific diabody (Ex16) consisting of a previously humanized anti-EGFR variable fragment (Fv) and a mouse anti-CD16 Fv had growth inhibitory activity, we designed a humanized anti-CD16 Fv to construct the fully humanized Ex16 (hEx16). However, the humanized form had lower activity for inhibition of cancer growth. To restore its growth inhibitory activity, we introduced mutations into the Vernier zone, which is located near the complementarity-determining regions and is involved in their binding activity. We efficiently prepared 15 different hEx16 mutants by expressing each chimeric single-chain component for hEx16 separately. We then used our in vitro refolding system to select the most functional mutant, which had a growth inhibitory effect comparable with that of the commercially available chimeric anti-EGFR antibody, cetuximab. Our refolding system could aid in the efficient optimization of other proteins with heterodimeric structure.

A High-Affinity Gold-Binding Camel Antibody: Antibody Engineering for One-Pot Functionalization of Gold Nanoparticles as Biointerface Molecules

Takamitsu HATTORI, Mitsuo UMETSU, Takeshi NAKANISHI, Satoko SAWAI, Shinsuke KIKUCHI, Ryutaro ASANO, and Izumi KUMAGAI

Bioconjug. Chem., Vol. 23, pp. 1934–1944 (2012).

Antibodies, with their high affinity and specificity, are widely utilized in the field of protein engineering, medicinal chemistry, and nanotechnology applications, and our recent studies have demonstrated the recognition and binding of antibody for the surface on inorganic material. In this study, we generated high affinity gold-binding antibody fragment by a combination of peptide-grafting and phage-display techniques and showed the availability of the material-binding fragment for one-pot functionalization of nanoparticles as interface molecules. After a gold-binding peptide sequence was grafted into one of the complementarity determining regions of a single variable domain of a heavy-chain camel antibody, a combinatorial library approach raised by 20 times the affinity of the peptide-grafted fragment. The high affinity gold-binding fragment (E32) spontaneously adsorbed on gold nanoparticles, and consequently the nanoparticles formed a stable dispersion in a high-ionic-strength solution. Multivalent and bispecific antibodies constructed on the E32 platform by means of fusion technology functionalized gold nanoparticles in one pot, and these

functionalized nanoparticles could be used to obtain surface plasmon resonance scattering images of cancer cells and to spontaneously link two different nanomaterials. Here, we propose the bispecific antibodies as convenient interface molecules in nano-sized world.

Crystal Nucleation Induced by Diffusion of Solute Molecules

K. IGARASHI, R. YAMAMOTO and H. OOSHIMA

Proc. of The First Asian Crystallization Technology Symposium, 2012, Seoul Korea

Development of a Novel Fines Dissolution Mechanism for Production of Large Crystals in Batch Crystallization

K. IGARASHI, M. ARIMOTO, H. OOSHIMA

Proc. of The 9th International Conference on Separation Science and Technology, 2011, Jeju Korea

Effect of Complete Dissolution of Once Appeared Crystals on Induction Period and Crystal Size in Cooling Crystallization of p-Acetanisidide

K. IGARASHI, A. KITANO, I. KODUTSUMI and H. OOSHIMA

Proc. of The 9th International Conference on Separation Science and Technology, 2011, Jeju Korea

Control of Crystal Size Distribution Using a mL-Scale Continuous Crystallizer Equipped with a High Speed Agitator

K. IGARASHI, Y. YAMANAKA, M. AZUMA and H. OOSHIMA

Journal of Chemical Engineering of Japan, Vol. 45(1), pp.28-33 (2012)

A mL-scale continuous crystallizer has been newly developed to produce small crystals with a narrow size distribution. The crystallizer is used for the poor solvent crystallization of glycine and L-alanine. The crystallizer is composed of a stainless-steel mixing vessel with an inner volume of 0.9 mL and a high-speed agitator that can agitate the crystallization solution up to 24,000 rpm. Glycine or L-alanine aqueous solution and poor solvent (methanol) are supplied into the vessel at a constant flow rate and intensely mixed by the agitator. The average residence time was set at 0.33, 3.3 and 33 s by changing the flow rate of an amino acid solution and poor solvent. The crystals obtained by the crystallizer are small and uniform in size, comparing with those obtained by a conventional beaker-scale semi-batch and continuous MSMR type crystallizers. For example, glycine crystals having the 1/38 of the size of crystals obtained by a semi batch crystallizer were obtained. The short residence time that can be attained by the present mL-scale crystallizer is advantageous for the production of small crystals with a narrow size distribution. The size distribution can be further controlled by changing the mixing ratio of poor solvent.

Structure of Super-saturated Solution and Crystal Nucleation

H. OOSHIMA

Proc. of The First Asian Crystallization Technology Symposium (ACTS-2012), Seoul Korea, FA-01 Plenary, p.1 (2012)

Repeated Cooling Crystallization for Production of Microcrystals with a Narrow Size Distribution

Z. XING, K. IGARASHI, A. MORIOKA and H. OOSHIMA

Journal of Chemical Engineering of Japan, Vol. 45(10), pp. 811–815 (2012)

The batch cooling crystallization of an organic compound, *p-acetanisidide*, was carried out using methanol as a solvent and no seed crystal. The crystallization needed an induction period of 10–200 min before nucleation, and the size distribution of the product crystals was broad with sizes ranging from 10 to 270 μm determined as the diameter of a circle with equal projection area. In order to control the nucleation process and obtain microcrystals with a narrow size distribution, the dissolution of crystals obtained by cooling crystallization, followed by recrystallization was adopted. Thus, the crystals once obtained by cooling crystallization were completely dissolved by heating the slurry to a temperature 17°C that was higher than the saturation temperature by 1.5°C. After the solution was maintained at that temperature for a given time, it was cooled again. In the case of repeated crystallization, the induction period observed in the first crystallization disappeared, and small crystals with a mean diameter of 40 μm and a narrow size distribution were obtained. However, the effect of the complete dissolution of crystals on the production of microcrystals

with a narrow size distribution disappeared when the solution was incubated at 17°C over 90 min. These results were explained on the basis of the history of the solution structure.

Protein recognition of hetero-/homoleptic ruthenium(II) tris(bipyridine)s for α -chymotrypsin and cytochrome *c*

Yoshinobu YAMAGUCHI, Nobuo Kato, Hideki AZUMA, Takeshi NAGASAKI and Junko OHKANDA
Bioorg. Med. Chem. Lett., Vol. 22(6), pp. 2354–2358 (2012).

We examined the relationship between the structures of hetero-/homoleptic ruthenium(II) tris(bipyridine) metal complexes (RuII(bpy)₃) and their binding properties for α -chymotrypsin (ChT) and cytochrome *c* (cyt *c*). Heteroleptic compound 1a binds to both ChT and cyt *c* in 1:1 ratio, whereas homoleptic 2 forms 1:2 protein complex with ChT but 1:1 complex with cyt *c*. These results suggest that the structure of the recognition cavity in RuII(bpy)₃ can be designed for shape complementarity to the targeted proteins. In addition, RuII(bpy)₃ complexes were found to be potent inhibitors of cyt *c* reduction and to permeate A549 cells.

Quantitative comparison between poly(L-arginine) and poly(L-lysine) at each step of polyplex-based gene transfection using a microinjection technique

Tomoko HASHIMOTO, Takeshi KAWAZU, Takeshi NAGASAKI, Akira MURAKAMI and Tetsuji YAMAOKA

Sci. Technol. Adv. Mater., Vol. 13(1), 015009/1–015009/8 (2012).

Among the well-studied polypeptide-type gene carriers, transfection efficiency is empirically known to be higher for poly(L-arginine) (PR) than poly(L-lysine) (PK). The big difference between PR and PK should be determined at one of the intracellular trafficking steps based on the different charge densities, structures or pKa values. However, the endosomal escape and the intranuclear transcription efficiency in living cells have not been clarified yet. In this study, a novel method for quantifying the intranuclear transcription efficiency and the nuclear transport of the polyplex is established based on the nuclear and the cytosolic microinjection technique, and the results for PK and PR with different molecular weights (MWs) are compared in living cells. The intranuclear transcription efficiency is the same in PR and PK and it decreases rapidly with increasing MW, in spite of the commonly measured transfection efficiency. The transcription efficiency is strongly suppressed at high MW and strongly correlates with the polyplex forming ability expressed as a critical ratio of the number of polypeptide cationic groups to the number of pDNA anionic groups. When considered with the results of the cellular uptake and *in vitro* transfection with or without chloroquine, the rate-limiting step for their gene transfer is the buffering effect-independent endosomal escape.

HVJ-E/importin- β hybrid vector for overcoming cytoplasmic and nuclear membranes as double barrier for non-viral gene delivery

Takeshi KAWAZU, Hiroyuki KANZAKI, Atsushi UNO, Hideki AZUMA and Takeshi NAGASAKI
Biomed. Pharmacother., Vol. 66(7), pp. 519–524 (2012).

In order to enhance the nuclear import of the transgene, we prepared plasmid DNA/importin- β conjugates consisting of biotinylated poly(ethylenimine)s and recombinant streptavidin-fused importin- β . Hemagglutinating virus of Japan-envelope (HVJ-E) vector containing the PEI polyplex/importin- β conjugate showed high transfection efficiency not only *in vitro* but also *in vivo*. We showed that novel HVJ-E/importin- β -conjugated PEI polyplex hybrid vector could overcome plasma and nuclear membrane barriers to achieve effective transfection.

Inorganic boron cluster materials for new radiation treatment by generating radiation inside of body

Takeshi NAGASAKI

Expected Mater. Future (Mirai Zairyo), Vol. 12(5), pp. 34-39 (2012) (in Japanese).

Recently, boron neutron capture therapy (BNCT) attracts attention as a cancer therapy of the low side effect. It is important to deliver ¹⁰B atoms only into the carcinoma cell selectively for the improvement of the treatment efficiency. In this review article, novel inorganic boron clusters are focused on developing a effective new radiation treatment for cancer by generating radiation inside of body.

Potential of polyion complex nanoparticle composed of mercaptoundecahydrododecaborane-appnded

high molecular weight polyamine as a boron carrier for neutron capture therapy

Takeshi NAGASAKI, Masayuki UMANO, Hironobu YANAGIE, Mitsunori KIRIHATA, Shin-ichiro MASUNAGA and Koji ONO

2011 MRS Fall Meeting, Boston, MA, USA, November 28-December 3, 2011; Preprints.

Tumor-targeting and boron neutron capture therapy by using biodegradable polyamines conjugated with boron clusters

Takeshi NAGASAKI, Yuxiang Zhu, Hideki AZUMA, Mitsunori KIRIHATA, Shin-ichiro MASUNAGA and Koji ONO

The 39th Annual Meeting & Exposition of the Controlled Release Society, Québec City, Canada, July 15-18, 2012; Preprints.

Dectin-1 mediated delivery system of anti-inflammatory drug and photo-sensitizer to immune cells

Yuta KAGOSHIMA, Jiawei LI, Atsushi IKEDA, Hideki AZUMA and Takeshi NAGASAKI

The 39th Annual Meeting & Exposition of the Controlled Release Society, Québec City, Canada, July 15-18, 2012; Preprints.

LidNA, a novel miRNA inhibitor constructed with unmodified DNA

Akira Tachibana, Yui Yamada, Hiroyuki Ida, Satoshi Saito & Toshizumi Tanabe

FEBS Lett. 586, 1529-1532 (2012).

Many miRNA inhibitors have been developed and they are chemically modified oligonucleotides such as 2'-O-methylated RNA and locked nucleic acid (LNA). Unmodified DNA has not yet reported as miRNA inhibitor because of low affinity of DNA/miRNA than mRNA/miRNA. We designed the structured DNA that was constructed with unmodified DNA and significantly inhibited miRNA function. The structure that needed for the activity was the miRNA binding site between double stranded regions that were responsible for the miRNA inhibitory activity and tight binding to miRNA. We firstly developed the miRNA inhibitor constructed with unmodified DNA, named LidNA, DNA that put the *lid* on miRNA function.

Dermokine- β impairs ERK signaling through direct binding to GRP78.

Higashi K, Hasegawa M, Yokoyama C, Tachibana T, Mitsui S, Saito K,

FEBS Lett. 586, 2300-2305. (2012)

Dermokine- β is abundant in stratified epithelia and in differentiating cultured keratinocytes. In this study, we investigated the role of dermokine- β in differentiation of keratinocytes. Treatment of keratinocytes or skin tumor cells with dermokine- β attenuated phosphorylation of extracellular-signal-regulated kinase (ERK). Exposure of cells to dermokine- β , as well as its carboxyl-terminus domain peptide, interrupted phosphorylation of ERK and stimulated dermokine gene expression. Inhibition of ERK signaling by its specific inhibitor also increased dermokine expression level. A combination of chemical cross-linking and immunoprecipitation, followed by proteomics analyses, identified glucose-regulated protein 78 (GRP78) as a dermokine- β -associated protein. Blockage of GRP78 expression by a specific siRNA abrogated actions of dermokine- β . These findings provide novel insights into the physiological significance of dermokine- β in the epidermis.

Altered expression of dermokine in skin disorders.

Hasegawa M, Higashi K, Yokoyama C, Yamamoto F, Tachibana T, Matsushita T, Hamaguchi Y, Saito K, Fujimoto M, Takehara K.

J. Eur. Acad. Dermatol. Venereol. doi: 10.1111/j.1468-3083.2012.04598.x. (2012)

Although dermokine- β , a glycoprotein expressed in epithelial cells, does not have significant homology to other proteins, its carboxyl-terminal domain shares a high pI value with many cytokines, suggesting similar functions. Objective To better understand the biology of dermokine, we here determined its localization under pathological conditions and examined factors that regulate its expression. Methods We generated an anti-human dermokine- β/γ monoclonal antibody cross-reacting with the mouse protein. Using this antibody, immunohistological staining and Western blotting of dermokine- β/γ were performed with various tissue samples. Although human dermokine- β/γ was expressed in almost all granular layers, upper spinous layers of the skin were also stained with anti-dermokine- β/γ antibody in inflammatory skin disorders.

Dermokine- β/γ was expressed in keratoacanthoma and a part of well-differentiated squamous cell carcinoma (SCC). However, dermokine- β/γ was not detected in poorly differentiated SCC or tumours derived from non-keratinocytes. In mice, dermokine- β/γ -expressed keratinocytes were increased in models of contact hypersensitivity, ultraviolet-irradiated skin injury and wound healing. Consistent with expanded distribution in inflammatory skin diseases, proinflammatory cytokines such as interleukin- 1β , interleukin-12, and tumour necrosis factor- α augmented dermokine- β/γ expression in cultured human keratinocytes. In contrast, growth factors including epidermal growth factor, insulin-like growth factor-I, keratinocyte growth factor and transforming growth factor- α significantly reduced dermokine expression. These results provide novel insights into the physiological and pathological significance of dermokine in the epidermis.

Chd2 interacts with H3.3 to determine myogenic cell fate.

A. HARADA, S. OKADA, D. KONNO, J. ODAWARA, T. YOSHIMI, S. YOSHIMURA, H. KUMAMARU, H. SAWAI, T. TSUBOTA, H. KURUMIZAKA, K. AKASHI, T. TACHIBANA, AN. IMBALZANO, Y. OHKAWA.

EMBO J. 31, 2994-3007. (2012)

Cell differentiation is mediated by lineage-determining transcription factors. We show that chromodomain helicase DNA-binding domain 2 (Chd2), a SNF2 chromatin remodelling enzyme family member, interacts with MyoD and myogenic gene regulatory sequences to specifically mark these loci via deposition of the histone variant H3.3 prior to cell differentiation. Directed and genome-wide analysis of endogenous H3.3 incorporation demonstrates that knockdown of Chd2 prevents H3.3 deposition at differentiation-dependent, but not housekeeping, genes and inhibits myogenic gene activation. The data indicate that MyoD determines cell fate and facilitates differentiation-dependent gene expression through Chd2-dependent deposition of H3.3 at myogenic loci prior to differentiation.

The classification of mRNA expression levels by the phosphorylation state of RNAPII CTD based on a combined genome-wide approach.

J. ODAWARA, A. HARADA, T. YOSHIMI, K. MAEHARA, T. TACHIBANA, S. OKADA, K. AKASHI, Y. OHKAWA.

BMC Genomics. 12, 516 (2011)

Cellular function is regulated by the balance of stringently regulated amounts of mRNA. Previous reports revealed that RNA polymerase II (RNAPII), which transcribes mRNA, can be classified into the pausing state and the active transcription state according to the phosphorylation state of RPB1, the catalytic subunit of RNAPII. However, genome-wide association between mRNA expression level and the phosphorylation state of RNAPII is unclear. While the functional importance of pausing genes is clear, such as in mouse Embryonic Stem cells for differentiation, understanding this association is critical for distinguishing pausing genes from active transcribing genes in expression profiling data, such as microarrays and RNAseq. Therefore, we examined the correlation between the phosphorylation of RNAPII and mRNA expression levels using a combined analysis by ChIPseq and RNAseq. We first performed a precise quantitative measurement of mRNA by performing an optimized calculation in RNAseq. We then visualized the recruitment of various phosphorylated RNAPIIs, such as Ser2P and Ser5P. A combined analysis using optimized RNAseq and ChIPseq for phosphorylated RNAPII revealed that mRNA levels correlate with the various phosphorylation states of RNAPII. We demonstrated that the amount of mRNA is precisely reflected by the phased phosphorylation of Ser2 and Ser5. In particular, even the most "pausing" genes, for which only Ser5 is phosphorylated, were detectable at a certain level of mRNA. Our analysis indicated that the complexity of quantitative regulation of mRNA levels could be classified into three categories according to the phosphorylation state of RNAPII.

Architecture and Building Engineering

Vibration Test Using a Plate Model to Verify the Effect of Vibration Control of Tuned Mass Dampers with Initial Displacement under Impulse Loading

Susumu YOSHINAKA, Shuji NISHIYAMA and Yoshiya TANIGUCHI

AIJ Journal of Technology and Design, Vol.17, No.37, pp.835-840 (2011) (in Japanese)

To effectively control transient responses, we propose TMDs with initial displacement. The initial displacement can change the phases of beat envelope curves resulting from superposition of two vibration modes with closely spaced natural frequencies. In this paper, we describe the vibration test under impulse loading to verify the effect of the proposed system experimentally and that a model of TMD made on an experimental basis works validly. Firstly, we explain the effect of vibration control of the proposed method to the plate model on the analytical basis. Then, we explain experimental results and lastly compared experimental results and analytical results.

Study of Single Layer Two-way Grid Shell with Tension Member

M. FUJIMOTO, A. TAKINO(Osaka University), Z. ZHANG, and K. IMAI

Proceedings of IABSE-IASS Symposium 2011, London, Sept.. 20- 23, Paper No. 254

We have previously reported on the buckling behaviour of single layer two-way grid shells with tension members installed as diagonals of a two-way grid. A tension member's function is to increase the in-plane rigidity of a single layer two-way grid and improve its stability behaviour. This study treats a single layer two-way grid cylindrical shell roof comprising a prefabricated wooden truss system with tension members. We focus on tension member installation and placement pattern as both diagonal members of two-way grids and out-of-plane stiffened members in a cylindrical surface. The experimental and numerical study examines the effects of tension members on the buckling behaviour of a single layer two-way grid cylindrical shell roof.

Effect of Tension Member on Buckling and Strength of Single Layer Two-way Grid Cylindrical Shell Roof

Z. ZHANG, M. FUJIMOTO, and A. TAKINO(Nara Women's University)

Proceedings of IASS-APCS Symposium 2012, Seoul, May 21- 24, Paper No. FF-128

This study treats the effects of tension member installation on the buckling load and strength of a single layer two-way grid cylindrical shell roof using numerical methods. Tension members are installed to stiffen the rigidity of the two-way grid shell roof. The tension member placement pattern, load distribution pattern, and initial imperfections are considered as numerical calculation parameters. It is confirmed by numerical analysis that tension members in out-of-plane and diagonals can cause increased buckling and strength of the two-way grid shell.

Relation between individual evaluation of light environment and personal attributes

Ryohei KAWAMOTO, Noriko UMEMIYA, Hiroshi ATSUTA and Tamami SUZUKI

Proceedings of the 27th Session on the International Commission on Illumination, CIE2011 Sun city, Vol.1, Part2, pp.1076-1085, 2011.

The light environment in a climate chamber was evaluated at two levels of lighting. Differences in evaluations offered by 200 student subjects were analyzed. Results revealed the following. 1) Sleep time during the day before the experiments, regularity of meal times, habits of window opening, and desire for a natural life are all related to evaluation of light. 2) Sex, use of corrective lenses, site of residence, and habits of saving light are unrelated to light evaluation. 3) Lighting comfort and preference depend on whether subjects live in wooden homes or in concrete homes. Concrete-home-residents are more comfortable than wooden-home-residents in

dark conditions, although light environment evaluations of concrete-home-residents and wooden-home-residents do not differ in a lighted condition. 4) Wooden-home-residents respond similarly to concrete-home residents if they do not desire continuity to outdoors. Concrete-home-residents respond similarly to wooden-home-residents if they change lighting according to the weather. Results of this study clarify that it is necessary to consider subjects' environmental consciousness and lighting habits during comfort and preference evaluations of light, although little effects of these attributes were found in brightness evaluation. Consideration of these attributes will engender more comfortable and preferred lighting design.

Relation of surrounding building configuration and mitigation effects of school lawn planting

Takayuki HARADA, Noriko UMEMIYA, Yuta SAKURAI, Ryota MATSUI, Ryohei KAWAMOTO, Toshiki NAOTUKA, Yumi OZAKI, Satoshi HIRATA

Proceedings of the 12th International Building Performance and Simulation Association Conference, Building Simulation 2011, Sydney, pp.2011-2016, 2011.

Lawn planting in an elementary school playground scattered in urban areas is expected to mitigate heat-island phenomena. This study, using CFD analysis, presents the degree to which this mitigation changes according to the configuration of surrounding buildings. Some examinations assess existing school shapes (CASES 1–4). Other cases are configured symmetrically from east to west (CASES 5–8). In two school shapes, the summer thermal environment in a school is assessed when its playground is covered with a lawn (CASES 2•4•6•8) and when covered with bare soil (CASES 1•3•5•7). Results of this study show, by simulating typical primary schools in urban regions having high building in surrounding areas, how high buildings can mitigate effects of lawn planning in schoolyards. Results show slight differences in the wind speed distribution when the schoolyard is made from bare ground into a lawn. An important consideration related to mitigation effects of primary school lawn planning in urban region is knowledge of the fluid properties in surrounding areas rather than the shape of the school building enclosing a schoolyard. Higher buildings in surrounding areas will have important effects.

Civil Engineering

Experimental Study on Strengthening Effect of High Modulus CFRP Strips Installed onto Lower Plate of I Shaped Girder

Nobuhito OCHI (Akashi National College of Technology), Masahide MATSUMURA and Nobuhiro HISABE (Mitsubishi Plastics, Inc.)

Keynote Lectures and Extended Abstracts of the Twelfth East Asia-Pacific Conference on Structural Engineering and Construction, EASEC12, pp. 219-220, 6pages in CDROM, January 26-28, Hong Kong SAR, China (2011)

Recently, number of steel bridges required to be strengthened to reduce working stress due to deterioration and updated design live load is increasing in Japan. Then additional steel plates are welded and bolted to these existing steel bridges in ordinary cases. However such conventional strengthening techniques have room for improvements onto construction workmanship. The use of high modulus CFRP strip as strengthening material is focused on for more rational and economical strengthening technique of superannuated existing I shaped steel girders.

Then, experimentally investigated in this study is strengthening effect of high modulus CFRP strips installed onto the lower flange plate of I shaped steel girder. Five girder specimens with different adhesive lengths of the CFRP strips to the lower flange plate are used in the bending tests. Also method to prevent CFRP strips from debonding at both ends of them is proposed and investigated in this experiment. Then, the bending strength and behavior of the strengthened I shaped steel girders are discussed.

Knock-off Effect of Steel Side Block as Displacement Restrainers on Dynamic Response of Isolated Bridge Structure

Kazuyuki ISHIHARA, Masahide MATSUMURA, Masahiko YOSHIDA (Kawakin Core-Tech Co.,Ltd.) and Minoru SAKAIDA (Sakaida Bridge Engineering & Consulting)

Keynote Lectures and Extended Abstracts of the Twelfth East Asia-Pacific Conference on Structural Engineering and Construction, EASEC12, pp. 656-657, 8pages in CDROM, January 26-28, Hong Kong SAR, China (2011)

Displacement restrainers of the superstructure in the transverse direction of the isolated bridge are usually installed to protect expansion joints from damage during earthquake. Steel side blocks, one of the displacement restrainers, are set near both sides of isolating bearings. Here, a more rational seismic response of the isolated bridge in the transverse direction can be considered to be that the displacement of the superstructure during a small and moderate earthquake like Level 1 Earthquake defined in the JSHB (Specification of Highway Bridges) is restraint and the displacement during a strong earthquake like Level 2 Earthquake is released to mitigate damage of bridge pier and/or base structure and to enhance redundancy against a strong earthquake. For instance, steel side block, improved to have a knock-off function, will provide these responses of the isolated bridge. This study describes the outline of the side block with slit, which is developed by the authors to control the breaking load accurately. The breaking characteristics of the side block with knock-off function are verified through static breaking test using down-sized specimens with changes in dimension of the slit, like cross-sectional area and height of the slit. Also analytically clarified is the installation effect of the side block on dynamic response of the isolated bridge structures.

Experimental Study on Debonding Prevention Methods of High Elastic Modulus CFRP Strips Installed onto Lower Flange Plate of I Shaped Steel Girder

Nobuhito OCHI (Akashi National College of Technology), Masahide MATSUMURA and Nobuhiro HISABE (Mitsubishi Plastics, Inc.)

Journal of Structural Engineering, Vol.57A, JSCE, pp. 114-124 (2011) (in Japanese)

Installation of CFRP strips of high elastic modulus can be effective for improving the load carrying capacity of a superannuated existing steel I girder. Experimentally investigated in this study are some debonding prevention methods at the edges of the CFRP strips onto the lower flange plate. At the first step, the bending tests are carried out for six girder specimens with different adhesive lengths of the CFRP strips. Then, debonding prevention plates at the edges of the CFRP strips and tie plate and tie rod bridging both edges of the CFRP plates over the steel splice plate of bolted connection is proposed to prevent the debonding and the effectiveness of the methods are examined for the specimens with the debonding.

Analytical Modeling and Seismic Performance on In-plane Behavior of Rigid Framed Steel Bridge Pier

Masahide MATSUMURA, Yukiyasu HONTANI (TAISEI Corp.) and Toshiyuki KITADA

Journal of Structural Engineering, Vol.57A, JSCE, pp. 94-103 (2011) (in Japanese)

Rigid framed steel bridge piers had several damages like plate buckling by the attack of the Hyogo-ken Nambu

Earthquake. To update seismic design adequately evaluating strength and ductility on in-plane behavior of the pier, some analytical modeling, which can consider plate buckling, is required and is available now but not for practical business use. Then investigated in this study is an adequate modeling method when using beam-column element based on Euler-Bernoulli theory for the analysis and influences of some modeling methods on the seismic performance of the in-plane behavior of the pier.

Seismic Retrofit for an Existing Network Arch Bridge with Slit-type Knock-off Bearings

Koichi SUGIOKA (Hanshin Expressway Co.,Ltd.), Nobuhiro MASHIMA (Hanshin Expressway Co.,Ltd.), Hiroaki MATSUSHITA (Hitachi Zosen Corp.), Takehiko HIMENO (Kawakin Core-Tech Co.,Ltd.) and Masahide MATSUMURA

Journal of Structural Engineering, Vol.57A, JSCE, pp. 467- 478 (2011) (in Japanese)

Seismic retrofit of an existing network arch bridge against large-scale (Level 2) earthquake ground motions was performed by modifying existing fixed steel bearings into slit-type knock-off bearings. Three-dimensional non-linear dynamic response analyses were carried out considering site-specific ground motions. It was confirmed that shear panel dampers as passive energy-dissipation were needed on both fixed-side and movable-side pier tops to avoid the potentially difficult retrofit work for the undersea pier anchors and foundations. The authors proposed slit-type knock-off bearings with the knock-off function as triggers against the Level 2 ground motions to provide isolation effect. Performance tests of the slit-type knock-off bearings were conducted to verify the required performance for the seismic retrofit design.

Influence of Corrosion Area of the Girder Ends of Highway Bridges to its Load Carrying Capacity

Makoto USUKURA (Tokyo Consultants Co.,Ltd.), Takashi YAMAGUCHI, Yusuke TOYOTA, Yukiko MITSUGI (Ishikawa National College of Technology) and Akihisa KONDO (Sogo Engineering Inc.)

Journal of Structural Engineering, Vol.57A, JSCE, pp. 724- 734 (2011) (in Japanese)

In these days, it has been reported that some of steel bridges are deteriorated due to corrosion of the girder ends. Since the evaluation method of the load carrying capacity of the girder ends with corrosion is not established, understanding of mechanical property and ultimate strength of the girder ends is required from the viewpoint of repair works. In this paper, the load carrying capacity of the girder ends with corrosion of Highway Bridges is studied based on FE analysis. In particular, the influence of corrosion area and location of the girder ends to its load carrying capacity are discussed focusing on the height and length of the corrosion area, the size of the sole plate and so on.

Experimental Study on Application of High Strength Bolted Connections to Submerged Structures

Kyoichi NAKAYASU (Hitachi Zosen Corp.), Toshiaki MORII (Hitachi Zosen Corp.), Hiroaki MATSUSHITA (Hitachi Zosen Corp.) and Takashi YAMAGUCHI

Journal of Structural Engineering, Vol.57A, JSCE, pp. 831- 841 (2011) (in Japanese)

Most of field joints of the submerged structures such as steel penstock or hydraulic gates are welded on site. High strength bolted friction type joints are hardly applied because of change of slip coefficient due to penetration of water, lowering of axial force due to corrosion of bolt, delayed fracture of high strength bolt, and so on. On the other hand, in refurbishment of existing structures it will be difficult to apply welded joints to them in terms of weld ability of existing material, influence of thermal strain on accuracy, and limitation of work space at the site. If high strength bolted friction type joints can be applied to them, they will become one of the alternatives for refurbishment method, and widely contribute to improvement of workability, reliability and economic efficiency. In this paper, the experiment for high strength bolted frictional joints subjected to tensile load considering water pressure and site condition are carried out. Based on the experimental results, slip coefficient of them is evaluated taking into consideration about water penetration into the frictional surface.

Proposal of an Acoustic Method to Evaluate Vertical Misalignment between Plates of Steel Expansion Joints of Finger Type

Luiza H. ICHINOSE (Japan Industrial Testing Corp.), Masahide MATSUMURA, Tetsuji YAMAGAMI (Hanshin Expressway Engineering Co.,Ltd.) and Takashi YAMAGUCHI

Steel Construction Engineering, Vol.18, No.69, JSSC, pp. 1- 8 (2011) (in Japanese)

Mal-function and damages of expansion joints not only affects the smooth traveling of vehicles on the bridge, but are also sources of inconvenient noises and vibrations. In addition, impact due to live loads may cause damages to the girder end structures, being worsened in case a smooth transition between adjacent girders is not assured. The present study performed a series of field and loading tests to investigate the acoustic and vibrational structural effects of vehicles traveling on the surface of steel finger expansion joints. Effects of vertical misalignment

between the plates of the joint fingers were investigated and a diagnosis method based on acoustic evaluation is also proposed.

Study on Seismic Performance of a Box Sectional Steel Pier with Transversely Profiled Plates

Kunitaro HASHIMOTO (Kyoto University), Kunitomo SUGIURA (Kyoto University), Takashi YAMAGUCHI and Takuji KUMANO (JFE Engineering Corp.)

Journal of JSCE, Ser. A1 (SE/EE), Vol.67, No.1, pp. 177-192 (2011) (in Japanese)

For a box sectional steel column with transversely profiled plates (TP plate), cyclic loading tests, combined non liner FE analyses, pseudo-dynamic tests and dynamic FE analyses are carried out, in order to investigate its seismic performance. As results of cyclic loading tests and combined non liner FE analyses, it is shown that steel pier with TP plate have good seismic performances, and the taper ratio and the slenderness parameter are the larger, seismic performances are the better. And as results of pseudo-dynamic tests and dynamic FE analysis considering the real seismic acceleration, it is found that the response displacement of steel pier with TP plate is smaller than the one of ordinary steel pier.

Breaking Effects of Displacement Limiting Devices for Rubber Bearings

Masahide MATSUMURA

The 4th Taiwan-Japan Workshop on Bridge Engineering, 3pages, Kyoto Univ., Kyoto, April 2-3 (2011)

Study on Mechanical Behavior of High Strength Bolted Friction Panel Joint Members of Steel Truss Bridges and Calculation Method of its Effective Width

Takashi YAMAGUCHI, Shinsuke YOSHIDA (Kyoto University), Kunitaro HASHIMOTO (Kyoto University) and Kunitomo SUGIURA (Kyoto University)

Steel Construction Engineering, Vol.18, No.71, JSSC, pp. 27- 42 (2011) (in Japanese)

In this study, in order to clear the mechanical behavior of panel point of steel bridges using high strength bolted frictional joints, tensile loading experiment is carried out at first. Secondly, in order to make more detail clarification of the mechanical behavior and to examine the effective width of the gusset plate, finite element analysis has been executed by using the model which has same configuration of the specimen. From the results of this experiment and analysis, the collapse behavior of panel points of steel truss bridges is discussed and applicable evaluation methods of the load carrying capacity for yielding of such panel points are proposed.

Analytical Study on Rigid Connection Detail of Steel-Concrete Composite Rigid Frame Bridge Using Bearing Plate

Takashi YAMAGUCHI, Yuhei KAWAMOTO, Dai SAGOU (Takadakiko Co.,Ltd), Takao YAMADA (Takadakiko Co.,Ltd) and Kazuaki TANI (Takadakiko Co.,Ltd)

35th International Symposium on Bridge and Structural Engineering (IABSE), London, UK, September 20-23, (2011)

Recently, the number of steel-concrete composite rigid frame bridges in Japan is increasing for short and medium span length. To make this type of bridge more rational, it is important to ensure a good performance of the rigid connection. Therefore, a new type of the connection detail with bearing plate has been proposed by the authors. In this study, effectiveness and applicability of the proposed rigid connection detail with the bearing plate was examined by elasto-plastic finite displacement analysis. Mechanical behaviour of the connection detail up to the ultimate limit state is investigated based on them. It is found that the load can be securely transferred from the steel girder to the abutment through the bearing plate. It is concluded that the proposed connection detail can become one of the practical and effective rigid connection considering easiness of construction.

Study on Residual Strength of Riveted Joints Damaged by Corrosion

Kunitaro HASHIMOTO (Kyoto University), Takashi YAMAGUCHI and Kunitomo SUGIURA (Kyoto University)

35th International Symposium on Bridge and Structural Engineering (IABSE), London, UK, September 20-23, (2011)

In this study, in order to clarify a relationship between a residual strength and a level of corrosion damage, and to investigate a mechanical behaviour of riveted joints damaged at rivet head by corrosion, experimental and analytical studies are carried out. In the experiments, are used the specimens which cut off from the demolished existing steel bridge members. Experimental specimens of single lapped joints which are varied the corrosion levels are prepared and tensile tests are executed. In FE analysis, the corrosion levels of a rivet head and joint type which are single and double lapped joints are dealt with and parametric analyses are carried out. As the results of

this study, it is found that the residual strength of the riveted joint damaged by corrosion is much decreased when a rivet head is corroded heavily in especially the case of the single lapped riveted joint.

Model Test of Isolated Bridges with Displacement Control Device which Brakes under Strong Earthquake by Shaking Table and Its Dynamic Response Analysis

Nobuhito OCHI (Akashi National College of Technology) and Masahide MATSUMURA

The 2011 World Congress on Advances in Structural Engineering and Mechanics (ASEM'11+), pp. 2754-2762, 18-22 September, Seoul, Korea (2011)

In isolated bridges, some displacement restrainers of superstructures in the transverse direction of the bridge axis, like steel side block (SB), is usually installed for damage protection of expansion joints during earthquakes. However, it can be rational to expect the isolation effects in the transverse direction as well as in the bridge axis against a strong earthquake. Then, recently developed and proposed by the authors is the steel side block with the knock-off function (CSB), which breaks at a pre-set breaking load and provides smooth shift to the isolated conditions. In this study, small-size shaking table tests and dynamic response analysis of the isolated bridge models installed the CSB are carried out by changing breaking characteristics of the CSB. Then, analytical modeling method of the CSB is proposed and the validity of it is verified as compared with the tested dynamic responses.

Analytical Study on Elasto-Plastic Behavior of Steel Members Predominantly Subjected to Cyclic Axial Force

Tetsunari IMAMURA (Osaka University), Kiyoshi ONO (Osaka University), Hiroaki TANIUE (Osaka University), Nobuo NISHIMURA (Osaka University) and Masahide MATSUMURA

Proceedings of the 6th International Symposium on Steel Structures ISSS-2011, pp. 64-68, Seoul, Korea, 3-5 November (2011)

The seismic performance of steel bridge piers which predominantly subjected to cyclic bending moment and methods to evaluate seismic performance of steel bridge piers have been already proposed. On the other hand, there are little studies about the elasto-plastic behavior and the seismic performance of steel members predominantly subjected to cyclic axial force like chord members of steel truss bridges. The seismic performance of steel members predominantly subjected to cyclic axial force and the major buckling parameters affecting the seismic performance may be different from those of steel piers and it is not clear whether the previous seismic evaluation methods for steel bridge piers can be applied to the steel members predominantly subjected to axial force. Therefore, it is necessary to grasp the elasto-plastic behavior and the seismic performance of steel members predominantly subjected to cyclic axial force. In this paper, the elasto-plastic behavior of steel members predominantly subjected to cyclic axial force is investigated by the finite element analysis.

Modeling and Ultimate Strength of Steel Column Members Subjected to Predominant Axial Force in Truss Bridges

Masahide MATSUMURA, Junpei YOSHIYAMA, Kiyoshi ONO (Osaka University) and Hiroaki TANIUE (Osaka University)

Proceedings of the 6th International Symposium on Steel Structures ISSS-2011, pp. 275-282, Seoul, Korea, 3-5 November (2011)

Plate and member buckling greatly influence on the ultimate state of thin-walled steel column members which are widely used in steel truss bridge. Such members will show an elasto-plastic behavior when subjected to an excess load, though the column members are designed elastically. Then a beam-column element, by which the plate buckling cannot be considered, is generally used for modeling the column member in the analysis of the truss bridge. Therefore, a local buckling of the component plate panels and initial imperfections are not taken into account for the model. Then investigated analytically in this paper is the ultimate state of a steel truss bridge, which is designed based on the Specification for Highway Bridges in Japan and is subjected to an increasing monotonic load in the downward direction. Also carried out are static loading tests using such column specimens subjected to an increasing eccentric predominant axial load. The effect of the plate buckling on the ultimate strength of the member is discussed based on the analytical and experimental results.

Static and Cyclic Loading Test of Steel Bellows Made of Various Steel Materials in Axial Direction

Shinya HIRAHARA, Kentaro TANAKA (Setsunan University), Hiroshi ZUI (Setsunan University) and Masahide MATSUMURA

Proceedings of Constructional Steel, Vol.19, JSSC, pp. 395-402 (2011) (in Japanese)

Steel bellows as energy absorbing bridge connector is proposed by the authors. In this paper, cyclic behaviors of

steel bellows with the same shape and with different steel materials are investigated by static and cycling loading test. Also discussed is a simplified stress-strain relationship used in FEM analysis by considering an increased yield stress due to bending process of the steel bellows. It is concluded that the yield ratio of the steel materials greatly influenced the energy absorbing capacity of the steel bellows. The increased yield stress is necessary to be considered in the analysis to obtain equivalent energy absorbing capacity of the steel bellows made of steel materials with smaller yield ratio and subjected to large cyclic displacement.

Shaking Table Test of a Small Vibration System Considering Member Knocking-off

Nobuhito OCHI (Akashi National College of Technology) and Masahide MATSUMURA
Proceedings of Constructional Steel, Vol.19, JSSC, pp. 375- 380 (2011) (in Japanese)

In isolated bridges, some displacement restrainers of superstructures in the transverse direction of the bridge axis, like steel side block (SB), is usually installed for damage protection of expansion joints during earthquakes. However, it can be rational to expect the isolation effects in the transverse direction as well as in the bridge axis against a strong earthquake. Then, developed and proposed by the authors is the steel side block with the knock-off function (CSB), which breaks at a pre-set breaking load and provides smooth shift to the isolated conditions. In this study, small-size shaking table tests and dynamic response analysis of the isolated bridge models installed the CSB are carried out by changing breaking characteristics of the CSB. Then, modeling method of the CSB in the analysis is proposed and the validity of it is verified as compared with the tested dynamic responses.

In-situ Behavior of Super-High Water Content Clay Improved by Plastic Board Drain

Takao YAMAMOTO, Satoru SHIBUYA, Akihiko OHSHIMA, Tsuneharu ORIHASHI, Mitsuhiro NAMBU and Satoshi NONAMI

Journal of Japan Society of Civil Engineers, Vol.66, (2012). (in Japanese)

In an attempt to examine the efficiency of plastic board drain for promoting consolidation of super-high water content clay, various kinds of in-situ measurement were carried out in a pond at Kobe airport. As expected before the ground improvement, it was manifested that the consolidation was achieved by the difference of total water head between the Plastic board drain and the clay. In addition to it, it was confirmed that the self-weight consolidation of the super-high water content clay takes place involved with no dissipation of excess pore water pressure in the clay. On the other hand, the applicability of ball-cone penetration test for estimating water content of the super-high water content clay was confirmed well by showing a good agreement with the direct measurement from the retrieved clay sample. Furthermore, it was well demonstrated that the plastic board drain even when deformed largely functioned well as the drain.

Comparison of Liquefaction Features Observed during the 2010 and 2011 Canterbury Earthquakes

R. P. ORENSE (Univ. of Auckland), T. KIYOTA (Univ. of Tokyo), S. YAMADA, M. CUBRINOVSKI (Univ. of Canterbury), Y. HOSONO (Toyohashi Univ. of Tech), M. OKAMURA (Ehime Univ.), and S. YASUDA (Tokyo Denki Univ.)

Seismological Research Letters, Vol. 82, No. 6, pp.905-918 (2011)

Two successive large-scale earthquakes, with magnitudes 7.1 and 6.3, struck the Canterbury region on the South Island of New Zealand almost 6 months apart. Both earthquakes caused extensive damage to lifelines and residential houses in the city and adjacent areas due to widespread liquefaction and re-liquefaction in areas close to major streams, rivers and wetlands. In this paper, the geotechnical implications of the two earthquakes are discussed based on the results of the reconnaissance investigations performed by the Japanese Geotechnical Society (JGS) immediately after the two events. The widespread liquefaction observed in natural sediments, re-liquefaction of soils within a short period of time, and further damage to earth structures which have been damaged during the first earthquake were discussed. In addition, the severity and extent of damage observed after the two events, especially in the eastern suburbs of Christchurch and in the town of Kaiapoi, are compared. Finally, the soil characteristics and other conditions of the ground near Christchurch's two main rivers, Avon and Heathcote, are presented to delineate the difference in severity of liquefaction observed in the two regions during

the 2011 event.

Repeated Liquefaction Observed During the 2010-2011 Canterbury Earthquakes

T. KIYOTA (Univ. of Tokyo), S. YAMADA, Y. HOSONO (Toyohashi Univ. of Tech)

Bulletin of Earthquake Resistant Structure Research Center, IIS in Univ. of Tokyo, No. 45, pp.115-121 (2012)

Christchurch city in New Zealand suffered from two big aftershocks of the 2010 Darfield earthquake that is main shock of so-called Canterbury earthquakes. They caused repeated liquefaction in suburb of Christchurch city, and severe damage to residences, buried lifelines, river dikes, road facilities and bridges was observed. This report summarizes results from field investigations including Swedish weight sounding tests in the affected area which were conducted after the earthquakes.

An Analysis on Influence of Regional and Individual Conditions to Intended Needs and Actual Demands of Bus Service

Naoki OKAMOTO and Yasuo HINO

Osaka City University, Memoirs of the Faculty of Engineering, Vol. 52, pp. 49-54(2011)

Recently, the vicious circle of decline of bus service and decrease of bus passengers has become remarkable, as the automobile-based life style has popularized with progress of motorization. On the other hand, the mobility of aged people has become important and serious problems because of progress aging society. Therefore, many local governments tried to introduce bus services depended on public subsidy into the inconvenient areas on public transport service¹⁾. However, as the bus passengers must be limited, there are not few cases that were not sustainable due to increase of subsidy. In this study, the influence of regional and individual conditions to intended needs and actual demands of bus service was analyzed through the experimental case study^{2), 3)}. As a result, some interesting findings came out as follows; 1) the number of actual bus passengers may be estimated as a half of the number of persons intended needs for bus, because many residents did not consider the cost subsidized by tax, but 2) some intended needs with obligated purpose and/or without any alternative modes must be actual demands, and also the service level as the distance to bus stop must influence to actual use.

A Prospect of Countermeasures and Important Issues for Road Safety in Future

Yasuo HINO

J Journal of Traffic Science of Osaka, Vol. 42, No.1, pp. 47-52 (2011) (in Japanese)

The conditions of traffic accidents and countermeasures were clearly classified into three stages. The first stage is the pre-1970' when the speed of motorization exceeded the supply of road facilities. The second is the late 1980' with popularizing the automobiles in the life style. The third is the latest decade when the effects of countermeasures have become unremarkable from viewpoint of reduction of traffic accidents. The features of these stages were influenced by changing social condition as well as typical causes of accidents. In this paper, the required issues to ensure the road safety in future were referred, based on the investigation of these social factors and their typical problems.

A study on Steps to Improve Trip Behavior under the Influence of Urban and Transport Policy

Yasuo HINO

Proceedings of symposium on Japanese-Chinese exchange of science and technology 2011, 2.1-2.4(2011) (in Japanese)

Most of people judge the modal choice based on their purpose, cost, time required and comfort level. Therefore,

the adaptation of their behaviors should depend on the service level of transport facilities and their conditions which must be obeyed by the policy. In this paper, some important issues, which should be obtained by analyzing the changes of trip behaviors according to recent trends of policies concerned with city and transport, were referred through some examples from view point of environment and welfare in the aging society. Especially, it was revealed that the trend of modal choice of private facilities such as car and bicycle was depended on transport policy linked the economical policy, and as a result, some serious problems were come in the environment and welfare. Finally, the way of environment oriented polices was investigated based on their results.

Status of Public Transport against Traffic Problems in Major Cities of China

Banban LI and Yasuo HINO

Proceedings of symposium on Japanese-Chinese exchange of science and technology 2011, 2.33-2.36(2011) (in Japanese)

To improve traffic congestion and environmental degradation caused by motorization and urbanization process in China, the preferential policies for public transport development have been introduced. However, public transport share is still declining, and transportation services are poor and lack of transportation infrastructures. In this paper, the process and features of traffic problems in major cities of China are indentified, and the public transport priority policy developed against the bad condition of public transport is also referred. Especially Bus Rapid Transit (BRT) system which has introduced to improve such problems is analyzed. As a result, the existing BRT systems were classified into 3types according the present situation of rail transit system, through the date of Beijing, Guangzhou, Hangzhou and Xiamen.

Study on Major Issues of Road Safety Education based on Safety Consciousness of Bicycles for School Students

Yusuke KOTAKE, Yasuo HINO and Nagahiro YOSHIDA

Japan Society of Civil Engineers, Proceedings of Infrastructure Planning, No.44, 6pp (CD-ROM)(2011) (in Japanese)

Recently, the number of accidents involved school students by riding bicycle. has been increasing. One of the reasons may be the lack of understanding rules of traffic including bicycle and consciousness of road safety. Then, this study focused on not only the consciousness of road safety of school students and parents especially in case of using bicycle, but also the actual condition and major issues of road safety education in school and home. In this study, the important issues concerned with road safety mentioned above were revealed by analyzing the data of large scale questionnaire research including 6,000 and more respondents and selected 29 schools in Hyogo prefecture. As a result, a lack of road safety education in junior high school and high school and understanding and interest of road safety came out of these analyses. Furthermore, base on the additional feedback survey, what is important is continuous instruction and training for teachers about road safety. In addition, it must be important to investigate the cooperation among school students and parents, teacher, police officer and researcher, in order to the effective education system for road safety.

Evaluation of Bus Rapid Transit (BRT) System from viewpoint of Public Transport Integration Strategy in CHINA

Banban LI and Yasuo HINO

Japan Society of Civil Engineers, Proceedings of Infrastructure Planning, No.44, 4pp (CD-ROM)(2011) (in Japanese)

In recent years, in some Chinese big cities, Public Transport Integration Strategies have extensively introduced, in order to improve all kinds of problems caused by automobiles. However, not only their detail but also evaluations of this strategy presented by BRT system were not yet revealed.

Then this study aimed to evaluate BRT systems as a typical integration strategy by analyzing some relevant indicators selected as the essential factors of the internal system, based on the date of public transport improvements in four typical case study cities, as Beijing, Guangzhou, Hangzhou and Xiamen. As a result, the relationship between BRT and general bus systems, road operation, carrying capacity and ratio of modal split comparing with the railway system, level of services and so on were selected as important indicators to evaluate the BRT system. In addition, some benefits of each BRT system were evaluated quantitatively and qualitatively, according to the characteristics of each case study city. These findings should be useful to clarify the placement of the BRT system as the integration strategy and also to introduce this system in other city in near future.

Analysis on the Influence of Winter Weather on Traffic Accidents in the North Desert Region of UYGUR

Kelem ZULPIKAL and Yasuo HINO

Japan Society of Civil Engineers, Proceedings of Infrastructure Planning, No.44, 4pp (CD-ROM)(2011) (in Japanese)

In Uyghur, as the road constructions in the desert region have expanded, the influences of specific desert weather to road safety have been more serious. Therefore, the authors, in particular, tried to show that high temperature and sandstorm in summer weather influenced to physical troubles of tire and engine, as well as driving failure. On the other hand, there must be also some problems caused by winter weather such as cold temperature, strong wind, and heavy snow in the desert region. However the actual influences were not yet revealed because the data is not sufficient. Then this study aimed to analyze the relationship between traffic accidents and winter weather on the G216 national highway located in the north desert region on Uygur. As a result, it should be revealed that the decrease in visibility due to driving and drifting snow and the skid caused by freezing road surface, bring and raise the risk of traffic accidents. In addition, the excess of speed limit due to the monotony driving on the long straight road section. These findings should be useful to improve the road condition and introduce the regulation to control the traffic flow, according to the weather conditions.

Quantify Benefits of Cycling Space Development in Jakarta

Muhammad ZULKIFLI, Yasuo HINO, AM PATTINAJA and Indra TJAHAJANI

Journal of the Eastern Asia Society for Transportation Studies, Vol.9, pp.1024-1039, 2011

This study aims to quantify the benefit of cycling space development in Jakarta. There are very few studies which evaluate benefits of cycling, especially if cyclist's conditions including road facilities are improved. Improvements on health, accidents, air pollution, travel time, saving on parking costs, vehicle cost and security-enjoyments were considered as benefits in this study. As quantifying was done without established data and value available, the Contingent Valuation Methods (CVM) including Willingness to Pay (WTP) and Willingness to Use with considerations and realistic assumptions were introduced as methodology. The results show that development of cycling space is valuable measures, especially on saving of user cost. This is because the higher interest to cycling among the large number of motorized vehicles in Jakarta. This study is designed to discuss the framework of methodology, therefore the finding could be developed to be more comprehensive quantifying for the further research.

Waterfront Functions Required from a Ship Transport Perspective

Yasumasa FUKUSHIMA and Takashi UCHIDA

Osaka City University, Memoirs of the Faculty of Engineering, Vol. 52, pp. 55-62 (2011)

Waterfronts perform various functions such as sites of ‘bustling’ and ‘healing’. From the viewpoint of the involvement of river area residents with rivers, it is important to develop waterfronts utilizing these functions. Devoting attention to needs related to ship transport which used to be an important interface between river and residents along the Yodo River, this study elucidates concrete measures for activation of ship transport and investigates functions that are required at the waterfront of the Yodo River.

New Measure of the Level of Service for Basic Expressway Segments Incorporating Customer Satisfaction

Takashi Sakai, Kiko Yamada-Kawai, Hirokazu Matsumoto and Takashi Uchida

Procedia Social and Behavioral Sciences, Vol. 16, pp. 57-68 (2011)

Using an empirical approach, we produced a level of service (LOS) measure that is consistent with a driver’s subjective evaluation from the viewpoint of customer satisfaction (CS). The study consists of (1) analysis of the causal relation between the level of CS and drivers’ perceptions related to traffic flow conditions using individual response data obtained through in-laboratory experiments with video images, (2) construction of practical driver satisfaction models segmented by the number of lanes of which independent variables are selected among ordinary indices of traffic flow considering results of the analysis presented above, and (3) a proposal of a real-time application of practical satisfaction models.

An Analysis of Town Navigation System Practices and Preliminary Modeling of Sightseeing Spot Choices Seeking for User Oriented Recommendation System

Yuki OKUHATA and Takashi UCHIDA

Japan Society of Civil Engineers, Proceedings of Infrastructure Planning, No.44, 8pp (CD-ROM)(2011) (in Japanese)

As the falling birthrate and the aging population, increasing suburban shopping malls, urban area is on a cavitations phenomenon. In order to solve the problem, a lot of countermeasures like digging up concealed spots by local residents, transmitting information about sightseeing, are worked on positively for local revitalization. In all of the countermeasures, “Pedestrian ITS (Intelligent Transport System)” is in a center of attention to deliver information for sightseeing. Recently, wide variety town navigation systems are adopted in each place. But most of them aren’t done well for themselves because their operations are stopped as soon as management is started. External factor bring down the problems and contents doesn’t attend to user’s needs are causes of that. This study clears up the causes of that modeling of sight-seeing spot choices required for user recommendation system.

Citizen’s Interest Survey for Public Structure Traceability System

Hirokazu MATSUMOTO and Takashi UCHIDA

Japan Society of Civil Engineers, Proceedings of Infrastructure Planning, No.44, 8pp (CD-ROM)(2011) (in Japanese)

It is strongly hoped that government will provide information possessed by them to citizen since in-formation society has grown and civil conscious has changed. System that provides information to citizen easily on a daily basis would bestow many benefits on not only citizen but also government. In this study, we sort current situation of disclosure of official information in Japan and suggest “public structure traceability system” as an indicated system to provide citizen information. Then information items are cleared up with civil conscious obtained through concerns research. In addition, probation experimentation with prototype of the system is performed.

System evaluation and civil conscious are categorized by civil reactions to public structure information.

A Comparative Experiment on Bicycle Path Conditions for Health Benefit using the Estimation Method of Consumption Energy

Soichiro NOTAKE, Nagahiro YOSHIDA, Yasuo HINO, and Takashi UCHIDA

Japan Society of Civil Engineers, Proceedings of Infrastructure Planning, No.44, 6pp (CD-ROM) (2011) (in Japanese)

In recent year, it has been reported that riding a bicycle has positive effects on health in foreign countries. In our country, with the increased interest in health as well as environment, use of bicycle which gains moderate physical activity is attracting many people. Nevertheless, most bicycles are used on pavement; therefore, it seems that low-speed bicycle has no effect on their health. But realizing high-speed bicycle conditions may bring some health benefits.

So in this study, we focused on the difference of energy consumption by bicycle facility conditions, and we estimated energy consumption on actual road using the relationship between heart rate and physical load in laboratorial experiment. As a result, energy consumption per unit time on actual road was increased when subjects ride their bicycles on road than on pavement because of the increase of the speed. It was also found that the amount of the effect depended on bicycle path conditions like gradient, signal interval.

An Experimental Study on the Relationship between Visual Information and Behavior for Bicycle Facility Design

Takanori OKAWA, Nagahiro YOSHIDA, Yasuo HINO, and Takashi UCHIDA

The 5th International Conference on Traffic and Transport Psychology, Poster session, (2012)

Some bicycle lanes with regal control have been introduced on carriageway as a governmental pilot project in Japan. However, the design standard of bicycle facilities is still unclear because of the lack of knowledge for cyclists' safety and convenience on roadway. Therefore this study focuses on interactions between visual information and behavior of cyclists on the various types of bicycle facilities. An experimental study using an eye-mark tracking system and the "probe-bicycle" system, which equipped with sensors measuring handle angle, pedal rotation speed, and break operation, was carried out to examine different type of cycle facility with pavement markings, signs, and additional warning signboards on existing roads. In addition to the measurement by using the probe-bicycle, an interview survey was carried out to confirm cyclist' s cognition. This paper describes results of some comparative analyses for understanding the characteristics of eye tracking and their behavior response to visual information on cycle facilities. The study showed that the range of eye movement was limited on bicycle lane behind the effect of high speed, but the range of eye movement became much wider at the transition from bicycle lane to other cycle facilities due to needs for search of surrounding obstacles.

A Comparative Experiment on Health Benefit of Bicycle Path Conditions using Indirect Energy Consumption Estimation Method

Soichiro NOTAKE, Nagahiro YOSHIDA, Yasuo HINO, and Takashi UCHIDA

The 5th International Conference on Traffic and Transport Psychology, Poster session, (2012)

Several researches showed that riding bicycle has some health benefits in many countries. Riding bicycle in Japan also attracts people who have concerns about their health and environment issues while bicycle trip statistics showed that the average trip distance was much shorter than other countries. Under these situations, some bicycle transport planners focuses on the engineering property of bicycle network to realize health benefit effectively, but

there is few researches describing the health effects on existent bicycle path conditions.

Therefore we conducted the preliminary experiment that 8 students ride on 3 courses representing urban road conditions with approx. 5km length including different types of bicycle path and traffic condition. Before the experiment, expiratory gas analysis was conducted in laboratory which gives an indirect estimation of energy consumption using the relationship between the load strength of physical activity and energy consumption. During the experiment, heart rate was monitored as dependent variable.

This study analyses the relationship between energy consumption rate and bicycle path conditions such as degree of gradient, interval of signals, and accumulation of physical tiredness using indirect energy consumption estimation method. It also investigated the effect of psychological pressures on heart rate caused by road or traffic conditions.

Development of a Reduction Device for Turbidity and Flow of the Bottom Layer by Sediment Dumped into a Vertical Pipe

T. KANAZAWA, K. TSURUGASAKI, T. SHIGEMATSU, T. HIRANO, K. MORITA

Journal of JSCE, Ser. B3 (Ocean Engineering), Vol. 67, pp. I_701-I_705 (2012) (in Japanese)

In backfilling a dredged sea bed pit, reduction and containment of turbidity by dumped sediment are strongly required. In this study, an attachment device to a vertical pipe for reducing generation of turbidity was developed. In the experiments, flow velocity induced by dumped sediment into a vertical pipe and distribution of turbidity were measured in detail. It was shown by laboratory experiments that developed device can reduce velocity and thickness of turbidity cloud moving on the bottom. Moreover, a field experiment using a prototype device in a construction site was carried out. Based on the measured time-series data of velocity and turbidity, effectiveness of the developed device was presented.

Characteristics of Sea Spray Generated by Waves Dashing against a Vertical Wall

M. TAKEDA, K. UOZUMI, T. SHIGEMATSU, M. TSUDA, K. HABUCHI, T. AMINO

Journal of JSCE, Ser. B3 (Ocean Engineering), Vol. 67, pp. I_673-I_678 (2011) (in Japanese)

From view point of operation and maintenance, it is a very important issue to survey durability of salt corrosion of coastal structures. Although accurate prediction of quantity of sea spray which attaches surface of coastal structures, the generation process of sea spray when waves attack the structures such as a pier and a sea wall has not been known yet. In this study, laboratory experiments were carried out by using three high-speed cameras to capture images of generation process of spray when regular waves attack an impermeable vertical wall on 1:30 slop. From every captured image, diameter and location of each spray and the number of generated spray were obtained.

According to experimental results, it was found that the number of generated spray had a peak until $t^*=0.15$ after waves attacked a vertical wall and that the number of spray depended on wave conditions. The time when the number of spray began to increase and the increase rate also depend on wave parameters. The mode value of diameter of generated spray distributed between 0.002 m to 0.003 m, which didn't depend on wave conditions.

An Experimental Study on Effect of Wave-Dissipating Section on Wave Reflection of a Vertical Caisson Covered with Blocks

T. SHIGEMATSU W. TAKESHITA, M. MAEKAWA, K. TSUBOI, H. MATSUSHITA, S. TOKUNAGA

Journal of JSCE, Ser. B2 (Ocean Engineering), Vol. 67, pp. I_130-I_135 (2011) (in Japanese)

A series of laboratory experiment was carried out in order to examine the effect of wave-dissipating section on

wave reflection characteristics of a vertical caisson covered with artificial blocks. Based on the experimental results for regular wave, two simple estimation equations of reflection coefficient were derived. One equation was represented as a function of wave steepness and relative wave height. The other was represented as a function of offshore wave length, the length of the section of wave-dissipating blocks which still water surface crossed, and water depth.

Fundamental Study on Conditions of Sea Spray Generation when Waves Dashing against a Vertical Wall

M. TAKEDA, K. UOZUMI, T. SHIGEMATSU, M. TSUDA, K. HABUCHI, T. AMINO

Journal of JSCE, Ser. B2 (Coastal Engineering), Vol. 67, No. 2, pp. I_701-I_705 (2011) (in Japanese)

From view point of operation and maintenance, it is a very important issue to survey durability of salt corrosion of coastal structures. Although accurate prediction of quantity of sea spray which attaches surface of coastal structures, the generation process of sea spray when waves attack the structures such as a pier and a sea wall has not been known yet. In this study, conditions of sea spray generation which waves dashing against a vertical wall were found out by laboratory experiments and numerical simulation. Although it is known that the Weber number takes part in the generating mechanism of sea spray, the Ursell number might be used as one of the conditions of sea spray generation. It was re-understood well the most predominant factor as the condition of sea spray generation was the collision velocity of water to a vertical wall.

Improvement Effect of Oxygen Supply on Bottom Environment in Consideration of the Oxidation Rate of Reducing Substance

H. TANAKA, T. SHIGEMATSU, T. ENDO

Journal of JSCE, Ser. B2 (Coastal Engineering), Vol. 67, No. 2, pp. I_1096-I_1100 (2011) (in Japanese)

A laboratory experiment using the water of the Doi river was carried out to propose a reaction model of hydrogen sulfide and dissolved oxygen. Effective supply method of oxygen-rich water into the river bottom was investigated for the purpose of remediation of severe hypoxic condition through a series of experiments using a density flow model combined with the proposed reaction model. It was found that hydrogen sulfide of bottom layer mixed by induced flow by density difference and reduced by oxidation reaction. Further, it was found that water supply from multiple points was effective for wide improvement of river water under the same total amount of supply water.

An Experimental Study for Motion Characteristics of a Floating-Type Evacuation Shelter Covered by a Sphere Shell from Tsunami

T. SHIGEMATSU, D. NAKAHIGASHI

Journal of JSCE, Ser. B2 (Coastal Engineering), Vol. 67, No. 2, pp. I_751-I_755 (2011) (in Japanese)

A float-type evacuation shelter has ever been proposed as one of urgent evacuation facilities by one of the authors. In this study, a new shelter covered by a sphere shell was proposed in order to control rotation of evacuation space for refugee. A series of hydraulic experiment was carried out to understand motion of the outer spherical shell and inner shelter. The outer shell had been kept rotating immediately after tsunami attack. In contrast, the inner shelter rotated once, but reverted back to the initial condition. The possibility of control of rotation velocity of the inner shelter by the weight was implied.

Development of Wave Power Generation using a Vertical Slit Type Breakwater

T. SHIGEMATSU, K. KATOH, T. WAKIMOTO, S. YOSHIOKA, I. SOTANI

Journal of JSCE, Ser. B2 (Coastal Engineering), Vol. 67, No. 2, pp. I_1231-I_1235 (2011) (in Japanese)

This study aims development of wave power generation system using wave energy in coastal zone. A wave power generation system using a vertical slit type breakwater widely used in Japanese ports and harbors is proposed by installing an improved Savonius windmill in a chamber of the breakwater. Laboratory experiment was carried out to examine the characteristics of power generation by measurement of the rotational speed and the torque of the windmill. According to the measurement results, the relationship between obtained power and wave condition was discussed. The effect of installing the windmill in a chamber of the breakwater on wave reflection was also discussed.

Parametric Analysis for Characteristics of Turbidity Flow Induced by Sediment Dumped into a Vertical Pipe

T. HIRANO, T. SHIGEMATSU, T. KANAZAWA

Journal of JSCE, Ser. B3 (Ocean Engineering), Vol. 68, No. 2, pp. I_396-I_401 (2012) (in Japanese)

A numerical model which had been already developed by authors for understanding a characteristic of turbidity flow induced by dumped sediment through a vertical pipe is improved by introducing a modified Smagorinsky turbulence model. According to comparison with laboratory experimental results, calculated results reasonably agree with experimental ones. As a result of parametric analysis by the developed model, horizontal velocity and momentum of turbidity mass on the bottom can be controlled by initial sedimentation load. In addition, it is figured out that thickness of turbidity mass on the bottom can be controlled by the clearance between the vertical pipe and water bottom.

A Study on Process of Heat Transfer at Sea Surface Layer Based on Measurement Data

T. HIRANO, T. SHIGEMATSU, T. KANAZAWA

Journal of JSCE, Ser. B3 (Ocean Engineering), Vol. 68, No. 2, pp. I_929-I_934 (2012) (in Japanese)

Water temperature distribution in enclosed water area, especially from water surface to 0.5m under water surface, was measured with weather information, wind, solar radiation. Seasonal change of vertical thermal distribution including violent weather effect is presented. Based on the measurement data, latent heat flux and sensible heat flux are estimated. Moreover thermal diffusivity in the water surface layer with 0.5m depth is evaluated. Finally, thermal flux between water surface and atmosphere is discussed with considering thermal supply from deeper water to water surface.

Environmental Urban Engineering

Distributions of Dissolved Oxygen and Carbon Dioxide in Eastern Osaka Bay and their Effects on the Survival of Adult Southern Rough Shrimp, *Trachysalambria curvirostris*

Yutaka YASUI and Susumu YAMOCHI

Journal of Coastal Zone Studies Vol.24, No. 2, pp. 89-97 (2012) (in Japanese)

We investigated distributions of oxygen and carbon dioxide in the bottom waters of the eastern part of Osaka Bay in high temperature seasons of 2009 and 2010. Indoor experiments were also conducted to examine the effect of hypoxia and high CO₂ concentration on the survival of southern rough shrimp. CO₂ concentrations of the bottom water increased with decreasing dissolved oxygen and concentrations of dissolved oxygen clearly showed an inverse correlation with those of CO₂. Indoor experiments revealed that the 24-hour median lethal concentration of dissolved oxygen was 1.1mg/l (17% in saturation) at 25°C for adult southern rough shrimp. No marked difference was observed on the mortality of southern rough shrimp between a combination of high CO₂ (1300ppm) with low dissolved oxygen and a combination of normal CO₂ (450ppm) with low dissolved oxygen.

Research on the Seasonal Succession of Green Tide and Tolerance of a Causative Seaweed *Ulva ohnoi* to Low Salinity and Desiccation at the North Pond of Osaka Nanko Bird Sanctuary

Midori YOSHIMURA and Susumu YAMOCHI

Journal of JSCE, Ser. B2 (Coastal Engineering), Vol. 67, pp. 1136-1140 (2011) (in Japanese)

Field surveys and laboratory experiments were conducted in 2009 to 2010 to examine methods to reduce outbreaks of green tides by *Ulva* spp. at the north pond of Osaka Nanko bird sanctuary. The green-tide-forming seaweed varied depending on the season, and *U. pertusa* predominated at the bird sanctuary from early summer to autumn, while *U. ohnoi* was abundant there from autumn to early spring. The laboratory experiments revealed that exposure of *U. ohnoi* to air with low salinity inhibited their photosynthesis at 35°C. These results, along with the preceding result of experiments for *U. pertusa* suggest the possibility of controlling a green tide of *U. ohnoi* or *U. pertusa* by a combination of exposure to air for 3-5hours with low salinities of 15-20psu in summer.

Field Surveys on the Characteristic of Changes in Concentrations of Organic Substance and Nutrient Salt at the Tidal Area of the Mouth of the Yamato River

Ryo USUI, Kiwamu TSUBOI, Susumu YAMOCHI

Journal of JSCE, Ser. B2 (Coastal Engineering), Vol. 67, pp. 936-940 (2011) (in Japanese)

Changes in concentrations of organic substances of the sediment and nutrient salts in the pore water of the riverbed were examined at a tidal area of the mouth of the eutrophic Yamato River in 2009-2010. TOC and TN contents of the sediment, together with NH₄-N and NO₂+NO₃-N concentrations in the pore water drastically changed depending on time, month and station. Production rate of NH₄-N in the pore water of the Yamato River was ca.10-100 times higher than that of laboratory experiments. These results suggest the importance of tidal change and wave in evaluating dynamics of organic substances and nutrients at the tidal area of the mouth of a river.

Deconjugation Characteristics of Natural Estrogen Conjugates by Acid-catalyzed Solvolysis and its Application for Wastewater Samples

Yoshinori KANJO, Ze-hua LIU and Satoshi MIZUTANI

Proceedings of the Second Forum on Studies of the Environmental & Public Health Issues in the Asian Mega-cities, pp.203-212, 2010

Deconjugation reactions of natural estrogen conjugates were studied here by three different solutions of 1 M hydrochloric acid (HCl) in methanol. Estrogen sulfates could be easily deconjugated even at low temperature, while deconjugation conditions of estrogen glucuronides required a higher temperature and longer time. For 1 M HCl in methanol with 8% water, the deconjugation efficiencies of the three studied estrogen glucuronides were below 59.4% at 80°C for 360 min, while the corresponding deconjugation efficiencies were above 80.6% for anhydrous HCl methanol at 80 °C for 210 min, which suggested trace water in the solution of 1MHCl methanol retarded the deconjugation rates of estrogen glucuronides. On the other hand, their corresponding deconjugation rates increased with the addition of ethyl acetate, and their corresponding deconjugation efficiencies were above 86.7% at 80 °C for 120 min. As water is a highly polar solution, and the polarity of ethyl acetate is lower than that of methanol, this may suggest that a low polar substance would favor the reaction, while a highly polar solution would prohibit the reaction. All reactions were in pseudo first-order, and higher temperature increased the reaction rate. Finally, a GC-MS method for simultaneous analysis of free estrogens and estrogen conjugates in wastewater with acid-catalyzed solvolysis was developed, and satisfactory recovery efficiencies were obtained by spiking the standard target chemicals into the influent and effluent of one municipal wastewater treatment plant (WWTP), which demonstrated the feasibility of the developed method. Compared with enzymatic hydrolysis, the acid-catalyzed solvolysis method developed here to deconjugate estrogen conjugates is cost effective and time-saving, giving it a greater potential for use with environmental samples.

Remediation of Groundwater Contaminated by Volatile Organochlorinated Compounds with Permeable Reactive Barrier

Yoshinori KANJO and Akihiko OSHIMA and Harue MASUDA

Proceedings of the 3rd International Conference of the OCU Advanced Research Institute for Natural Science and Technology, p.34, 2011

In order to remove or degrade heavy metals or VOC (tetrachloroethylene, trichloroethylene and cis-1,2-dichloroethylene) in the groundwater, we performed the column experiments with the permeable reactive barrier (PRB), which was arranged with the mixture of 2% iron dust, 10% soil, and 88% silica sand. Even if the retention time in the PRB column was only 1 hr, the cumulative removal ratios of PCE, TCE and cis-1,2-DCE per unit iron dust were reached to 22.3, 16.0 and 5.3 mg-VOC/g-Fe, respectively. Using with the PRB column, we can obtain more than 50% of the removal ratios for PCE and TCE for 1 month. Judging from these results, it was concluded that PRB with the mixture of iron dust, soil and silica sand was effective and economical materials for the remediation of polluted groundwater by VOC.

Recovery of toxic metal ions from washing effluent containing excess aminopolycarboxylate chelant in solution

Hiroshi HASEGAWA, Ismail M.M. RAHMANA, Masayoshi NAKANO, Zinnat A. BEGUM, Yuji EGAWA, Teruya MAKI, Yoshiaki FURUSHO, Satoshi MIZUTANI

Wat. Res., 45, pp.4844-4854, 2011

Separation process for the recovery of metals from effluents that contain an excess of Aminopolycarboxylate chelants (APCs) are proposed in this paper. Additionally, the option of recycling the processed water using a solid phase extraction (SPE) system with an ion-selective immobilized macrocyclic material, commonly known as a molecular recognition technology (MRT) gel, is presented. Simulated effluents containing As(V), Cd(II), Cr(III), Pb(II) or Se(IV) in the presence of APCs at molar ratios of 1:50 in H₂O were studied with a flow rate of 0.2 mL min⁻¹. The 'captured' ions in the SPE system were quantitatively eluted with HNO₃. The effects of solution pH, metal-chelant stability constants and matrix elements were assessed. Better separation performance for the metals

was achieved with the MRT-SPE compared to other SPE materials. Our proposed technique offers the advantage of a non-destructive separation of both metal ions and chelants compared to conventional treatment options for such effluents.

Evaluation of Mercury Ion Sorption on Soils by Column Test

Satoshi MIZUTANI, Kazushi KADOTANI and Yoshinori KANJO

J. Japan Society of Civil Engineering, Division G, Vol.67, pp.267-272, 2011 (in Japanese)

Mercury sorption abilities of 4 kinds of soils (Kurotuchi-soil, Akatuchi-soil, Arakidado-soil and Masado-soil) are evaluated by column test, in order to prevent water and soil pollution because of leaching. Mercury solution (1 mg/L of HgCl₂) is poured into the soil layer, and the mercury concentration in the leachate was determined. The difference of them are treated as the quantity of sorption. Kurotuchi-soil showed the highest sorption ability, and Akatuchi-soil and Arakidado-soil is followed. After the experiment of 1200 hours, 1530 mg/kg-soils of mercury were sorbed on Kurotuchi-soil. Furthermore, much higher sorption ability is suggested based on the leaching concentration. The column test shows the similar results with the batch experiment. However, negligible differences are recognized for the mercury sorption ability of each soil between column test and batch test.

Recovery of Indium from End-of-life Liquid-Crystal Display Panels using Aminopolycarboxylate Chelants with the Aid of Mechanochemical Treatment

Hiroshi HASEGAWA, Ismail M.M. RAHMANB, Yuji EGAWA, Hikaru SAWAI, Zinnat A. BEGUM, Teruya MAKI and Satoshi MIZUTANI

Microchemical Journal, in press (Available online 24 August 2012)

Indium is widely used in liquid-crystal displays (LCD) in the form of indium tin oxide (ITO). This work introduces a new technique for the treatment of the end-of-life LCD screens, termed as ITO-glass hereafter, using aminopolycarboxylate chelants (APCs) in combination with a mechanochemical treatment process. APCs are capable of forming stable complexes with the indium deposited on the ITO-glass, whereas the rate of recovery was not substantial. The mechanochemical treatment induces the destruction of crystalline structure with which the ITO fragments are attached and facilitate the increased indium dissolution with the chelants. The increase was more prominent followed by a decrease in the cumulative processing time from 24 to 6 h when the vitrified ITO-glass was simultaneously crushed and washed with the chelants. The extraction of indium was better at the acidic pH condition, and it was further intensified when the operating temperature was raised to ≥ 120 °C.

Distribution of the acid extractable Pb contents in solid waste melting slag,

Satoshi MIZUTANI and Yoshinori KANJO

Proc. 8th Int. conf. Sustainable management of waste and recycled materials in construction (WASCON2012), Gothenburg, Sweden, 30 May - 1 June 2012

The distributions of the acid extractable Pb contents in different solid waste melting slag are discussed. From a municipal solid waste melting plant, 17 lots of slag are sampled during 2 month. Each lot are approximately 3 kg. Each lot are divided into 20 small portions, and 6 g are extracted from each portions. The 1N HCl extraction test (JIS K 0058-2) was performed for each portion. Extracted Pb quantity is determined by ICP-AES and distribution of Pb in one lots are estimated, by statistical process. In the twenty data sets, we sometimes found a specific high values in the samples from the same lot. It is probably caused by the unavoidable mixing of metal Pb. All data were plotted on a lognormal probability paper. Basically the data sets showed logarithmic normal distribution. Based on the average and dispersion of the 20 values, distribution curve of the lot were estimated for each lot. Knowing the distribution of hazardous elements is important to evaluate the safety of the slag.

Introduction of Environmental Safety Control for Recyclable Materials - New Concept in Japan

Satoshi MIZUTANI and Hirofumi SAKANAKURA

Proc. 3rd Forum on Studies of the Environ. & Public Health Issues in Asian Mega-cities (EPAM2012), Beijing, China, 5-6 July 2012

Recyclable materials, such as iron and steel making slag, copper slag, ferronickel slag, municipal solid waste molten slag, coal fly ash etc. are focused on, in order to make the recycling society. Effective use of those materials prolong the time to expiration of landfill site and natural resources. When the recyclable materials are used in our environment, reliance from the viewpoint of environment safety is the most important because these materials potentially contain chemicals that have adverse effect to the natural environment. In this paper, present utilization standard for recyclable materials are introduced. Furthermore the new concepts and guideline of the utilizing recyclable materials in Japan are discussed.

Distribution of Acid Extractable Fluoride in Steelmaking Slag and Mixture Treatment aiming to Reuse

Satoshi MIZUTANI, Yoshinori KANJO and Hirofumi SAKANAKURA

Proc. 3rd int. conf. indust. hazard. waste manage., Sep.12-14, Chania, Greece 2012

Test method for acid extractable contents of chemicals in slag (JIS K0058-2) was performed to four kinds of electric furnace slag generated in Japan. Twenty samples of each slag were experimented. The fluoride content in the same sample was not uniform, and the analytical value showed to log normal distribution. Based on the probability density from log normal distribution, the logarithm average value and standard deviation of content, the distribution curves were drawn. The possibility of excess of an environmental standard for using in the general environment for Slag-A and Slag-D was 100 %. That of Slag-C was 0 % and that of Slag-B was 0.42 %. Furthermore the change of the fluoride contents distribution after mixture treatment of Slag-A and Slag-C are discussed.

Generation Characteristics of Arsine during Metal Recovery by Acid from Lead Smelter Dust,

Satoshi MIZUTANI, Yoshinori KANJO and Hiroshi HASEGAWA

Proc. 3rd int. conf. indust. hazard. waste manage., Sep.12-14, Chania, Greece 2012

Arsine generation characteristics in mixing strong acid with lead smelter dust are studied. Arsine collecting equipment using collection bottles after reacting equipment of dust and acid using conical flask was set up to study the generation characteristics of the gas. The effects of mixing conditions of dust and acid (1. kinds of acid, 2. strength of acid, 3. liquid per solid ratio) on arsine generation were investigated. The highest level of arsine was generated when the dust contacted with HCl. The arsine generated from the other acids addition is much less than HCl. The concentrated HCl (12M) generate much more arsine than dilluted HCl. Basically, the high liquid per solid ratio (L/S) generates high level of arsine.

Extraction of Valuable Metals from Municipal Solid Waste Melting Fly Ash by Acid/Chelating Agent,

Satoshi MIZUTANI, Kota SAKAI, Yoshinori KANJO and Hiroshi HASEGAWA

Proc. SETAC Asia/Pacific 2012, September 24-27, Kumamoto, Japan 2012

In order to recycle valuable metals in fly ash from melting process of municipal solid waste, the recovery experiments by solution were studied. 5 kinds of fly ash were used. The metals were classified into 4 groups: rare metals, valuable metals, invaluable metals and soluble salts. Three different solutes, that is 3N HNO₃, 3N HCl, and 7% EDTA solution, were used for the extraction. Three kinds of single batch extraction tests by 3 kinds of solutes, and 3 kinds of serial batch extraction tests, that is a water-washing treatment followed by a batch extraction by 3 kinds of solutes were performed. Recovery rate of valuable metals and rare metals were 50 - 83% and about 80 % for acid extraction, and were 37 - 90 % and 33 % for EDTA extraction for single batch test. After the water washing processes, the extraction recovery rates of valuable metals increased upto 87 - 97 % for acid extraction and 40 - 95 % for EDTA.

